DIRECT SYNTHESIS OF THIOLATE-PROTECTED GOLD NANOPARTICLES USING BUNTE SALTS AS LIGAND PRECURSORS: INVESTIGATIONS OF LIGAND SHELL FORMATION AND CORE GROWTH

by

SAMUEL E. LOHSE

A DISSERTATION

Presented to the Department of Chemistry
and the Graduate School of the University of Oregon
in partial fulfillment of the requirements
for the degree of
Doctor of Philosophy

June 2011

DISSERTATION APPROVAL PAGE

Student: Samuel E. Lohse

Title: Direct Synthesis of Thiolate-Protected Gold Nanoparticles Using Bunte Salts as Ligand Precursors: Investigations of Ligand Shell Formation and Core Growth

This dissertation has been accepted and approved in partial fulfillment of the requirements for the Doctor of Philosophy degree in the Department of Chemistry by:

Victoria De Rose	Chairperson
James E. Hutchison	Advisor
Catherine Page	Member
Darren W. Johnson	Member
Miriam Deutsch	Outside Member
and	
Richard Linton	Vice President for Research and Graduate Studies/Dean of the Graduate School

Original approval signatures are on file with the University of Oregon Graduate School.

Degree awarded June 2011

DISSERTATION ABSTRACT

Samuel E. Lohse

Doctor of Philosophy

Department of Chemistry

June 2011

Title: Direct Synthesis of Thiolate-Protected Gold Nanoparticles Using Bunte Salts as Ligand Precursors: Investigations of Ligand Shell Formation and Core Growth

Approved: _____
James E. Hutchison

Applications of ligand-protected nanoparticles have increased markedly in recent years, yet their controlled synthesis remains an under-developed field. Nanoparticle syntheses are highly specialized in their execution and often possess significant limitations. For example, the synthesis of thiol-stabilized gold nanoparticles (AuNPs) with core diameters greater than 5.0 nm is difficult to achieve using existing methods. This dissertation describes the development of a synthetic strategy for thiolate-stabilized AuNPs over a wide range of core sizes using alkyl thiosulfates (Bunte salts) as ligand precursors. The use of Bunte salts permits the synthesis of larger AuNPs than can be achieved using thiols by allowing the AuNP cores to grow to larger diameters before the formation of the thiolate ligand shell.

Chapter II details the development of a direct synthesis strategy using Bunte salts as ligand precursors that produces AuNPs with diameters up to 20 nm. Chapter III describes an investigation of the ligand shell formation that occurs during these syntheses. The ligand shell formation involves the adsorption of the Bunte salt to the AuNP surface, where it is converted to the thiolate. This conversion requires an excess of sodium borohydride in the synthesis of >5 nm AuNPs, but not for the synthesis of smaller AuNPs.

This synthetic strategy was adapted for use in flow reactors to attain simultaneous AuNP synthesis and characterization. Chapter IV demonstrates that thiol-stabilized AuNPs can be synthesized in a microfluidic device with product monitoring provided by UV-vis absorbance spectroscopy. The development of a capillary flow reactor that permits the incorporation of new monitoring techniques is presented in Chapter V. The incorporation of Small-Angle X-ray Scattering (SAXS) analysis provides quantitative *in situ* determinations of AuNP diameter. The combination of synthetic control and monitoring makes capillary flow reactors powerful tools for optimization of NP syntheses and monitoring NP growth.

In Chapter VI, the capillary flow reactor is used in an investigation of AuNP core growth. We also review AuNP growth mechanisms and show how to differentiate these using SAXS and UV-vis analysis. In these studies, AuNP growth is unexpectedly shown to involve a coalescence mechanism.

This dissertation includes previously published and co-authored material.

CURRICULUM VITAE

NAME OF AUTHOR: Samuel E. Lohse

GRADUATE AND UNDERGRADUATE SCHOOLS ATTENDED:

University of Oregon, Eugene
Idaho State University, Pocatello

DEGREES AWARDED:

Doctor of Philosophy, Chemistry, 2011, University of Oregon

Master of Science, Chemistry, 2005, Idaho State University

Bachelor of Science, Chemistry, 2005, Idaho State University

Bachelor of Science, Biochemistry, 2003, Idaho State University

AREAS OF SPECIAL INTEREST:

Nanomaterials Chemistry and Synthesis

Green Chemistry

PROFESSIONAL EXPERIENCE:

Research assistant, Chemistry, University of Oregon, Eugene, 2007-2011

Teaching assistant, Chemistry, University of Oregon, Eugene, 2005-2006

Teaching assistant, Chemistry, Idaho State University, Pocatello, 2003-2005

GRANTS, AWARDS, AND HONORS:

NSF IGERT Fellow, University of Oregon, 2008-2010

Graduate Research Symposium Outstanding Oral Presentation, Idaho State University, 2005

PUBLICATIONS:

Lohse, S.E.; Lisowski, C.E.; Hutchison, J.E. Two-Stage Ligand Shell Formation at Gold Nanoparticle Surfaces: Conversion of Bound Thiosulfates to Thiolates. *Inorg Chem*. **Submitted.**

Stankus, D. P.; Lohse, S.E.; Hutchison, J.E.; Nason, J.A. Interactions between natural organic matter and gold nanoparticles stabilized with different organic capping agents. *Environ Sci Tech* **2011**, ASAP.

Lohse, S.E.; Dahl, J.A.; Hutchison, J.E. Direct synthesis of large water-soluble functionalized gold nanoparticles using Bunte salts as ligand precursors. *Langmuir* **2010**, *26*, 7504.

Lohse, S.E.; Rosentreter, J.J. Photooxidation of aqueous trichloroethylene using a buoyant photocatalyst with reaction progress monitored via micro-headspace GC/MS. *Microchemical Journal* **2006**, *82*, 66-72.

ACKNOWLEDGEMENTS

Completion of graduate school and other serious aspects of life are not possible without a lot of hard work from dedicated and talented people behind the scenes.

I would like to thank Jim Hutchison for his assistance in preparing this manuscript and all of his advice and ideas during my time at the University of Oregon. Thanks also to Gautam Bhattacharyya who served as an excellent pre-mentor to all of us graduate students before we found our official homes in the department. I would like to thank all the professors in my committee, the Chemistry Department, and the staff of the Chemistry Department and the Material Science Institute for all their hard work and assistance.

I would like to extend a special thanks to all the fellow members of the Hutchison research group, particularly Dr. Jennifer Dahl and Dr. Michael Jespersen, who played a large role in my early development. More recently, I want to thank all our other group members, who helped make the largely collaborative nature of my work possible: Dr. Carmen Lisowski, Matt Carillo, Dr. Lallie McKenzie, Pat Haben, Ed Elliot, Josh Razink, Rick Glover, Bev Smith, Brandi Dickinson, and Zack Kennedy. I have also been fortunate to work with many talented research partners outside the University of Oregon: Dr. Corey Koch, Dr. Vince Remcho, and Dr. James Ingle. A special thank you to Stephen Golledge, Kurt Langworthy, and the CAMCOR people for helping develop my skills in the characterization of nanomaterials. Thanks also to Alex Hexamer and his team at Beam line 7.3.3 at the Advanced Light Source at Berkeley National Laboratories.

Finally, even more thanks to my family: my mom and dad, brother and sister, and my grandparents. Thanks to all you guys for making this possible.

This research was supported in part by the Air Force research Laboratory (FA 8650-05-5041) and the NSF-IGERT program (DGE-0549503).

To my brother, Keith, and my sister, Gretchen. You guys show me how to do things I thought were impossible every day.

TABLE OF CONTENTS

LIST OF FIGURES

Figure Page

Figure Page

LIST OF TABLES

CHAPTER I

ADVANCES IN GREENER NANOPARTICLE SYNTHESIS: PROGRESS TOWARDS EFFICIENT NANOPARTICLE PRODUCTION

Note: A modified version of the material presented in this chapter will be submitted to the Royal Society of Chemistry journal Green Chemistry. The material presented in this Chapter is formatted according to RSC guidelines. The manuscript was co-authored with Jim Hutchison, who provided editorial guidance and advice.

Introduction: The State of Nanomaterial Production

The continuing realization of new applications for nanomaterials is providing a driving force for the development of large-scale, controlled production of high quality nanomaterials. Due to their remarkable size-dependent properties, which can be harnessed for applications ranging from the construction of exceptionally strong and lightweight composites to the diagnosis and treatment of cancer, [1-5] the demand for nanomaterials of sufficient quality to be used in consumer products is steadily increasing.[6,7] This sustained interest in applying nanomaterials to consumer products has created a demand for *much greater quantities* of high performance materials, both for the development of prototypes and clinical testing.[8,9,10] Though nanomaterial commodity products, such as polydisperse zinc oxide or titanium dioxide nanoparticle dispersions

can routinely be prepared in kilogram quantities,[7] the preparation of more complex nanomaterials (ligand protected quantum dots, anisotropic metal nanoparticles, functionalized gold nanoparticles) is still largely restricted to milligram-scale syntheses.[9,11] The increased demand for high-performance nanoparticles (i.e.- nanoparticles with multiple chemical and physical behaviors engineered into their design) has enhanced the need to swiftly translate nanoparticle syntheses from discovery phase formulations (small amounts of product, reproducibility issues, characterization issues, and uneven performance) to a more application phase/production-scale model (gram-scale, reproducible syntheses with minimal health and environmental hazards and predictable performance).[12-14]

The transition between the laboratory synthesis of nanoparticles and the implementation of production methods is by no means straightforward, as existing syntheses and purification methods for functionalized nanomaterials are rarely developed with large-scale production in mind. Nanomaterial syntheses have historically been developed by empirically-derived successes, because little is known about the chemical principles that govern size, shape, and surface chemistry during synthesis.[3,4] Production of nanomaterials entails the development of scalable, cost-effective, and benign synthetic methods, followed by the successful scale-up of these reactions, and the development and implementation of appropriate monitoring and purification techniques.[11-14] Even when beginning pilot studies for chemical production from syntheses that are well-understood, the translation of initial pilot syntheses to a production line can take years of research and development.[12] The unique features of nanomaterials chemistry, and lack of knowledge

regarding some of the most fundamental aspects of nanomaterial growth make the development of low-hazard, high efficiency syntheses an even more difficult chemical and engineering challenge, as even the path to safe, efficient pilot syntheses is difficult to predict.

The challenges associated with transitioning from lab-scale synthesis to an optimized production process are related to both the synthetic reaction itself, as well as aspects of purification, scale-up, and monitoring. (i) In order to develop suitable production methods, the synthetic efficiency of the reaction must be improved, while the hazard associated with the reaction must be mitigated to the point where it can safely be performed on a large scale. (ii) The methods used to control size and shape in the synthesis must be scalable, so that gram or even kilogram scale amounts of materials can be rapidly prepared with no loss in product quality. (iii) Appropriate monitoring methods must be interfaced with the synthetic reaction so that product quality can be monitored over the course of the reaction, and (iv) suitable purification methods must be developed so that nanomaterials of various sizes and shapes can be isolated while reducing the dependency on high-volume solvent washes. A number of successful strategies have recently been devised that have significantly improved scalability, separation efficiency during purification, and the prospects for quality control through product monitoring in nanomaterial synthesis. Many of these strategies have been borrowed from related disciplines such as chemical engineering and pharmaceutical manufacturing. Improving the synthetic efficiency of the underlying chemical reactions is still one of the most difficult areas to address, however, because significant advances in this area require the

development of new synthetic strategies in a field where understanding of the fundamental chemistry remains incomplete.

Green chemistry offers conceptual guidelines to improve the efficiency of nanomaterials syntheses while simultaneously providing the means to reduce the hazards these syntheses and materials pose to the public and the environment. [3,15,16] Green chemistry therefore provides a potential path to the development of synthetic methods that will form the basis of optimal nanomaterials production (i.e.- synthetic methods that are materially efficient and non-hazardous). Green chemistry and nanochemistry have much to offer one another, but unlike the application of green chemistry to traditional organic chemistry or polymer chemistry, the research community's limited understanding of the active chemical mechanisms in nanoparticle formation and structure-function relationships have hindered the development of new green strategies for nanomaterial synthesis.[4,9] Continuous development of new strategies to develop greener syntheses and greener nanomaterial products is fueled by fundamental investigations into nanomaterial growth and properties, which is, in turn, motivated and enhanced by the development of these new strategies. Contributions made in all these fields enhance the progress that can be made in applying green chemistry to the development of syntheses that are optimally applicable to nanomaterial production (Figure 1.1).

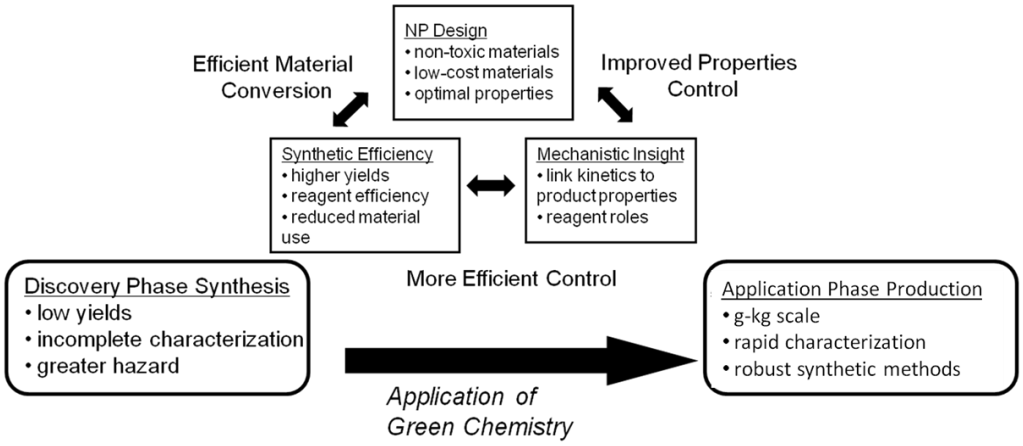

Figure 1.1: Green chemistry provides a path connecting the discovery-phase synthesis of nanomaterials to the development of appropriate synthetic methods to serve as pilot production methods. The principles of green nanochemistry provide a philosophical framework to move from low-efficiency, hazardous syntheses to higher-efficiency, low-hazard production-phase methods. In order to develop strategies to get from one point to the other, our understanding of nanomaterials properties and growth chemistry must evolve. New strategies for green nanomaterials synthesis are developed by the synergistic interaction of research in the fields of nanomaterials properties and design, synthetic efficiency, and mechanistic understanding.

In this perspective review, we discuss progress made in utilizing green chemistry principles to develop strategies that improve the efficiency of ligand-stabilized nanomaterials synthesis, with particular emphasis on noble metal nanoparticle (MNP) and quantum dot (Q-dot) syntheses. These materials represent only a small subsection of the nanomaterial synthesis field, and much more information on the synthesis and properties of different classes of nanomaterials and the green synthesis of nanomaterials can be found in these related reviews.[3-21] In this review, we consider the development of benign, scalable syntheses achieved using green chemistry design principles as an

essential first step in the development of a method for nanomaterial production. We will discuss the application green chemical strategies in the development of more efficient, less hazardous synthetic techniques and examine a few key examples in detail. We will critically examine the advantages of these greener synthetic methods, and the implications they have for the development of application phase production methods. We will also discuss recent efforts to improve mechanistic insight into NP synthesis and product design, which provide the basis for the development of more effective green chemistry strategies. We will address the development of new strategies that permit the gram-scale synthesis of functionalized nanomaterials and the development of new purification strategies that will increase the material efficiency of nanoparticle purification.

History of Nanomaterial Synthesis: Complex Targets Are Realized at the Expense of Efficiency

The earliest syntheses of nanomaterials possessed both elegance and simplicity. They were performed in aqueous solution or solid matrices with benign reagents and relatively low energy inputs; advantages that have been lost in the pursuit of increasingly complex nanomaterials targets.[1-5,22,23] The earliest syntheses (commonly thought to be developed by the Romans) were empirically-derived methods that provided reasonable size and composition control, permitting the use of gold and silver nanoparticles' optical properties in construction of drinking vessels and stained glass windows.[1,2,3,15] Even though the origin of these optical properties would not be recognized for thousands of years, these early syntheses provided the desired materials in reasonable yields with appropriate size control and methods for dispersing the materials into the desired matrix.

In contrast, the majority of modern syntheses for ligand-stabilized nanomaterials are low-yield, multi-step syntheses that permit sophisticated synthetic control over the spatial distribution of atoms, and the dimensions of the core.[3,4] These more complex synthetic methods arose in response to the need to access and study much more complex nanomaterial targets.

The ability to control nanomaterial properties is a direct consequence of the ability to control their structure and composition.[1-5] The three areas of the nanoparticle chemistry that need to be controlled during synthesis are (i) the size, shape and composition of the core, (ii) the overgrowth of additional inorganic shells over the core material, and (iii) the formation of the ligand shell, a layer of adsorbed or covalently bound organic molecules (Figure 2).[1] The ligand shell prevents these particles, which possess high surface energies, from aggregating irreversibly into larger, more energetically stable bulk materials.[1-5] The ligand shell may also display specifically chosen functional groups to the environment (ω-functionalities). This functional group content can be used to direct the assembly of NPs into larger structures, or to bind specific chemical targets.[1-5]In the early years of controlled nanoparticle synthesis (1970-1995), synthetic techniques were developed that focused primarily on controlling the size and shape of the core to better understand the origin and extent of nanomaterial optical and electronic properties.[3,4] More recently (1996-present), synthetic control has focused on the shape of these particles, and the spatial arrangement of molecules on their surface (functionality) or the ability to reproducibly place dopants within the core.[10,24] The need

to control all of these structural features has led to the development of increasingly complex, but also inefficient nanomaterial syntheses.

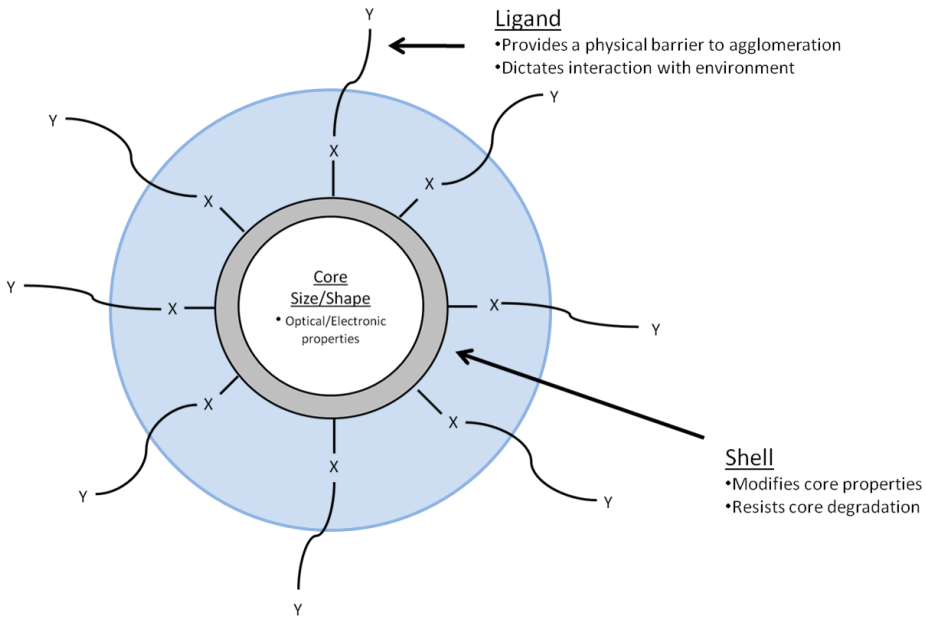

Figure 1.2: The structure of ligand-stabilized nanoparticles. Functionalized NPs consist of three general regions. (i) the core is the origin of the optical/electronic properties, which are modified by the size, shape, and composition. (ii) one or more inorganic shells can be grown over the core to mediate the core's properties and protect it from degradation. (iii) on the exterior, these NPs are usually protected by ligands that are covalently bound or adsorbed to the layer below. The ligand shell has a large impact on the behavior of the particle in its environment, and again improves the stability of the particle.

Modern synthetic techniques for ligand-stabilized nanoparticles are disparate and highly specialized, but share a number of common strategies in order to achieve control over atomic and molecular assembly on the nanoscale.[1-5,24-32] Some of the most ubiquitous synthetic techniques include the synthesis of citrate-stabilized colloidal gold, pioneered by Frens and Turkevich,[2,25] the direct synthesis of thiol-protected gold

nanoparticles (AuNPs) developed by Brust,[1,26] the synthesis of ligand-stabilized quantum dots developed by Murray et al (and subsequently refined by Peng and others),[27] and the synthesis of anisotropic gold nanoparticles developed independently by Murphy, Mulvaney, El-Sayed and others.[28-29] The common stages of solution-based syntheses for nanomaterials are described in Figure 1.3, with the desired efficiency and hazard attributes of a low-hazard, efficient synthesis summarized at each stage. The core material is synthesized from a precursor, which nucleates new particles that grow until they reach a desired size or shape. Control over size and shape is typically achieved by manipulating the growth reaction kinetics. Typical strategies for property control include temporally separating nucleation and growth, or utilizing capping agents with different binding affinities to passivate the growth of particles at different sizes.[1-5] The surface chemistry or composition of the particle may then be modified by subsequent post-synthetic modification steps (growth of additional layers onto the core, or ligand exchange).[1-5] At the end of the growth stages, ligand-stabilized nanoparticles will be present in a crude product mixture that also contains excess starting materials, free-ligand, and by-products. The desired product is separated from the unwanted materials in purification stage that traditionally includes washing, centrifugation, or chromatography.[3,4,9]

Typically, the yields of material afforded by modern synthetic methods are low (milligram quantities), because the synthetic manipulations used to control particle size and shape result in a low percentage of the precursor being converted to the final product. This reality stands in marked contrast to the goals for efficiency and hazard stated in each

stage of Figure 1.3, where the ideal attributes of a green nanoparticle synthetic reaction are described. In traditional synthetic approaches, ligand-stabilized nanomaterials have been prepared using pyrophoric reagents, and toxic heavy metals. Control over nanoparticle shape is often afforded using vast excesses of cytotoxic surfactants, and hazardous organic solvents are still ubiquitous in both synthesis and purification of nanomaterials. In addition, syntheses are often designed so that size and shape are controlled by synthetic processes that permit the formation of unwanted byproducts, or result in the incomplete conversion of the precursor into the desired product.

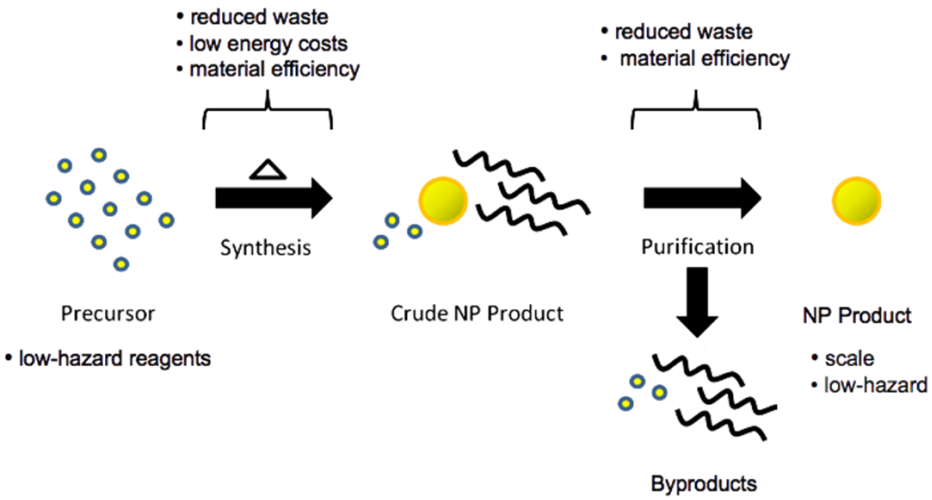

Figure 1.3: An idealized green synthesis for ligand-protected nanoparticles, with the desired characteristics of efficient growth chemistry, purification and the product delineated at each stage. During the synthesis, a non-hazardous molecular precursor is converted into a NP of the desired composition, by the addition of an initiating species (reducing agent, heat, light, etc.). This produces a crude product containing the desired target, as well as a number of small molecular species, ligands, and unwanted byproduct. These are removed using a purification process that produces minimal additional solvent waste, and produces the desired product (which is benign) in high yield. The reality of nanomaterial synthesis is usually quite different.

The in solution growth of gold nanorods (AuNRs) provides an example of how the need to predictably control the physical dimensions of a product is achieved by synthetic techniques that reduce the efficiency of the reaction.[3,4] In this reaction, nucleation (initial particle formation) and growth (the addition of monomer units to existing nuclei) are separated, so that spherical AuNP seeds grow into rod-shaped particles within surfactant templates *via* the reduction of additional gold by ascorbic acid. After purification to remove unreacted gold salt and undesirable small gold spheres, the synthesis yields almost exclusively surfactant-coated AuNRs with controllable aspect ratios in milligram quantities.[3,4] Although this synthesis provides the desired product using a relatively benign synthetic procedure, this level of control comes with a price. The synthetic manipulations used to favor the formation of AuNRs result in the conversion of only about 15% of the gold starting material to the nanorod product.[3,4] In addition, the synthesis requires a large excess of a cytotoxic surfactant (well above the critical micelle concentration), as well as small amounts of silver, in order to synthesize the AuNRs effectively. The complex nature of the nanorod surface chemistry also makes it challenging to effect post-synthetic modifications. These types of sacrifices of efficiency to achieve a more complex chemical target have become commonplace in the synthesis of many ligand-stabilized nanoparticles.

It is clear that new synthetic strategies are necessary to develop nanomaterial synthesis strategies that will form an effective basis for nanomaterial production methods. In the discovery phase of nanomaterials synthesis, the synthesis of more complex, yet more controlled targets is its own reward, and efficiency and hazard receive minimal

consideration.[3,4,9] However, the production of nanomaterials will put a premium of cost-effectiveness (efficiency), while permitting no sacrifice in control over properties.[13,14] Current nanomaterial syntheses, where control over properties correlates with decreased efficiency in the synthesis have set up a situation where the control and efficiency are in competition.[4] This means that new strategies are needed to refine nanomaterial synthesis and recapture the efficiency that marked the earliest syntheses of nanomaterials. This is the first step in developing synthetic methods that will be suitable for nanomaterial production. Green chemistry, specifically geared towards improving synthetic reaction efficiency while decreasing the hazard associated with chemical transformations, is a potential method to do just that.

The Role of Green Chemistry in Converting Discovery-Phase Synthesis to Nanomaterial Production

Green chemistry provides a philosophical approach to develop methods for the production of high performance nanomaterials in an efficient and low-hazard manner.[3,4,15,16] The principles of green chemistry were originally codified by Anastas and Warner, and provide twelve key concepts for designing more efficient, less hazardous chemical reactions.[15] Considering the relative youth of the nanotechnology field, there is a massive opportunity for green chemistry to have a positive impact on the early implementation of nanomaterials production because of the lack of entrenched infrastructure for nanomaterial manufacturing. In addition, the application of green chemistry principles and the design of efficient large-scale production methods share many common goals: among these are the design of more efficient reactions (with respect

to energy consumption, atom economy, number of purification steps, and cost of reagents), the use of minimally hazardous (while maximally efficacious) reagents, and the ability to safely scale up reactions.[3,4,12,13] Despite the appeal of this approach, the progress made in developing green NP synthesis methods has primarily relied on trial and error, fortuitous empirical observations, and effective guess work, making progress in the field gradual.[3,4]

Recently, the original twelve green chemistry principles were condensed to six principles for green nanomaterials synthesis.[3,9] These principles provide a framework that is capable of directing the development of efficient nanomaterials synthesis. These principles are: design for safer materials, design for waste reduction, design for process safety, design for material efficiency, design for end-of-life, and design for energy efficiency.[9] Typically, to effect these design goals, researchers identify the least effective or most hazardous aspects of existing syntheses, and use chemistry strategies that will replicate the effects of existing reagents and protocols in an effort to develop efficient, low-hazard syntheses. Figure 1.4 provides examples of some of the strategies that have been implemented in order to apply green chemistry design principles to existing syntheses. Some examples of the application of these green chemistry strategies to nanomaterials syntheses are reviewed in detail in Section 4.

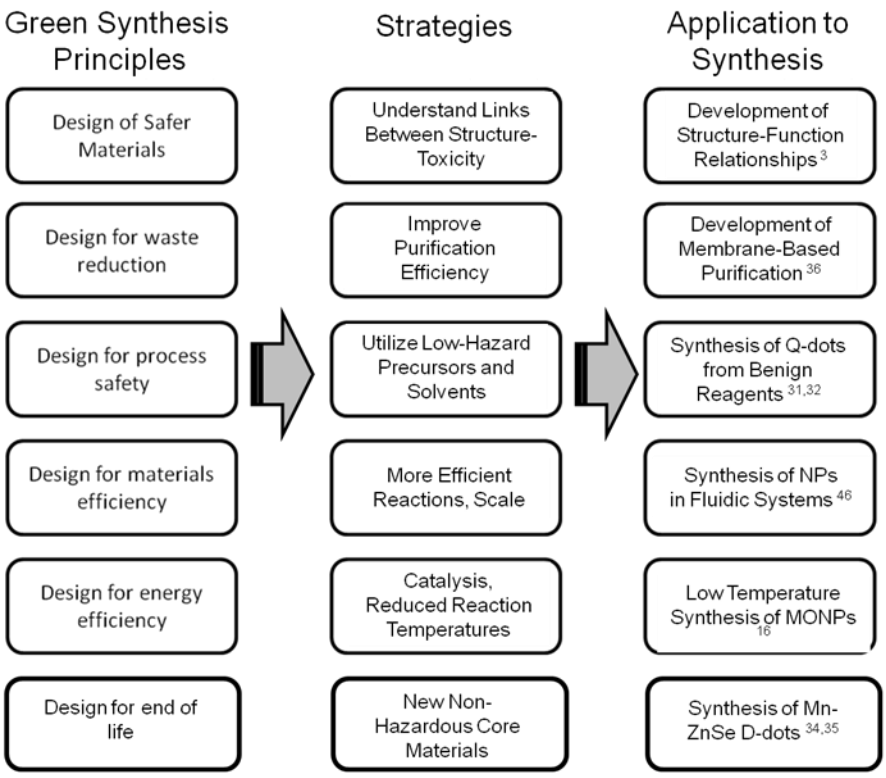

Figure 1.4: The application of green chemistry principles to functionalized nanomaterials (given the community's current understanding of nanoparticle growth) is generally achieved by applying the design principles to specific target areas of the syntheses to formulate a strategy. A number of specific examples of how strategies to address these aspects have been developed are shown in the right hand column.[3,23,34-40] These approaches have provided significant advancements in nanomaterials synthesis, but in order to achieve more holistic green improvements in nanomaterials synthesis, we must develop a better overall understanding of the mechanisms by which nanomaterials grow. Selected examples of the application of these strategies are given in Section 4. (MONP= metal oxide nanoparticle).

The application of these strategies has allowed the research community to make significant strides in the development of greener methods for nanomaterial synthesis. For

instance, there are now a wide variety of solution-based syntheses for ligand-stabilized nanomaterials that can produce milligram quantities of pure material in hours, where once, pyrophoric reagents and syntheses that required days were the norm. However, a lack of insight into the formation mechanisms of nanomaterials synthesis has limited researchers' abilities to design and identify new strategies to improve reaction efficiency.[3,4] This means that the development of new green chemical strategies for the synthesis of ligand-stabilized nanomaterials is somewhat limited by the knowledge base developed from existing mechanistic and structural data.[3] The ability to ultimately relate the precise composition of nanomaterials to their chemical and physical properties and develop growth models may be the most important challenges to meet in the formulation of successful strategies for green nanomaterial synthesis.

Ideally, the application of green chemistry design principles will result in efficient, scalable synthetic methods that will form the basis for nanoparticle production methods. Production methods are generally designed around pilot syntheses that provide the most cost effective, least hazardous routes to the desired product.[3,12,13] Production, however, requires low-hazard, controlled, scalable syntheses that can be performed reproducibly, and monitored for quality control purposes.[12,13] In this way, emerging nanomaterial production somewhat parallels the development of pharmaceutical production methods, where following the development of lead compounds, many years of research have traditionally been required to develop scalable, cost-effective synthetic methods, apply R+D efforts to the development of kilogram-scale production methods, implement them, and build up large enough stockpiles of materials for successful clinical

trials.[12,13] Although a number of strategies for the development of efficient production methods from suitable pilot syntheses exist, green chemistry principles can and should be used in the development and implementation of production methods. In section 5, we will explore some strategies for the scale-up of nanomaterial syntheses, the development of new purification methods, and the implementation of appropriate monitoring techniques in order to explore whether methods in these areas are in place to make nanomaterial production feasible in the event that sufficiently efficient syntheses are developed.

Recent Applications of Green Chemistry Design Principles to Nanomaterial Synthesis

The six principles for green nanomaterials synthesis described in Figure 1.4 suggest a general approach for developing more efficient synthetic reactions, but the successful application of these principles relies on an understanding of the origin of the optical/electronic properties of nanomaterials, the roles of various reagents present in their synthesis, and the chemical/physical properties of the products. Effective application of the design principles is currently most successful when a clear strategy is in place that identifies the primary area of the synthesis where alterations will have maximum benefit without negatively impacting the properties of the product.[3,4] Typically, nanoparticle syntheses are made greener by the judicious application of reagent or solvent substitutions that reduce hazard or improve efficiency.[3,4] A detailed understanding of the roles the reagents play is necessary for these types of alterations to produce maximum benefit. Without a comprehensive understanding of how these alterations affect the efficiency of the reaction and the properties of the product, these substitutions will either

have less than the anticipated impact, or the new product will not possess the desired properties.

This type of diminished utility of the nanoparticle products often occurs when nanomaterial syntheses are attempted in biological systems, or biopolymer matrices as a greener alternative to traditional solvents and capping agents.[41,42] These syntheses may produce products with desired size or shape, but the products are often not isolable, and the surface chemistry is ill-suited for application.[3,18] These materials are not adequate for applications where nanomaterials with well-controlled size and surface chemistry are required, though they do evoke some of the efficiency and simplicity of the earliest nanomaterial syntheses.

In this section, we focus on describing examples of the successful application of some of the green design principles given in Figure 4 to existing nanomaterials syntheses. We will focus on only four of the applied design principles: design of safer materials, design for end of life, design for process safety, and design for material efficiency. Designing for waste reduction and energy efficiency are also very important concepts in the development of nanomaterial production methods, but our intention here is to give only a few key examples of how green synthesis strategies are implemented and executed. In each subsection, we will describe some of the key green synthesis needs that these strategies seek to address, describe a key example of the implementation of this strategy in detail, and then critically assess the effectiveness of the approach.

Design of Safer Processes. Developing synthetic methods that are minimally hazardous is crucial for the large-scale production of nanomaterials, and has been the focus of extensive research over the past decade.[3,4,12,13] The current frontier in safer synthetic design involves removing hazardous reagents while improving the performance of the synthetic method. Some of the key hazards that have traditionally been associated with the synthesis of nanomaterials are the use of pyrophoric reagents in the synthesis of inorganic, ligand-stabilized nanoparticles and the reliance on large quantities of organic solvents.[3,4] Though these are significant concerns in nanomaterial synthesis, their impact is magnified in large-scale production.[12,13,18] The use of pyrophoric reagents makes the scale up of many syntheses almost impossible, while the use of hazardous organic solvents is a significant concern because the amount of solvent produced is disproportionate to the amount of nanomaterial product recovered (liters of solvent to produce milligrams of material).[3,4] The general strategy for removing hazardous reagents and solvents from the syntheses is straightforward enough (identify less toxic reagents that possess the requisite properties), but identifying reagents that provide superior performance can be challenging if the underlying chemistry of the synthesis is not well understood.[35,36] Therefore, identification of appropriate reagent or solvent candidates often requires extensive testing to verify improvements in synthetic performance.

A significant example of the removal of pyrophoric and toxic reagents from an established nanomaterial synthesis was demonstrated in 2001 by Peng, who formulated a new method for the synthesis of functionalized CdSe Q-Dots.[35,36] Peng investigated the utility of several new precursors and ligands to replace dimethyl cadmium (acutely toxic,

pyrophoric) and tri-octyl phosphine oxide (TOPO), which were used in the original quantum dot synthesis developed by Murray and Bawendi.[35] Peng demonstrated that cadmium oxide and cadmium acetate (less toxic, non-pyrophoric cadmium sources) improved the efficiency and versatility of the synthesis, as did the replacement of the expensive TOPO with common fatty acids.[35,36]

Peng's re-formulated procedure resulted in an increase in the performance and versatility of the original quantum dot synthesis. Q-dots with core diameters between 1.5 and 25.0 nm can be prepared using Peng's method (a significant increase in the range of core diameters available versus the previous synthesis), a synthetic accomplishment that significantly increased the range of emission wavelengths that could be accessed using Q-dots. In addition, the use of fatty acids as a capping agent/solvent increases the efficiency of post-synthetic modifications to the Q-dots.[4,35,36] In this case, the simple replacement of a very toxic and hazardous reagent and an expensive solvent had far-reaching consequences in improving the safety and efficiency of the traditional synthetic method.

Similar reductions in hazard, while increasing the efficiency of nanomaterials synthesis were realized by our group in 2000, where we showed that the phosphine-protected 1.5 nm gold clusters could be synthesized using a simple in-solution method, using sodium borohydride (rather than diborane) as a reducing agent.[3,4,42] The previous solvent, benzene, was also replaced with a less hazardous compound, toluene. By removing the pyrophoric reagent from the synthesis, the need for specialty glassware and inert atmosphere conditions were also removed, and the synthesis of the phosphine-protected AuNPs can now be performed under open atmosphere conditions. In addition to

removing a pyrophoric reagent, the alterations to the method actually increased the yield of the synthesis, reducing the time and material cost required to prepare phosphine-protected AuNPs (~1 g/day vs ~100 mg/day).[3,4,43]

Examples such as these represent advances in the preparation of ligand-stabilized nanoparticles from low-yielding, energy-intensive syntheses to synthetic procedures that can be performed in almost any laboratory with minimum hazard to users. In these cases, simple reagent or solvent substitutions were the major changes needed to implement the design principle. These alterations, however, were achieved primarily by extensive testing and empirical observation. An understanding of the chemistry involved certainly played a role, but insufficient knowledge was available to simply make *a priori* alterations to the existing synthetic methods. In the future, it will be important to develop more rational strategies to target likely replacement compounds and solvents, but this can only be done by developing better understanding of the roles the reagents play in the synthesis of nanomaterials. Therefore, more extensive investigations of nanoparticle growth mechanisms will be a significant boon to the speed with which less-hazardous synthetic procedures are developed.

Design for End of Life/Design for Safer Products. The mere fact that nanomaterials possess novel properties based on their unique size makes their inherent hazard hard to predict and model. This is not acceptable from the standpoint of consumer products, particularly for nanomaterials that are being touted for use in therapeutic applications. Unless the hazard associated with nanomaterials can be assessed and mitigated where appropriate, the development of high-performance production methods is a moot point.

The challenge in designing safe nanoproducts is essentially being addressed in two ways. First, the fate and degradation of nanomaterials in biological systems and the environment needs to be understood.[3,8,9,32,3344] One thing that is certain is that nanomaterials possess at least the potential toxicity of the chemical constituents, should the nanoparticle degrade.[3,9,44] Secondly, the relationships between nanoparticle size and composition and their likely toxicity must be quantified. This is a more challenging problem, and is currently the subject of intense research.[32,33,44] Thus, while it is possible to design for the end of life of these materials, designing for inherently safer nanomaterials is still struggling to circumvent a substantial knowledge gap.

Both of these design principles are a significant concern for nanomaterials, such as Q-dots, that contain toxic metals (such as Cd or Se) within their cores.[3,4] As a general rule, high-performance nanomaterials should be synthesized entirely from non-toxic (or minimally-toxic) reagents, because this decreases the likelihood that when the finished NP is released into the environment or biological systems (either at end-of-life or in applications) that it will have negative human or environmental health impacts.[3,8,9,44] However, successful implementation of these design criteria requires an extensive understanding of the origin of nanoparticles' size dependent properties- and it is not always clear how less toxic materials can be used to replicate nanoscale properties that are intrinsic to other, more hazardous materials. We are only beginning to understand the physics and chemistry of nanoscale materials to the point where we can predict many of the optical and electronic properties that occur in novel nanomaterials, but there are several notable instances, where nanochemists have used less hazardous materials to

replicate the performance properties typically achieved through the use of toxic materials. In recent years, Peng has demonstrated that Mn-doped ZnSe and Cu-doped InP nanocrystals could show tunable emission (as a result of recombination events with the dopants) that extends across most of the visible spectrum and into the near IR, replicating the size-dependent band gap emission of CdSe quantum dots.[38-40]

In 2007, Peng et al. developed a synthesis for cadmium-free, transition metal-doped Q-dots (also known as D-dots) by separating the nucleation, doping, and growth steps in the synthesis of Mn-doped ZnSe.[38,39] In this procedure, MnSe nanoclusters are nucleated, and then over-coated with ZnSe in order to produce MnSe:ZnSe core-shell NPs or Mn-doped ZnSe NPs.[38,39] The spatial distribution of the dopants can be controlled by varying the temperature of the over-coating process, and the concentration of the precursors.[39] In 2010, Peng's group demonstrated that this approach could also be extended to Cu-InP D-dots.[40] The D-dots possess readily tunable optical properties, and good quantum yields (up to 40%), but the relative quantum yields can vary substantially depending on the nature and concentration of the dopants.[38,39] They can also be readily functionalized by analogous methods to CdSe Q-dots.[39] With the advent of the Cu-InP dots, their tunable emission has been extended across the length of the visible spectrum and into the near-IR.[40] The development of the D-dots represents an important demonstration that high-performance nanomaterial properties can be replicated using only low-hazard precursors, when appropriate chemical strategies are employed.

The principal drawback associated with this approach to developing non-toxic quantum dots is that the concentration and distribution of the dopants must be carefully

controlled in order to maintain the desired optical properties.[40] This type of approach can increase the synthetic complexity of the product, introducing new challenges for efficient synthesis. In this case, the ability to correctly control the composition of the D-dot and the location of the dopants has a significant influence on the emission properties of the product, which approach, but do not necessarily exceed the optical performance of traditional Q-dots. Finally, it should also be noted, that while Peng's strategy addresses the hazards associated with nanoparticle degradation, the hazard associated with D-dots *as nanomaterial products* is still entirely unknown, and new structure-function relationship studies will have to be undertaken in order to quantify their hazard versus traditional Q-dots.

The development of alternative non-toxic core materials for high-performance nanomaterials is an area of green nanomaterial synthesis that is beginning to receive significant attention. Peng's research again shows that the implementation of an effective chemical strategy can circumvent a major green chemistry challenge, and produce a high-performance nanomaterial product. The ability to extend this type of approach to develop multiple alternative core materials to CdSe is impressive, but the complicated structural manipulations necessary to replicate the properties of the hazardous substance highlight the need to continue to develop insights into how nanomaterial structure and composition influence nanoparticle properties. In addition, the need to increase the structural complexity of the core material in order to reduce hazard will have implications in the overall efficiency of the synthetic method, which in turn makes the development of an efficient production method more complex.

The Design of Efficient Synthetic Reactions. While reducing the hazard associated with nanomaterials synthesis is an important part of green nanomaterials production, improving the material efficiency of the reaction is vital for the transition from nanomaterials synthesis to nanoparticle production. The overall efficiency of a synthetic reaction can be assessed in many different ways, including measuring the amount of waste generated versus the amount of product recovered (E-factor),[18] the amount of auxiliary reagents that are required, the time required to synthesize a given amount of the material (throughput), and the energy cost associated with the synthesis.[3,4] In addition, the actual yield of the nanoparticle synthesis and the amount of byproducts produced versus the amount of product recovered are important from a cost-effectiveness standpoint.[9,12,13] Strategies based on all of these approaches have been proposed to improve the overall efficiency of nanomaterial synthesis, with the amount of waste generated being a principal concern. From an environmental standpoint, the generation of unnecessary waste (particularly excessive use of organic solvents or the presence of hazardous ancillary reagents in the waste stream) is exactly the type of environmental hazard that green chemistry was implemented to avoid.

In recent years, the problem of efficiency in synthesis has been attacked from a variety of angles. Many of the most successful strategies have targeted improvements in the efficiency of purification, attempting to reduce a reliance on organic solvents as eluents (purification strategies will be discussed in detail in Section 5).[34] Other researchers have focused on eliminating hazardous auxillary reagents that promote size or shape control. For instance, it was recently shown that the effective synthesis of gold

nanorods could be realized with only a small fraction of the amount of cetyl-trimethyl ammonium bromide (CTAB, a cytotoxic surfactant) that is typically used as a shape-directing agent.[45] The feasibility of eliminating post-synthetic modification steps (e.g.- ligand exchange) to produce a broader size range of functionalized nanomaterials has also been explored. A number of researchers have recently shown that protected thiols (e.g.- Bunte salts and thioacetates) can be used to access an expanded the size range of thiol-protected AuNPs through direct synthesis.[46-50] Synthesizing these nanoparticles directly reduces the total number of synthetic steps required to produce thiol-protected AuNPs with core diameters greater than 5.0 nm,[47,48] and in certain cases eliminated the need to use biphasic reaction mixtures and phase-transfer catalysts to synthesize these nanoparticles.[49]

While a plethora of strategies have been demonstrated that increase *aspects* of nanoparticle synthetic efficiency, too many of these approaches focus on *only* a single aspect of efficiency. For instance, the implementation of more efficient purification methods may eliminate the need for hazardous reagents in purification, but does not address the atom economy of the synthetic reaction, or address the traditionally very poor yields of nanomaterial synthetic reactions (recall that only 15% of the gold that goes in the synthesis of gold nanorods is recovered as product).[4] From the examples above, it can be seen that strategies for improving the efficiency of nanomaterial synthesis primarily focus on the elimination of hazardous waste, but, from a production standpoint, the atom economy of the synthetic reaction and the overall yield are very important considerations that need to be more thoroughly researched.[8,18] In the case of improving synthetic

efficiency, a grounded mechanistic understanding of nanoparticle growth chemistry and ligand shell formation are vital for improving reaction yields and atom economy.

Developments in Mechanistic Investigations of Nanoparticle Synthesis. Identifying the optimal green chemistry strategies for nanoparticle synthesis will be a slow, painstaking process unless we can develop a detailed chemical understanding of the formation chemistry of nanomaterials.[3,4] This level of understanding is not easy to come by, however. As we have previously described, nanomaterials syntheses are very complex chemical reactions, often requiring that thousands to millions of atoms and molecules come together in a controlled fashion to make a specific target. Add to this the fact that many of these reactions occur completely in a matter of minutes, and the difficulty associated with fully detailing the chemical reactions that make up the synthesis of ligand-stabilized nanoparticles becomes a daunting task.[3,51] In addition to understanding the process by which the core material develops its size and shape, it also necessary to understand how ligand shell formation occurs during synthesis and during post-synthetic modification processes (i.e.-ligand exchange).[51] It is these mechanistic insights, however, that form the basis of effective strategies for the application of green chemistry principles. Without understanding how nanomaterials form, effective alternative reagents and reaction conditions that improve reaction efficiency and reduce hazard cannot be effectively identified.

Recently, this commitment to mechanistic investigation, and the implementation of improved strategies for reaction monitoring have led to a number of important mechanistic findings that were subsequently utilized to improve the versatility of many

syntheses and improve control over product properties.[51-72] For the past decade, researchers have been using the classical models of nanoparticles growth (e.g.- temporal separation of nucleation and growth) to attempt to produce more monodisperse products or improve size or shape control in synthesis.[3,4,66] Though these studies greatly expanded the arsenal of nanomaterial synthetic techniques, size and shape control methods are still not as precise as many researchers would desire.[52,53] In the past few years, however, the implementation of new monitoring techniques and an increased number of mechanistic studies have shed new light on key features of many traditional nanoparticle syntheses, including the growth of CdSe quantum dots,[68-70] the synthesis of gold nanoparticles,[53-58,61-64,71,72] and the growth of anisotropic nanocrystals.[59,60,65] Among the most important findings from these studies has been the observation that the speciation of monomers in the reaction mixture has a strong influence on the size and shape of the product.[66,70,72] In addition, the observation of metal nanoparticle growth by coalescence, rather than monomer diffusion to nuclei has been observed in certain size regimes.[54-56] The chemical processes that underlie ligand shell formation and the process of ligand exchange have been investigated in much greater detail, as well, revealing that ligand shells re-organize as nanoparticles age, and that ligand shell formation from related species (e.g. thiols versus disulfides) proceed by substantially different mechanisms.[51]

Several of these mechanistic observations have been used effectively to more precisely control the synthesis of nanomaterials. It was recently shown that the pH has a substantial impact on the mechanism of AuNP formation in the Turkevich synthesis, and that by controlling the pH of the reaction, the size and dispersity of the AuNPs could be

more precisely controlled than by varying the citrate:gold ratio used in the synthesis.[57,58] Similarly, Jana developed a gram-scale synthesis for gold nanorods by demonstrating how the size of the gold nanoparticle seed used to initiate the nanorod synthesis influenced the mechanism of anisotropic nanoparticle growth.[29] Jana's work also showed why small variations in reaction conditions in nanorods synthesis tend to lead to the development of very different anisotropic shapes (e.g.- cubes and stars). Even Peng's synthesis of D-dots is based on a strategy of temporally separating nucleation and growth to achieve the necessary control over nanoparticle structure.[38-40] These types of studies provide important examples of how mechanistic insights can be utilized to achieve the synthesis of nanoparticles with increasingly well-controlled properties.

At this stage, the number of studies focusing on the fine details of the mechanisms of nanomaterial formation is only beginning to yield significant dividends in improving synthetic control of nanoparticle properties, but the appropriate implementation of instrumental techniques and mechanistic investigations will continue to shed light on the growth kinetics and key mechanistic details in nanoparticle formation. By fully understanding the roles of the different reagents in the synthesis, researchers can develop optimal strategies in the green synthesis of nanomaterials. The successful implementation of new monitoring techniques, such as SAXS and liquid-cell TEM, have significantly enhanced our understanding of nanoparticle growth mechanisms.[52-54] Based on the conflux of appropriate analytical techniques and strategies for probing different aspects of nanoparticle growth mechanisms, we may be poised for a significant boom in mechanistic insights into various nanoparticle syntheses.

Progress in the Development of Green Nanoparticle Syntheses. The application of the green chemistry design principles described in Figure 1.4 has resulted in a number examples of greener nanomaterial syntheses that have resulted in the development of less-hazardous, more efficient synthetic methods, and even the development of high-performance nanomaterials from non-toxic core materials. However, the reaction efficiency (i.e.- atom economy and yield) of nanomaterials syntheses is still relatively low. The low reaction efficiency of many nanomaterial syntheses and the excess volumes of hazardous organic solvents generated during synthesis are important barriers to overcome in the formulation of nanomaterial syntheses that can serve as suitable pilot methods for production. In order to circumvent these challenges, deeper mechanistic insights into nanomaterial synthesis must be achieved.

Moving from Pilot Synthesis to Production

We have discussed how green chemical design principles can be used to develop nanoparticle synthesis strategies that may ultimately lead to nanoparticle synthesis methods that are benign, efficient, and scalable. These types of syntheses would be ideal candidates to begin designing production methods around. Production implies much more than effective synthesis, however. At the production phase, the yield of material, the robustness of the synthetic method, and the ease with which the requisite purification and monitoring can be incorporated into the production line are crucial factors in developing cost-effective methods for high quality nanomaterial production.[11-13] Thus, scale is a defining feature between nanomaterial synthesis and production, but appropriate monitoring of the synthesis, and the ability to develop suitable purification methods that

scale with synthesis are also key requirements in the production of ligand-stabilized nanomaterials.

Reaction scale, effective monitoring, and purification play significant, but very different roles in the synthesis of new nanomaterials, and the application of production methods.[11] In the development and refinement of synthetic methods, scale is primarily a concern in generating sufficient material for characterization and the development of structure-function relationships.[9] Similarly, the purity of materials is crucial for appropriate characterization.[11] Monitoring is primarily deployed to correlate structure and properties or to investigate mechanisms of formation.[3] In the development of production methods, scale becomes an absolute concern, with the appropriate scale defined by the demand for sufficient material for testing or prototype development.[11-13] Purification is essential in order to remove any byproducts that may negatively impact product properties.[9] Monitoring is deployed primarily for QC purposes, and is used to ensure that the material produced has the requisite properties or purity (Figure 1.5).[11] Similarly, the performance requirements for scale, monitoring and purification are very different at the level of a laboratory scale synthesis and gram-scale production. Some of the differences in performance requirements for these areas are given in Figure 1.5.

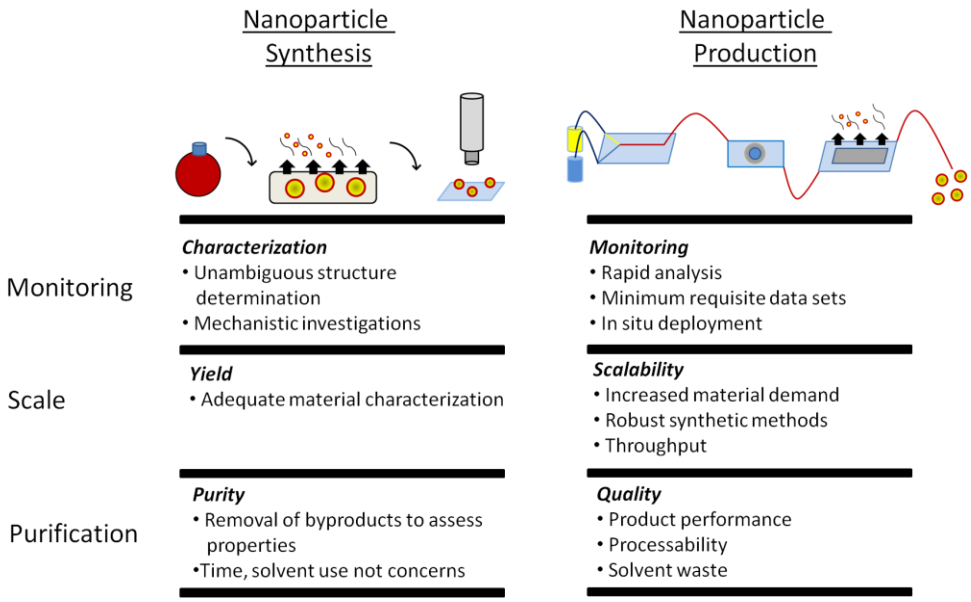

Figure 1.5: The different roles and requirements for reaction scale, purification, and monitoring are given for two different phases in nanomaterial production (synthesis and production). In the synthesis phase, scale and purity are primarily concerns in the production of material for analysis/characterization, but in the production phase, scale is an absolute requirement to meet demand, while monitoring and purification are primarily concerned with product quality, and throughput and cost-effectiveness dictate the feasibility of these strategies.

Monitoring Nanomaterial Synthesis for Mechanistic Insight and Quality Control in Production. Reaction monitoring and characterization serve very different roles during the various stages of nanoparticle production development. The deployment of adequate monitoring methods in mechanistic investigations is crucial for determining reaction kinetics and identifying key intermediates. These types of mechanistic realizations inform the development of more effective synthetic strategies, as was discussed in Section 4. In addition, the adequate characterization of materials following synthesis is an important pre-requisite for the successful investigation of their fate and toxicity. During the

development of production methods and during active production, however, monitoring is primarily important for quality control purposes and verifying the robustness of a given synthetic method. In many cases, characterization and monitoring make use of similar instrumental techniques, but during production, rapid analysis becomes increasingly important, and minimum sufficient characterization data sets to ensure product quality are the most important pieces of information to gather. Therefore, the ability to deploy analytical techniques *in situ*, and the ability to acquire sufficient characterization data in real time are the most important requirements for effective monitoring during production.

Previously, *in situ* monitoring of nanoparticle formation was restricted to qualitative analysis techniques such as UV-vis absorbance spectroscopy or emission spectroscopy methods, however, several new *in situ* techniques that provide quantitative data on nanoparticle size and shape have recently been demonstrated.[52-5473,74,75,76] Optical spectroscopy techniques can provide rich data about nanoparticle size and shape in a non-invasive manner (particularly if absorbance features can be closely correlated with size determinations by TEM). However, these methods are typically limited to the analysis of particular size regimes of nanoparticles, and do not provide facile quantitative determinations of size and shape dispersity.

Two new techniques have recently been demonstrated that permit quantitative *in situ* monitoring of NP core diameter with improved detail.[52-54] The first technique adapts TEM analysis for *in situ* monitoring of single nanoparticles in a growth solution by incorporating a liquid stage containing NP growth media.[53-54] This permits the real-time monitoring of individual nanoparticles growing over time, and has yielded significant

insights regarding possible size-dependent behaviors in the method of NP growth. This method is limited in its scope by many of the traditional microscopy limitations: the time required to analyze a statistically relevant fraction of the NP population and the possibility that growth mechanisms are affected by extended electron exposure within the microscope. These limitations make *in situ* TEM more useful for mechanistic studies than production monitoring. The second approach, in contrast, uses scattering techniques (DLS or SAXS) to determine particle size and shape distributions for whole nanoparticle samples rapidly and effectively.[52] These techniques have been employed for everything from simple size analysis to real-time monitoring of NP growth kinetics. These scattering analyses are typically rapid, and provide quantitative determinations of both mean core diameter and dispersity.[52] These scattering analyses are therefore well-suited for both mechanistic investigations and quality control in production, though depending on the desired temporal resolution, significant infrastructure (e.g.- synchrotron radiation sources) may be required.

The application of new monitoring techniques provides straightforward methods to verify material dimensions and properties during synthesis. Integrating these analytical techniques with possible production platforms is the principle challenge in utilizing existing nanoparticle characterization techniques for effective monitoring. The recent addition of real-time microscopy monitoring of NP growth and the successful deployment of scattering analyses for quantitatively monitoring the growth of NP populations are poised to deliver breakthroughs in our mechanistic understanding of NP formation, and scattering analyses provide a simple solution for real-time quantitative

product monitoring. However, these new monitoring techniques only assess the size and shape of nanomaterial samples. Though this is an important element of quality control, developing rapid characterization methods for analyzing nanoparticle surface chemistry and composition is another important monitoring challenge in the synthesis of ligand-stabilized nanomaterials, but one that has not been extensively investigated.

Scaling up Nanomaterials Synthesis to Meet Production Goals. An important difference between the synthesis of specialty nanomaterials in a research lab, and the production of functionalized gold nanoparticles for commercial applications is the ability to prepare the material on the necessary scale (g-kg) and preserve or improve the synthetic control over size, shape, and surface chemistry afforded by the original synthesis.[3,4,37] In addition, the presence of hazardous reagents and waste generation must also be carefully considered when choosing strategies for nanomaterial scale up. In the discovery phase, it is important to be able to synthesize sufficient amounts of material only to adequately characterize the material that has been created.[11] In the development of pilot synthetic methods for production, the potential scalability of the method is an important concern. Therefore, successful scale up strategies for nanoparticle synthesis must consider the ability to control properties, the exposure of workers to hazardous reagents, and the absolute amount of material that can be produced.

From a green chemistry perspective, it is imperative that strategies for scale up permit the synthetic method to continue to provide efficient synthetic control over material properties, and that the method for scale up reduces or eliminates the use of hazardous solvents or reagents. The best strategy for addressing these concerns requires

the development of pilot synthetic methods that are benign and efficient. Then, as long as no new solvent or reagent use is incurred in the scale up of the reaction, the synthesis of the nanomaterial remains viable. In this case, the challenge reduces to developing strategies to scale nanomaterial production without introducing additional hazard or sacrificing synthetic efficiency.

Conceptually, it would seem quite simple to scale up existing nanomaterials syntheses until the desired amount of material is achieved, but changes in the scale of nanomaterial synthetic reaction has consequences for researchers' ability to control their properties. Increasing the scale at which a synthesis is run can impact localized reagent concentrations in the reaction vessel, affect the rate of heat dissipation, or make it increasingly challenging to maintain an inert atmosphere environment within the reaction vessel, all leading to changes in the product properties.[37,77-82] One response to these concerns has been to miniaturize nanoparticle syntheses by performing these reactions in flow reactors (particularly microfluidic devices).[37] Ironically, going to small reactors can provide an opportunity to increase the scale of nanomaterial synthesis. Fluidic devices provide a continuous stream of product (high-throughput syntheses) and can be operated continuously (in theory). [37] If larger quantities of material are required, multiple reactors can be operated in parallel to produce larger amounts of product (a process referred to as numbering up).[37]

Fluidic synthesis reactors have been shown to provide improved control over product properties, providing a variety of options to closely control the timing and volumes of reagent additions, and the option to incorporate a variety of analytical

techniques for real-time monitoring (Figure 1.6), making flow reactors somewhat analogous to miniature production lines.[37] Several classes of ligand-stabilized nanomaterials, including metal NPs, gold nanorods, and Q-dots have been synthesized in simple microfluidic devices, with varying degrees of success.[77-82] The microfluidic devices employed in these studies range from the simple to the highly complex, and have been fabricated from many materials, including glass, PDMS, and harder polymers. [37] Many of these devices have also been designed to include various analytical techniques for real-time monitoring of NP size, with UV-vis absorbance spectroscopy being the most common. [37] The combination of improved synthetic control, built-in monitoring, and the potential to rapidly synthesize large amounts of material have applications in the large-scale synthesis of nanomaterials, the investigation of nanoparticle growth kinetics, as well as the rapid optimization of nanoparticle synthesis by combinatorial approaches.

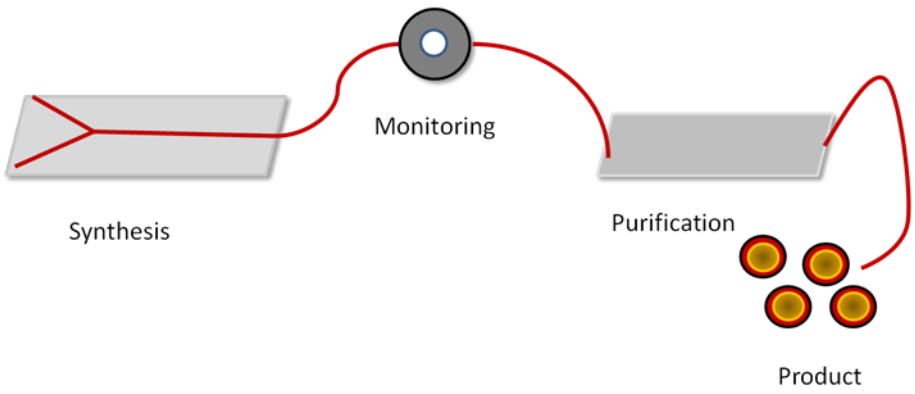

Figure 1.6: A diagram of an idealized microfluidic device that integrates synthesis, monitoring, and purification. In this way, the idealized microfluidic device is analogous to a nanoparticle production line, but with all the components integrated into a single, modular device that is highly portable and potentially be run by automated systems.

A key example of a fluid reactor-based system for large-scale nanomaterial synthesis is the development of the Workstation for Automated Nanomaterials Discovery and Analysis (WANDA) system at Lawrence Berkeley National Labs.[78] WANDA is an automated nanomaterial synthesis system containing eight custom reactors that provide precise temperature control and an inert atmosphere environment for the rapid synthesis of ligand-stabilized quantum dots. High-throughput optical spectroscopy methods have been successfully interfaced with the WANDA system to permit rapid characterization of the products, and the system automatically spots quartz plates for ex situ characterization by XRD.[78] WANDA has also been employed for the combinatorial optimization of nanomaterial synthesis methods, and kinetic analysis of quantum dot growth. This type of self-contained reactor and analysis system demonstrates the potential that flow reactors possess for high-throughput synthesis and screening of nanomaterials.

In concept, flow reactors provide an ideal synthetic environment for the synthesis of many ligand-stabilized nanomaterials. In practice, however, there are many challenges, both chemical and engineering-based, that must be overcome in order to correctly utilize fluidic systems for nanomaterials synthesis.[37] The choice of solvent is crucial, as many reactors are made of soft polymers that are not compatible with many common organic solvents, and bi-phasic solvent systems require the use of sophisticated mixers in order to adequately mix the two reagent streams.[37] In addition, the narrow reaction channels of the fluidic devices make them susceptible to fouling due to nanomaterials aggregation.[37,77-83] Song et al. recently highlighted a number of key challenges that must be addressed before fluidic syntheses gain more wide-scale use.[37] These include the complete characterization

of materials produced in flow systems, in order to compare their quality to batch products, demonstrating effective size control in nanomaterials flow synthesis, demonstrating the ability to synthesize increasingly complex nanomaterials targets, and fully characterizing the throughput available using these methods.[37] Unfortunately, the flow reactor approach cannot be generalized to the preparation of all nanomaterials, but for the solution-based syntheses of ligand-stabilized nanoparticles, flow reactors provide a number of potential advantages for increasing scale and improving synthetic control.

Developing Scalable, High-Throughput Purification Methods. Traditional laboratory scale nanomaterials purification methods (solvent washes, column chromatography, dialysis, etc.) are not compatible with industrial scale chemical purification, being time and solvent intensive, hard to scale, and limited in their size and shape separation.[3,34,84,85] In the research laboratory, the material efficiency and throughput of the purification method are secondary considerations,[3] but the purification method must provide sufficient pure material (in dimensions and compositions) so that the composition and properties of the material can be determined unambiguously.[11] In contrast, the production of functionalized nanoparticles will demand that pure materials can be prepared rapidly and with efficient solvent use, because any significant generation of solvent waste incurs additional cost.

The sheer volume of waste associated with the laboratory scale purification of functionalized nanomaterials by traditional methods makes a strong argument for the development of new purification techniques.[18] Anastas has previously shown (*via* calculation of the E-factor for different nanomaterials syntheses) that the solvent volumes

used during the purification of ligand-stabilized nanomaterials by the conventional approaches given above often significantly exceed (sometimes by orders of magnitude) the amount of solvent generated in the synthesis of the nanomaterials themselves.[18] It is not uncommon to see purification methods reported where up to 15 L of solvent may be required to prepare 1 g of functionalized gold nanoparticles.[3,18] This amount of solvent waste spent during purification is entirely unacceptable in the production of functionalized materials, and this makes the rapid and efficient purification of functionalized nanomaterials an area of infrastructure and technology development where entirely new approaches will have to be developed before production methods can be realized.

As a consequence of the limitations of conventional NP purification methods, recent nanomaterial purification research has primarily focused on adapting entirely new purification approaches from other disciplines to increase throughput, reduce solvent waste, or improve size/shape separation.[86-89] Recently, there has been an increasing interest in using flow-based techniques to purify nanomaterials.[34,86,89] These flow-based approaches are actually highly varied and have exploited various strategies ranging from tangential flow in commercially available capsules[34] (diafiltration, *vide infra*) to nanotextured surfaces in microfluidic devices.[89] Some of these flow-based purification techniques have significantly increased the throughput associated with purification, and permit water-soluble nanomaterials to be purified without recourse to organic solvents.[34] Biological purification methods have also been a source of inspiration to improve size/shape separation. Gel electrophoresis and density gradient centrifugation has

successfully been used to separate various shapes and sizes of gold, silver, and semi-conductor nanoparticles, but are not easily scaled, and do not provide high-throughput methods for purification.[86-88]

Of the new techniques proposed for nanomaterial purification, diafiltration is among the most appealing, providing rapid separation of products from precursors, and eliminating the need for organic solvents as eluents in some cases.[34] Diafiltration utilizes a tangential flow method for separation, where nanomaterial solutions are forced through a polymer membrane, and small byproducts and unreacted starting materials exit through pores in the sides of the membrane. In 2006, Sweeney et al. reported a method using tangential flow membranes (with various pore sizes) to rapidly purify samples of water-soluble gold nanoparticles by diafiltration.[34] These capsules rapidly remove free ligand, salts, and some byproducts from aqueous nanoparticle samples. In addition, the commercially available diafiltration cassettes can be used to achieve the size fractionation of gold nanoparticles with 1.0 nm size resolution, depending on the size of the NPs.[34] This technique represents a remarkable savings in both the amount of solvent used (4 L water/gAuNP versus 15L/g AuNP) and the time required (fifteen minutes versus three days) to purify a nanoparticle sample versus more traditional approaches, such as chromatography or dialysis.[34]

Though the advantages of diafiltration are significant, application of the current formulation of the method is somewhat limited. The principal drawbacks associated with this approach, are that, at present, no analogous membrane capsules exist for the purification of organic-soluble nanoparticles and the ability to separate different sizes of

nanoparticles are limited by the resolution available in the capsule membrane pore sizes. In practice, this means that while suitable cassettes are available to separate 3.0 nm AuNPs from 1.5 nm AuNPs, these membranes cannot be used to separate anisotropic nanomaterials from isotropic materials if they are of similar size in one dimension (e.g. 10.0 nm spherical AuNPs from gold nanorods that are 10.0 x 50.0 nm).[34] Nevertheless, if the diafiltration method can be translated to the purification of organic-soluble NPs, this scalable and rapid separation method may serve as an excellent prototype for the high-throughput purification of gram-scale batches of nanomaterials.

The development of new nanoparticle purification strategies is moving at a relatively gradual pace, although the angles from which the challenges are being addressed has diversified.[34] Since 2005, only a handful of new purification strategies have been proposed. Considering the reliance in most research laboratories on conventional NP purification techniques that are solvent and time-intensive, much more research on nanoparticle purification will be necessary in order to develop applicable strategies for purification during NP production. Many challenges still need to be addressed in this area, particularly developing reliable methods for separating different NP shapes, developing high-throughput purification techniques for organic-soluble NPs, and separating nanoparticles with similar size, but disparate surface chemistry. It is likely that new purification strategies addressing the current frontiers in nanomaterial separation will evolve along with the community's understanding of how nanoparticle size, shape, and functionality dictate the interactions of the particle with its environment.

Progress in the Development and Implementation of Production Technology and Infrastructure. Although cost-effective, scalable nanoparticle synthetic methods have not yet been achieved, significant progress has been made in developing strategies and infrastructure that can provide for effective monitoring, scale-up, and purification during production. The application of new *in situ* monitoring techniques (such as SAXS) that permit real-time determinations of NP size and dispersity provides an opportunity to quickly accurately monitor NP properties using non-invasive techniques. In addition, the development of automated reactor systems (such as WANDA) for nanomaterial synthesis has been shown to be a viable approach for the rapid synthesis and analysis of many classes of nanomaterials. The development of new purification methods for nanomaterials has proceeded gradually, however, with only a handful of new techniques demonstrated in the last five years. Of these methods, diafiltration provides the most applicable example of how flow purification techniques can be used to purify nanomaterials rapidly and with minimal organic solvent waste.

Summary and Outlook

The large-scale production of high-performance functionalized nanomaterials requires the development of cost-effective, benign, and scalable synthetic methods. The majority of existing nanomaterials synthetic methods are controlled using inefficient, hazardous chemical strategies that are ill suited to large-scale production. The challenges associated with developing suitable nanoparticle production methods include reducing the hazard associated with these syntheses, developing high-performance nanoparticles from benign chemicals, developing high-throughput/low waste purification methods, and

improving synthetic efficiency. The principles of green chemistry provide a framework that can guide the evolution of nanomaterials synthesis into the production phase, but clever chemical strategies are necessary to effect these alterations.

Recently, the application of green chemistry principles to ligand-stabilized nanoparticle synthesis has provided an increased number of synthetic techniques with improved process safety, product safety, and decreased the volume of waste generated during synthesis. These advances include the elimination of pyrophoric reagents from common syntheses, the design of quantum dots with non-toxic core materials, and increased synthetic throughput with decreased organic waste. One area that has remained more problematic to address, however, is the underlying efficiency of the nanoparticle synthetic reactions. Improving the reaction efficiency (atom economy, material efficiency, energy efficiency) of nanoparticle syntheses will require a more detailed understanding of nanoparticle formation mechanisms. Recent mechanistic insights into nanoparticle growth have already been applied to improve synthetic control over nanoparticle properties, but improving the atom economy of nanoparticle synthetic reactions will required more detailed insights into nanoparticle growth chemistry. These insights may be enabled by the application of new NP monitoring techniques, such as in situ TEM analysis and the application of small-angle x-ray scattering to assessing the growth kinetics of metal nanoparticles.

Despite the gradual progress in developing cost-effective nanoparticle synthesis methods, significant progress has been made in developing infrastructure that will enable the transfer of nanoparticle syntheses to production scale processes, including new

strategies for reaction scale up, high-throughput purification, and real-time monitoring. Significant new approaches include the development of *in situ* methods for quantitative size analysis, new purification approaches that significantly increase throughput (requiring only minutes to achieve pure materials), and the development and implementation of automated nanoparticle reactors. This evolution in infrastructure means that as cost-effective syntheses are devised, general methods for quality control and in-line purification may have already be in place, enabling a more rapid transition from pilot studies to manufacturing than would ordinarily be possible in such a young industry.

Transition 1: Characterization Techniques for Nanomaterials

Because the properties of nanomaterials depend as much on their shape and dimensions as on their chemical composition, the accurate characterization of nanomaterials is important both in the synthesis of new materials and the investigation of nanomaterial formation.[3,8] Previously, characterization of nanomaterials has been primarily important in understanding the origin of size and shape-dependent optical, electronic, and magnetic properties.[3,8] Currently, these methods are becoming increasingly utilized to confirm that similar materials produced by different synthetic techniques possess equivalent structure and composition, the characterization of nanomaterials prior to deployment in applications, and monitoring in mechanistic investigations.

Typically, the characterization of nanomaterials (specifically gold nanoparticles) focuses on three aspects of nanomaterial structure: particle size, particle shape, and the composition of the molecules adsorbed or bound to the particle surface (surface chemistry).[3,8] There are several common techniques used in the assessment of each structural aspect. Microscopy techniques are most commonly used to address shape and size (transmission electron microscopy or scanning electron microscopy), though the same information can frequently be inferred from optical characterization techniques, such as UV-vis absorbance spectroscopy or fluorescence spectroscopy.[3,8,76] Characterizing nanoparticle surface chemistry is still an area where new techniques and insights are currently being developed. The unique size of nanomaterials complicates their surface chemistry characterization.[8] Techniques common in the analysis of single molecules (e.g.-NMR spectroscopy), are applicable only in certain size regimes, and yet the surface of the nanoparticles cannot always be completely characterized by the use of analytical techniques developed for bulk materials (e.g.- X-ray photoelectron spectroscopy).[3,8] Thus, many techniques are often used in synchrony to infer the surface chemistry composition and structure possessed by the particles. Typically, X-ray photoelectron spectroscopy (XPS), thermogravimetric analysis (TGA), FTIR, and NMR spectroscopy are used in concert to develop a basic picture of gold nanoparticle surface chemistry.[90]

There are many challenges remaining in the successful characterization of gold nanoparticles in various media and situations, however, one of the biggest challenges involves the *in situ* determination of gold nanoparticle properties, particularly size and

shape. Traditionally, UV-vis has been the most ubiquitous of these techniques, providing qualitative real-time determinations of nanoparticle size and shape, but the use of this technique for quantitative analysis is restricted to specific size regimes. Small-angle X-ray scattering (SAXS) has recently been shown to provide real-time quantitative monitoring of nanoparticle size and shape, and is rapidly gaining popularity in kinetic investigations of nanoparticle formation reactions.[64,76] In this section, we will provide brief descriptions of the theory, utility, and limitations of several nanoparticle characterization techniques (first *ex situ* techniques, then *in situ* techniques) that will be referred to frequently throughout this dissertation.

Ex Situ Nanoparticle Characterization Techniques: TEM and XPS

Transmission Electron Microscopy (TEM). Historically, transmission electron microscopy is the most ubiquitous nanoparticle characterization technique. This technique provides a visual determination of nanoparticle size and shape, providing the core material has a high enough atomic number (or is thick enough) to provide sufficient contrast to visualize the particle.[3,91] In TEM, a sample under high vacuum is exposed to electrons from a high-intensity electron source (frequently a heated tungsten filament). The electron beam is focused and excluded respectively by various lenses and apertures in the microscope, much the same way that light is collected and excluded by lenses and apertures in a light microscope.[91] The electrons easily pass through the extremely thin films used as sample mounts, but scatter off, or are absorbed by high-Z nanomaterials, providing silhouetted images of the nanomaterials from which size and shape can be easily determined. Substrates used for sample mounts are typically SiO or SiO_2 films that

are microns thick. TEM resolution is typically on the order of Angstroms, permitting the visualization of ordered arrays of atoms within the nanomaterials in some cases.[3,8,90]

In the context of nanomaterials analysis, TEM is typically used for establishing the average size and shape. The size of gold nanoparticles is typically reported as the mean core diameter (d_{core}), which is typically given along with the standard deviation in core diameter (also referred to as the dispersity, or sometimes polydispersity).[90] A successful determination of the particle size distribution usually requires the analysis of an extremely large number of nanoparticles (usually N>500) in order to produce robust statistics. The core diameter can be measured in a number of ways, but this process can be somewhat simplified by using image analysis software to determine the core diameter of the AuNPs (Figure T1.1). Although the core is clearly visible, the ligand shell typically cannot be seen by TEM analysis.

The principal limitations associated with TEM analysis relate to the number of measurements that need to be made to develop a representative measure of particle properties.[3,8,90] In addition, TEM analysis requires appropriate sample preparation in order to produce accurate results.[76] Prolonged exposure of particles to the electron beam also can cause sample damage, and skew the results of the analysis. Ultimately, TEM provides one of the most accurate determinations of particle size and shape, but requires extensive analysis time and sample preparation.

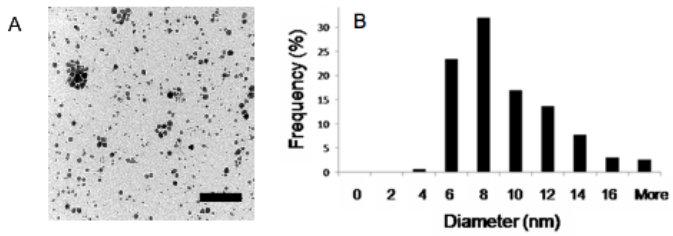

Figure 1.7: Characteristic TEM data from the visualization of gold nanoparticles. (A) TEM micrograph. (B) Size distribution histogram that summarizes the results of the size analysis of the micrographs. The scale bar shown in (A) is 100 nm.

X-ray Photoelectron Spectroscopy. X-ray photoelectron spectroscopy (XPS) is the principal tool for the analysis of the surface chemistry of ligand-stabilized nanomaterials, as XPS can provide compositional analysis, a determination of oxidation states, and determination of empirical formulas for the materials.[90,91] XPS analysis has been shown to effectively provide accurate determinations of the number of ligands bound per atom of the core material for AuNPs between 0.8 nm and 10.0 nm in diameter.

XPS involves the excitation of inner shell electrons within a material by bombarding the samples with a monochromated X-ray source. The ejected electrons are captured by the detector, and their kinetic energy and the frequency of their emission are both recorded. The kinetic energy of the ejected electrons can be related to their binding energy using the following equation (1.1):

$$E_{binding} = E_{photon} - (E_{kinetic} + \phi) \qquad (1)^{7}$$

Where E_{photon} is the energy of the incident X-rays, $E_{kinetic}$ is the kinetic energy of the ejected electron, and ϕ is the work function for the spectrometer.[91] The binding energy

for each element analyzed can therefore be obtained from the energy of the ejected electrons, which provides a measure of the relative oxidation states of the different elements. However, only electrons generated within approximately the top 10 nm of the analyzed material are successfully captured by the detector. Electrons excited farther down in the material will be reabsorbed or trapped, meaning that XPS is generally only used to analyze the surface of materials, or approximately the depth of one nanoparticle.

An example of the sulfur S2p region of a ligand-stabilized gold nanoparticle XPS spectrum is shown in Figure T1.2. The signal for each type of sulfur atom appears as a doublet. In this spectrum, three types of sulfur atoms are represented, with the species with the lowest binding energy (162.5 eV) being the most reduced of the sulfur atom types, the species at 163.5 eV being slightly more oxidized, and the species at 168.6 eV being a strongly oxidized sulfur species. The area of these doublets can be ratioed to that of other species observed in the overall XPS spectrum (also called a survey scan) to determine the relative composition of the material. From these data, we can determine the S:Au ratio in order to determine the average number of thiolate ligands present on these AuNPs.

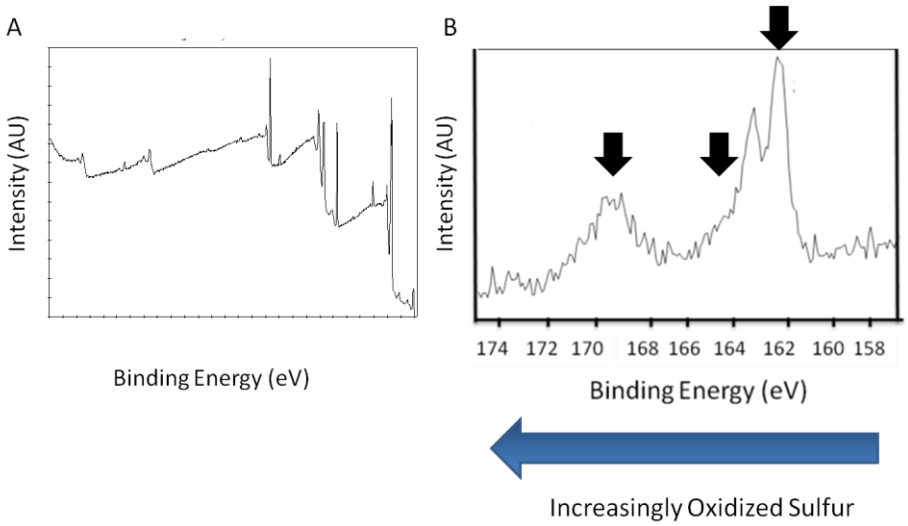

Figure 1.8: Representative XPS analysis of the composition of ligand-stabilized gold nanoparticles. (A) The survey scan provides a quick scan of the entire spectrum, providing a cursory evaluation of the elements present. Areas of interest are then analyzed in detail. (B) XPS region scan for the S2p region of the XPS spectrum (158.0-174.0 eV). Three sulfur species are indicated, with the more oxidized sulfur species occurring at higher binding energies.

Other Ex Situ Characterization Techniques. The use of XPS analysis to determine nanoparticle composition is often complemented by some combination of FTIR, NMR, and TGA of purified particle samples. FTIR gives qualitative information about the presence of specific chemical functional groups in the ligand shell. NMR spectroscopy provides similar information in certain AuNP size regimes, and depending on ligand length. TGA provides information about the mass of organic material associated with gold nanoparticles, providing another means to determine the number of ligands present on the gold nanoparticle surface.

In Situ Characterization Techniques: UV-vis Absorbance Spectroscopy and SAXS

UV-vis absorbance spectroscopy. UV-vis absorbance spectroscopy has long been one of the most common methods used to quickly assess the size and shape of the gold nanoparticle core.[3,8,73,74] Because of the AuNP size and shape-dependent optical properties, the position and intensity of features in the absorbance spectrum provide a quick estimate of the size of the AuNPs in the sample. AuNPs with core diameters of 3 nm or greater can quickly be identified by the presence of a plasmon absorption occurring near 520 nm, and the wavelength of maximum absorption will increase along with the intensity of the absorption in response to AuNP core size.[3] UV-vis absorbance spectroscopy is frequently used to qualitatively monitor changes in nanoparticle size over time by studying the position, intensity and width of the plasmon absorbance, though in certain size ranges it has also been shown that AuNP size and concentration can be quantitatively determined from the sample's absorbance data.[3] Because of the rapid acquisition times associated with this analysis and the relationship between absorbance features and nanoparticle properties, UV-vis absorbance spectroscopy is a common technique for in situ nanoparticle monitoring. Although UV-vis absorbance rapidly provides information on AuNP size and concentration, it is difficult to extract any data on the size dispersity of the sample from the UV-vis data.

Small-Angle X-ray Scattering (SAXS). In order to obtain quantitative determinations of nanoparticle size, dispersity, and concentration, small angle x-ray scattering is frequently

used to analyze nanoparticle samples. SAXS has traditionally been used to complement TEM analysis and UV-vis absorption spectroscopy in AuNP size analysis.[90] SAXS-based size analysis of AuNP samples has been shown to provide good agreement with TEM analysis of AuNP size in a variety of media.[76] Much like UV-vis absorption spectroscopy, SAXS can be used to probe the characteristics of an entire nanoparticle sample, rapidly, and with no sample preparation required. Recently, SAXS has also been utilized for the *in situ* analysis of nanoparticle growth kinetics.[64] The primary drawback in SAXS analysis is that concentrated samples, extended acquisition times, or extremely intense X-ray radiation sources (e.g.-synchrotron radiation sources) are required for nanoparticle size analysis.

In SAXS analysis, the size of the AuNPs in the sample under study is related to the intensity of X-rays scattered by the scattering vector "q."

$$q = (4\pi/\lambda) \sin(\theta/2) \qquad (2)^{76}$$

In this equation, λ is the wavelength of the X-ray source, and θ is scattering angle. The scattering angle is inversely correlated with the size of the nanoparticles under observation. The collected SAXS data is typically reported as a plot of intensity as a function of the scattering vector, as shown in Figure 1.9. In order to determine the size of the AuNPs under investigation, the data is modeled according to equation 1.3.

$$I(q) = (\Delta\rho)^2 (n\int f(r)\, V(r)^2\, P(q,r)\, dr) \qquad (3)^{76}$$

Here, V(r) and P(q,r) are the volume and form factor for a sphere of radius r, while f(r) is the size distribution of the particle sample. $\Delta\rho$ is the difference in electron density between the particle material (gold) and the solvent (water). The relative concentrations of gold nanoparticle samples at each time can be related to the intensity of the scattering at q=0 by equation 1.4.

$$I(0) = N(V)^2\Delta\rho^2 \qquad (4)^{76}$$

In this equation, N is the number of scatterers present in the volume of the sample analyzed at any given time. By determining N, and dividing by the volume of the solution element analyzed, the relative concentration of AuNPs at any residence time can be determined.

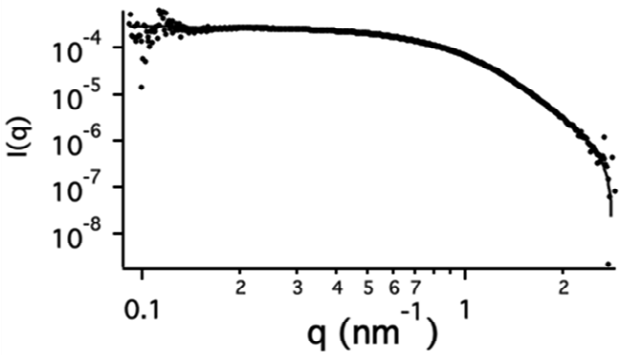

Figure 1.9: Scattering intensity versus scattering vector plot obtained for a 5.0 AuNP sample analyzed by SAXS. The scattering data can be modeled to provide the size and size distribution of the AuNP sample.

Because of the unique size regime and compositions of nanomaterials, it is rare that a single characterization technique can entirely assess even one aspect of the materials physical properties in a conclusive manner. Instead, suites of characterization techniques are typically used in concert to produce data sets that provide the minimum amount of characterization data necessary to fully assess a sample's properties.[3,8] In this dissertation, some combination of the techniques described above is always used to assess the size and surface chemistry of the AuNPs. In Chapters II and III, *ex situ* characterization techniques (TEM, TGA, FTIR, and XPS) are used to establish nanomaterials properties in order to verify the composition and size of synthesized materials, and to investigate the effect of reaction parameters on ligand shell composition. In Chapters IV-VI, greater emphasis is placed on using *in situ* characterization techniques (UV-vis and SAXS) to monitor nanoparticle properties as they are synthesized, with support, where appropriate, from *ex situ* characterization methods.

Transition 2: The Synthesis of 5.0 nm Thiol-Protected AuNPs and the Synthetic Utility of Ligand Precursors

Spherical gold nanoparticles are commonly applied materials because of the size-dependent optical and electronic properties.[3,20] Gold nanoparticles with core diameters greater than 3.0 nm display a size-dependent optical behavior known as Surface Plasmon Resonance (SPR) which results from the interaction of incident radiation with conducting electrons on the surface of the gold nanoparticle, resulting in a dipolar oscillation of the electron density on the AuNP surface.[20] This phenomenon is manifested as an absorption in the visible portion of the electromagnetic spectrum centered at 520 nm, but the

intensity and wavelength of maximum absorption depend on the size of the AuNP.[20] The SPR absorbance can first be seen in solutions of 3.0 nm AuNPs, but becomes significantly more intense for AuNPs with core diameters greater than 5.0 nm. The SPR absorbance is the basis for many different gold nanoparticle applications, including colorimetric sensing and microscale optical devices, other applications relying on the light absorbance and scattering properties of gold nanoparticles.

The surface chemistry of gold nanoparticles (primarily the composition of the ligand shell) provides a method for mediating the interaction of gold nanoparticles with their environment, including their interactions with surfaces and analytes.[3,8] Because of this, precisely controlling the surface chemistry of AuNPs is an important aspect of nanomaterials synthetic chemistry.[3,8] When precise control of the ligand shell composition is desired, functionalized thiols are generally used as nanoparticle ligands. The functional group displayed by the thiol (the ω-functionality) plays a role in determining the solubility and chemical behavior of the AuNPs. In addition, thiols and phosphine-protected AuNPs possess exceptional stability, and can be manipulated essentially as single molecules, making ligand-stabilized AuNPs preferred for many applications over AuNPs stabilized by adsorbed polymers or ions.[3] However, the synthesis of large thiol-protected AuNPs is difficult to achieve using existing synthetic strategies.

Generally, thiol-protected gold nanoparticles are synthesized by one of two synthetic strategies: direct synthesis or ligand exchange. AuNPs with core diameters greater than 5.0 nm cannot be synthesized by direct synthesis using thiols.[3,91] The thiol

ligand shell forms so rapidly on the particle surface that particle core diameters do not exceed 4.0 nm (strong passivation of nanoparticle growth). Ligand exchange involves the synthesis of a large AuNP using a weak passivant such as citrate, ascorbic acid, or amines, which is then exchanged for a functionalized thiol to produce a large thiol-protected AuNP.[3] However, the synthesis of large AuNPs by ligand exchange methods is a problematic reaction. In addition to the additional time and solvent required for the ligand exchange to proceed, aggregation and loss of product during the ligand exchange is a frequent problem.[3] Therefore, the development of a direct synthetic method for thiol-protected 5.0 nm (and larger) AuNPs would represent a significant synthetic accomplishment that addresses a significant limitation in the synthesis of functionalized gold nanomaterials.

One strategy for achieving the direct synthesis of large AuNPs involves the use of a ligand that combines the ability to weakly passivate nanoparticle growth (allowing the growth of large particles), with the ability to be converted to a covalently-binding ligand (producing thiolate-protected AuNPs at the end of the synthesis). There are a number of organic molecules possessing functional groups that could serve this purpose. These ligand precursor compounds are referred to as *masked* or *protected thiols*, and contain a thiol (R-SH) protected by another functional group. The most common protected thiols include Bunte salts (alkyl thiosulfates, R-S-SO_3^-), thioactetates (R-S-COR'), and thiocyanates (R-S-CN). All of these compounds have been shown to form thiolate monolayers on gold films without any additional reagent input. During monolayer formation, the protected thiol adsorbs to the gold film, and then eliminates the protecting

group to form a thiolate monolayer. We hypothesized that if the protected thiols produce thiolate ligand shells on gold nanoparticles by a similar process, then large thiol-protected AuNPs could be synthesized directly using these molecules as ligand precursors. In this dissertation, we explore the use of Bunte salts as ligand precursors in the direct synthesis of thiol-protected gold nanoparticles. We also investigate the chemistry of thiolate ligand shell formation on the surface of gold nanoparticles, and examine the growth kinetics of the gold nanoparticle core.

Chapter II describes the development of a direct synthetic strategy for large thiolate-protected AuNPs using Bunte salts as ligand precursors. Chapter III details an investigation of how synthetic conditions influence the formation of the ligand shell. Chapters IV and V describe how the direct synthesis is adapted for use in two different flow reactor setups that provide improved opportunities for the synthetic control of nanoparticle properties and *in situ* monitoring. Chapter VI describes the use of a capillary flow reactor with *in situ* SAXS and UV-vis monitoring to follow the growth of gold nanoparticles in real time. Chapters II-VI include co-authored material, as indicated in the preface to each chapter.

CHAPTER II

DIRECT SYNTHESIS OF LARGE WATER-SOLUBLE FUNCTIONALIZED GOLD NANOPARTICLES USING BUNTE SALTS AS LIGAND PRECURSORS

Note: The information presented in this chapter has previously been published in *Langmuir* **2010** (Lohse, Dahl, and Hutchison). The manuscript has been reproduced with permission of the author. The work described in this chapter is that of the author. The study was co-authored with Jennifer Dahl and James Hutchison. Jennifer Dahl had the initial idea for using Bunte salts as ligand precursors in the synthesis of gold nanoparticles and performed the first proof of concept synthesis. Jim Hutchison provided editorial guidance and advice.

Introduction

Gold nanoparticles possess a variety of size-dependent optical phenomena that can be harnessed for applications such as the detection of analytes in solution, construction of microscale optical devices, and biomedical assays or treatments.[1-6] Effective application of those properties is realized by controlling the nanoparticle surface chemistry (functionality).[2,4,7,8] The principal attribute of gold nanoparticles (AuNPs) harnessed in these applications is the surface plasmon resonance (SPR)

phenomenon that manifests itself as an intense absorption at 520 nm.[2,9] The intensity of this absorption and energy at which it occurs are determined by the size of the AuNP, with particles with d_{core} > 5 nm possessing the most intense SPR absorptions, and therefore the most utility in many cases.[2,9] Because AuNPs possess such important size-related effects, the ability to control the size of the AuNP is one of the most important and most thoroughly researched dimensions of an effective nanoparticle synthesis.[2,4,6,10,11,12] However, for many applications, precise size control is useless if the functionality of the particle cannot also be controlled. It is the surface chemistry of the particle that enables many of the applications detailed above.[4,6,13]

A number of cunning chemical strategies have been developed for synthesizing functionalized gold nanoparticles of various sizes. Yet, even the most commonly used techniques (ie. the Brust synthesis and ligand exchange techniques) still suffer from limitations that make it a challenge to synthesize large (d_{core} > 5 nm) AuNPs with precisely controlled surface chemistry.[4,6,8,9,14,15] In the Brust synthesis, a direct synthetic method, gold nanoparticles are synthesized in the presence of functionalized thiols, producing thiolate monolayer-protected AuNPs.[7,10,12] However, because AuNP growth is quickly passivated by the formation of thiolate bonds, it is difficult to produce AuNPs with core diameters greater than 4 nm in this way.[4,8,15] In contrast, ligand exchange techniques require a step-wise synthetic approach that involves producing a gold nanoparticle stabilized by an exchangeable ligand (citrate, phosphines, or amines) that is replaced with a functionalized thiol in a subsequent step to yield the monolayer-protected particle.[2,4,15] In this case, the method has been shown to be highly effective in the

synthesis of smaller gold nanoparticles (d_{core}< 2 nm). However, in the case of large AuNPs, incomplete ligand exchange becomes a problem and the reaction is sensitive to changes in ionic strength and interactions between incoming and outgoing functionalities.[4,15,16,17] The differences in reaction efficiency may be related to the curvature of the particle, reactivity of the particle surface, and other size-related changes in the surface chemistry of the particle.[4,6,15,16,17] In short, it is still synthetically challenging to produce large functionalized gold nanoparticles and there is a significant need for the development of direct syntheses that produce specifically-functionalized gold nanoparticles with d_{core} > 5 nm.

We explored a new approach towards the synthesis of large functionalized AuNPs, inspired by the work of Murray with functionalized alkyl thiosulfates (Bunte salts).[18-21] Several years ago, Murray demonstrated that thiol-stabilized AuNPs could be synthesized using Bunte salts as ligand precursors because Bunte salts eliminate sulfite to form a thiolate monolayer on the surface of the gold nanoparticle.[18,19,20] Murray demonstrated the synthesis of small gold nanoparticles (d_{core}~3 nm) using this method and found that both alkane and sulfonic acid functionalities could be displayed on the surface of AuNPs using Bunte salts as ligand precursors.[18,19] Murray and others postulated that, during synthesis, the Bunte salt first physically adsorbs to the surface of the developing nanoparticle, and then eliminates sulfite to form a thiolate linkage to the gold core.[19-21,22] Based on these reports, we hypothesized that the weaker, non-covalent, interaction between the nanoparticle and the Bunte salt would allow the developing nanoparticle to grow to a larger diameter before becoming passivated by the thiolate

monolayer on the particle's surface. These slow passivation kinetics could allow for a direct synthetic route to functionalized gold nanoparticles with large core diameters.[19-21,23] In addition, the Bunte salt ligand precursors would provide an excellent delivery platform for a variety of hydrophilic functional groups. Despite the promise of this synthetic method, its versatility has not been explored.

In the present study, we have developed a direct synthesis for large (up to 20 nm) functionalized gold nanoparticles. The synthesis takes advantage of the slow passivation kinetics of Bunte salts to extend the size range of functionalized AuNPs above what is typically available in the Brust method. We show here that a wide variety of functionalized Bunte salts can readily be prepared from functionalized organohalides, and that these ligand precursors indeed produce monolayer-protected particles with the desired ω-functionality. We demonstrate that Bunte salts produce larger particles than thiols under the same reagent conditions. We report the effect of ligand precursor: Au ratio, reducing agent concentration and temperature on particle diameter and dispersity. These reaction parameters have inter-related effects on the core diameters of the particles produced. The optimized synthesis can be tailored to produce AuNPs in a variety of desired core diameters between 1.5 and 20.0 nm, and can be prepared with a variety of functional groups covalently anchored to their surface. For this study, three types of functionalities were chosen: a biologically relevant neutral hydrophilic ligand (analog of mercaptoethoxyethoxyethanol, MEEE BS, **1,** Fig. 1), a carboxylate ligand (analog of 9-mercaptononanoic acid, MNA BS, **2**), and a quaternary ammonium ligand (the Bunte salt analog of mercaptopentyl(trimethylammonium) chloride, MPTMA BS, **3**).

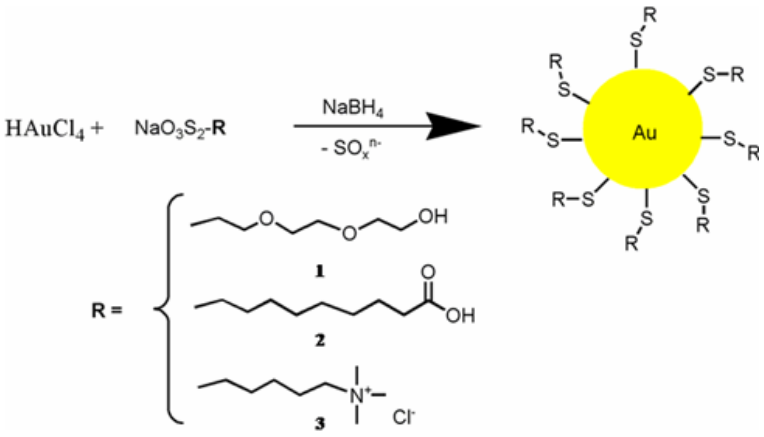

Figure 2.1: General reaction scheme for the synthesis of gold nanoparticles using Bunte salts as ligand precursors. Following adsorption to the gold surface, the ligand precursor eliminates an oxidized sulfur species to provide a thiolate attachment to the surface of the gold nanoparticle (AuNP). The facile nature of the Bunte salt synthesis makes this synthetic technique a powerful tool for the direct synthesis of large hydrophilic functionalized gold nanoparticles. The ligand precursors used in this study represent three important classes of hydrophilic functionalities: an oligoethylene glycol, MEEE BS (**1**), a carboxylic acid, MNA BS (**2**), and a quaternary ammonium species MTMAP BS (**3**).

Experimental

Materials. All materials were obtained from their suppliers as given below and used as received: Hydrogen tetrachloroaurate hydrate (Strem), 2-[2-(2-chloroethoxy)-ethoxy]ethanol 99% (Aldrich), 5-bromopentyl(trimethylammonium bromide) 99% (Aldrich), 9-bromononaonic acid (RDC/RIC), and sodium borohydride caplets (Aldrich, 98%). Nanopure deionized water (Millipore 18 MΩ) was used for the preparation of stock solutions and as a solvent for nanoparticle synthesis. 2-[2-(2-mercaptoethoxy)-

ethoxy] ethanol was synthesized using previously reported methods.[24] To remove free ligand, small molecules, and ionic species from the solutions of finished nanoparticles, particle solutions were purified by diafiltration in a 10 kD membrane cassette (PALL).[24]

Analysis of Nanoparticles. Purified nanoparticle solutions were analyzed by UV-vis absorption spectroscopy to gain a quick estimate of size and dispersity. The NPs were then analyzed by transmission electron microscopy (TEM) by imaging the dropcast purified samples on a Philips CM-12 electron microscope using etched SiO_2 TEM grids.[25] Final statistical size distributions were arrived at by TEM-based size analysis of the purified particles ($n > 900$ particles, with the exception of particles with $d_{core} > 20$ nm, where $n > 100$). The size analysis of the particles was performed using Image J analysis software.[26] For TGA, XPS, and FTIR analysis, the excess ligand was removed from solution by diafiltration.[24] The purified samples were then lyophilized and the powdered solid was used to make a KBr salt plate (FTIR, 1.00 g of KBr to 100 mg of lyophilized particles) or 2.00 mg was taken for TGA. For XPS analysis, the diafiltered nanoparticle solutions were concentrated and three 500 µL depositions of these solutions were dropcast onto a clean chromium-coated silicon wafer. Each 500 µL droplet was allowed time to dry in between depositions.

Thermogravimetric analysis (TGA) was performed on a TA Instruments 2950 Thermogravimetric Analyzer. FTIR spectra were obtained using a Nicolet Magna 550 Fourier Transform Infrared Spectrometer. XPS analysis was performed on a Thermo Fisher Escalab 250 X-ray Photoelectron Spectrometer. UV-vis absorption analysis was

performed on an Ocean Optics cell holder and USB2000 detector, with a Micropack DH-2000 light source.

Synthesis of Bunte Salt Ligand Precursors. We synthesized a variety of ligand precursors using the Bunte salt synthetic procedure given by Murray and others.[18,19] To synthesize the Bunte salt, the appropriate organohalide precursor (2.0 g) and sodium thiosulfate (0.80 molar equivalents) were dissolved in 150 mL of water and heated to reflux for four hours. The water was then removed by rotary evaporation and drying on a vacuum line. The crude products were purified by dissolution in ethanol, followed by gravity filtration (Supporting Information). [19] The purified ligand precursors were analyzed using ^{1}H-NMR spectroscopy (300 MHz, Varian). TGA was employed to verify the removal of the sodium halide byproduct.

Standard Nanoparticle Synthesis Conditions. Gold nanoparticles were synthesized using a modified procedure from that given by Murray et al.[19] All reactions were carried out in aqua regia-cleaned 100 mL round-bottomed flasks. Briefly, hydrogen tetrachloroaurate trihydrate (0.1 mmols) was combined with the Bunte salt ligand precursor in L:Au ratios ranging from 4:1 to 1:100 in 50 mL water. This gave solutions which varied from clear and colorless to light orange or brown in the case of higher L:Au ratios. The reaction mixture was allowed to stir for ten minutes before an aqueous solution of 0.1 M sodium borohydride (10.0 molar equivalents with respect to [$AuCl_4^-$]) was added to the reaction mixture. This addition immediately induced a color change to deep red indicating the formation of gold nanoparticles greater than 5 nm in diameter, or in the case of higher L:Au ratios, deep brown, indicating the formation of smaller

particles. The particle solutions were left to stir for an additional three hours. Each crude nanoparticle solution was purified by passing it through a coarse frit (in the rare event that this was necessary to remove visible aggregates) and diafiltering the reaction mixture with 20 volume equivalents of nanopure deionized water to remove the excess free ligand precursor.[24]

Synthesis of MEEE-Stabilized AuNPs from Thiols. In order to compare the core diameters of particles prepared using thiols to particles prepared using Bunte salts under the same synthetic conditions, MEEE-stabilized gold nanoparticles synthesized using thiols were prepared using the reagent conditions described above, with the exception that the thiol, 2-[2-(2-mercaptoethoxy)-ethoxy] ethanol, was employed as the ligand.[19,24]

Effects of L:Au Ratio, Temperature and Reducing Agent Concentration on AuNP Core Diameter and Polydispersity. In order to explore the effect of L:Au ratio, temperature, and borohydride concentration on particle diameter and polydispersity for the preparation of functionalized AuNPs from Bunte salt ligand precursors, small reaction mixtures (20.0 mL total volume, and a concentration of 0.0025 M $HAuCl_4$) were prepared with molar L:Au ratios of 1:6, 1:4, 1:1 and 1:3. For each of these L:Au values, the reaction was run at two temperatures: 60ºC (heated oil bath) and 2ºC (ice bath), and two sodium borohydride concentrations: 10 molar equivalents with respect to Au and 1.0 molar equivalent with respect to Au. The gold complex and ligand precursor were fully mixed in nanopure deionized water by stirring for ten minutes. Sodium borohydride (0.1 M aqueous solution) was added to the reaction mixture by the rapid addition of 100 µL or

1.00 mL by micropipette. The solutions were then stirred for three hours, diluted 1:1 (v:v) with nanopure water and analyzed by UV-vis and TEM.

Demonstration of Accessible Size Ranges Using MEEE BS (1) as Ligand Precursor. In order to demonstrate the entire range of accessible core diameters provided by this synthesis, we synthesized a variety of different size MEEE particles using the standard synthetic conditions described above, but varied the procedure as follows. In order to synthesize the smallest particles, the reaction was carried out at 2° C, with a L:Au ratio of 3:1. Hydrogen tetrachloroaurate (0.1 mmols) were combined with the appropriate volume of a 0.1 M aqueous solution of the Bunte salt as described in the preceding section. This initial reaction mixture is a light brown, and the color darkens to a richer brown after the addition of 10.0 molar equivalents of borohydride. The reaction mixture was held at 2° C for one hour, and then the reaction was left to stir for a further two hours at room temperature. In order to synthesize slightly larger particles, a 1:1 L:Au ratio was employed and the reaction was run at room temperature. Upon borohydride addition, the solution turned a dark maroon color. To gain an estimate of the upper limit of accessible sizes, the synthesis was performed at elevated temperatures in the presence of a limiting amount of ligand precursor. These particles were synthesized by heating the tetrachloroaurate and Bunte salt solution (1:100 L:Au) to 60 °C for ten minutes prior to the addition of 10.0 molar equivalents of sodium borohydride, which caused the solution to turn from a very light yellow rapidly to red-violet, indicating the formation of larger AuNPs.

Synthesis of Large Functionalized AuNPs with Different Hydrophilic Functionalities. Gold nanoparticles functionalized by ligand precursors **1**, **2**, and **3** were synthesized using the standard procedure given above, using L:Au ratios of 1:6, 1:2, and 1:3 respectively.[19] The reactions were run at room temperature (24° C). In the case of ligand precursors MPTMA (**1)** and MNA (**3)**, a precipitate is sometimes observed at higher L:Au ratios prior to borohydride reduction. Initial investigations suggest that this precipitate is a Bunte salt-gold(III) complex (see Supporting Information), and that the formation of this complex does not preclude or complicate the formation of gold nanoparticles. Following sodium borohydride addition, the solutions become a deep red color, indicating the formation of large gold nanoparticles.

Results and Discussion

The goal of this study was to determine whether a direct synthesis for large (5-20 nm) water-soluble functionalized gold nanoparticles could be developed by taking advantage of the slow passivation kinetics of a masked thiol ligand precursor (Bunte salt). In order to gain some basic insight into the growth chemistry of the reaction, we undertook a series of screening experiments which examined the effect of the ligand precursor:Au ratio (L:Au), the reductant concentration, and the reaction temperature on the product AuNP size and polydispersity. Once we had identified suitable general reaction parameters, we set out to demonstrate the range of accessible core sizes available by this method. Finally, we demonstrated how the facile nature of the ligand precursor synthesis could be utilized to produce a wide variety of functionalized particles, and characterized the surface chemistry of the particles.

Comparison to Direct Synthesis with Thiols. We first tested the hypothesis that Bunte salt ligand precursors will allow for the synthesis of larger functionalized particles than the corresponding thiols. To test this, we compared the core size of particles obtained using our standard synthetic conditions when a hydrophilic Bunte salt ligand precursor (MEEE BS, **1**) was employed versus the thiol (2-[2-(2-mercaptoethoxy)-ethoxy]ethanol, MEEE). In both cases, the reaction was performed with 10 molar equivalents of sodium borohydride and a L:Au ratio of 1:6.

The difference in particle size that resulted when using the two ligands was immediately apparent. When the thiol was employed, the reaction produced a brown solution, indicating the formation of small nanoparticles. However, when the Bunte salt was employed, the product solution was red, consistent with the formation of large AuNPs. UV-vis absorption spectroscopy analysis of the solution showed a very shallow plasmon absorption for the thiol-derived particle solution (Fig. 2.2), but shows a strong plasmon absorption centered at 526 nm for the Bunte-salt derived AuNPs. TEM analysis confirmed this size difference. The thiol-derived AuNPs had a mean core diameter of 1.8 ± 0.4 nm. In contrast, the particles prepared using the Bunte salt analog showed a mean core diameter of 6.1 ± 1.1 nm (Fig. 2.2). The fact that the Bunte salt gives rise to larger nanoparticles than the thiol is consistent with our hypothesis that the slower passivation kinetics of the Bunte salt ligand precursors could provides access to larger AuNPs.

Given the observed size difference between AuNPs synthesized using Bunte salts and the analogous thiol under the same reaction conditions, we considered a couple of key differences between the two reaction pathways that might lead to the different

outcomes. The first difference is that Bunte salt, when mixed with gold salt, does not form the thiolate-Au(I) polymer that is produced during the thiol-based syntheses. If the Au(III) complex were reduced more slowly than the Au(I) polymer, this might explain the differences in particle size; however, it seems unlikely that the reduction of Au(III) to Au(0) is significantly slower than the reduction of Au(I) to Au(0) by borohydride. A second difference is that monolayer formation occurs at different rates because the transformation of the thiosulfate to the thiolate, that is likely assisted by the surface of the gold nanoparticle and/or borohydride reduction, results in slower, less ordered monolayer formation (passivation) leading, in turn, to the larger particle size.[22] Of the two options, it seems more likely that the larger size of the gold nanoparticles is related to the differences in the rate of monolayer formation on the particle's surface.

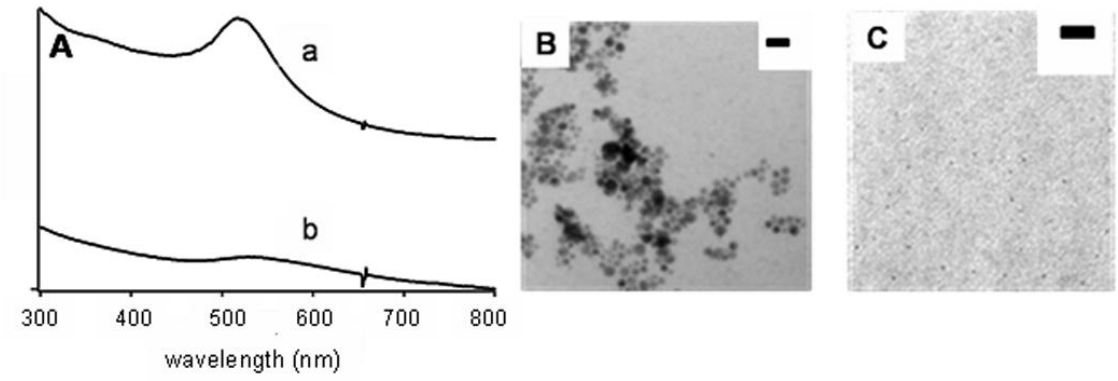

Figure 2.2: (A) Absorption spectra for MEEE-stabilized gold nanoparticles produced using the Bunte salt (a) and the thiol (b). Both particle samples were prepared using a L:Au ratio of 1:6, and the same concentration of reducing agent. (B) TEM micrograph of MEEE-functionalized AuNPs prepared using the Bunte salt (6.1 ± 1.1 nm). (C) TEM micrograph of MEEE-functionalized gold nanoparticles prepared using the thiol (1.8 ± 0.4 nm). Scale bars in B and C are 20 nm.

In addition, this experiment indicated that functionalized AuNPs can be synthesized with minimal core diameter dispersity, even at larger core diameters in this direct synthesis. The 18% polydispersity determined for this sample is comparable to the core diameter dispersity observed in other direct synthesis techniques, such as the Brust synthesis and with previously reported dispersities given for AuNP synthesis using Bunte salts.[7,14,18-21,26,28] In general, direct synthesis with thiols and "masked thiols" (such as Bunte salts) are expected to yield nanoparticle solutions with greater polydispersities than syntheses with more weakly binding ligands such as amines or citrate.[2,29,30] However, it is possible that this polydispersity can be decreased even further if greater control over the synthetic conditions can be realized.

The slower passivation afforded by the Bunte salt precursors makes this a synthetic method with a potentially vast scope, particularly if we can determine which reaction parameters influence the size of the nanoparticles produced. Previous investigations of the Brust synthetic method have revealed that ligand:gold ratio, reaction temperature, and reducing agent concentration have strong influences on particle diameter and dispersity.[7,12,27] We anticipated that these three reaction parameters would have similar impacts on the product nanoparticles properties when Bunte salts were employed, as this means of size control is commonly used in many nanoparticle syntheses, including the Brust and Turkevich syntheses.[1,2,4,7] Murray had previously suggested that the L:Au ratio might be used to tune particle size, in the direct synthesis of AuNPs using Bunte salts as ligand precursors.[18] However, it has not yet been shown the L:Au ratio could be used to tune particle size over a *broad* range of small to large core

diameters for this system. In addition, although the effect of temperature and reducing agent concentration on AuNP core diameters have been tested for other synthetic reactions, the slow passivation kinetics of the ligand precursors employed here may lead to effects in this system that cannot be rationalized by simple analogy to direct synthesis using thiols.

Effect of L:Au Ratio, Temperature, and Reducing Agent Concentration on Particle Size. Based on studies of related AuNP synthetic systems, we expected to observe that the L:Au ratio (L:Au), temperature (T), and reducing agent concentration ([R]) would influence the core diameter of the product AuNPs, but it was not clear what effect these parameters would have on the dispersity of the AuNPs produced using Bunte salt ligand precursors, or whether synergistic effects might exist between the these parameters which could be exploited for size control. In order to investigate this, we screened the three reaction parameters' effects using a factorial experiment design (see Supporting Information).[30] The factorial experiment design (also known as a Design of Experiments, or DOE) entails testing a predetermined matrix of possible combinations of the three reaction parameters (factors) to more rapidly screen the reaction parameters than can be done in a serial fashion. ANOVA statistical analysis can be used to test the impact of each property on the products' core diameter and monodispersity and determine whether any of the reaction parameters showed synergistic effects.[27,30]

The simplest formulation of the DOE in this system calls for screening a matrix of the desired factors at high and low values of a specifically chosen range. The conditions at which the reactions were run are summarized in Table 2.1. In order to successfully

perform the factorial design, the given reaction conditions must be run at precisely chosen values in a randomly generated order, with all of the reaction conditions carefully controlled. Once the raw data has been obtained, the data must be analyzed using ANOVA to assess the significance of each factor.[30]

To perform the factorial design analysis on this synthetic system, we performed a two-level analysis on the three factors. We performed two separate factorial experiment design analyses, which were identical, except that they examined different ranges of L:Au ratios (Table 2.1). Our matrix of sample conditions contained a series of high and low reducing agent concentration (1 and 10 molar equivalents with respect to the gold salt) samples, at different L:Au ratios (1:6-1:1, and 1:4-3:1) and temperatures (2ºC and 60 ºC). In addition, each analysis also included a midpoint- a data point with a set of values halfway between the high and low levels for each factor. The effects on particle diameter and the polydispersity of each sample were determined by TEM analysis of the samples and these data were corroborated qualitatively by UV-vis absorbance analysis of the samples. The raw data collected from the DOE studies are presented in Table 2 (and more fully in the Supporting Information). The data in Table 2.2 has been analyzed with the "low" values of L:Au ratio (1:4) given first, and with the "high" values (3:1) given below.

Table 2.1. The Factors and Levels Associated with the Design of Experiments Analysis

Factors	**Levels**	
	High	Low
Ligand:Au Ratio (L:Au)	1:1, 3:1	1:6, 1:4
Temperature (°C)	60	2
Reductant Molar Equivalents ([R])[a]	10	1

[a] Molar equivalents of reducing agent with respect to the gold salt ($HAuCl_4$)

Table 2.2. Representative Data Generated During the DOE Studies on the Impact of L:Au Ratio, Temperature, and Reducing Agent Equivalents on Core Diameter and Dispersity*

Reaction Conditions			**SPB (λ_{max})[a]**	**d_{core}, nm[b] (% polydispersity)**
L:Au	Reductant Equivalents[c]	T (˚C)		
1:4	1	60	535 nm	30.0 ± 9.5 (32 %)
1:4	1	0	523 nm	2.6 ± 1.1 (42 %)
1:4	10	60	518 nm	3.4 ± 1.1 (32 %)
1:4	10	0	513 nm	3.0 ± 0.9 (30 %)
1:1	1	60	527 nm	3.8 ± 3.1 (82 %)
1:1	1	0	519 nm	3.3 ± 1.1 (33 %)
1:1	10	60	517 nm	3.2 ± 1.1 (34 %)
1:1	10	0	512 nm	2.8 ± 0.7 (25 %)
3:1	1	60	523 nm	2.0 ± 0.5 (25 %)
3:1	10	60	524 nm	2.4 ± 0.7 (29 %)
3:1	10	0	515 nm[d]	1.6 ± 0.4 (25 %)
1.7:1	5.5	24	515 nm[d]	1.6 ± 0.3 (19 %)
1:6	10	60	532 nm	10.1 ± 2.7 (27 %)

* DOE data presented in full in the Supporting Information

[a] The wavelength of the surface plasmon band (SPB) maximum

[b] The mean core diameter for the nanoparticles in the sample followed by the standard deviation. Core diameter measurements were based on a sample of N particles, where N>300, with the exception of the 30 nm particles, where N>100.

[c] The number of moles of sodium borohydride added with respect to hydrogen tetrachloroaurate.

[d] The UV-vis spectra for these samples shows a non-symmetric, shouldered absorption. See supporting information.

As is typical for a factorial design, inspection of the raw data reveals little about the effect of the three factors on particle size and dispersity. In fact, it is tempting to conclude that the majority of the core diameters lie within experimental error of one another, and no trends can be identified. In order to understand which factors had a significant impact on particle size and dispersity, ANOVA analysis of the data given in Table 2.2 was undertaken.[30a-c] The ANOVA assesses the variation of the means and generates main effects plots. This analysis determines the significance each factor by comparing the values for core diameter and dispersity obtained at high and low values for each factor (an example main effects plot is included in the Supporting Information). From the main effects plot, the significance of each parameter on the response can be calculated, and these results are tabulated as Pareto Effects Plots (Figure 2.3). For a two-level, three-factor analysis, any factor that shows an effects value greater than 2.31 is significant at the 0.95 confidence level. In Figure 2.3a, the analysis of the impact of the factors on core diameter, all of the factors show effects values greater than 2.31, indicating that all three factors (and combinations of factors) may have a significant impact on particle core diameter. In Figure 2.3b, L:Au ratio displays an effects value of less than 2.31, indicating that L:Au ratio has no effect on particle diameter dispersity, but the amount of reducing agent used and the reaction temperature do have significant effects.

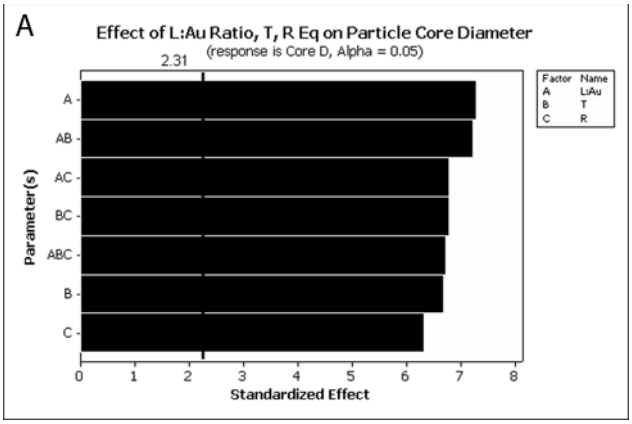

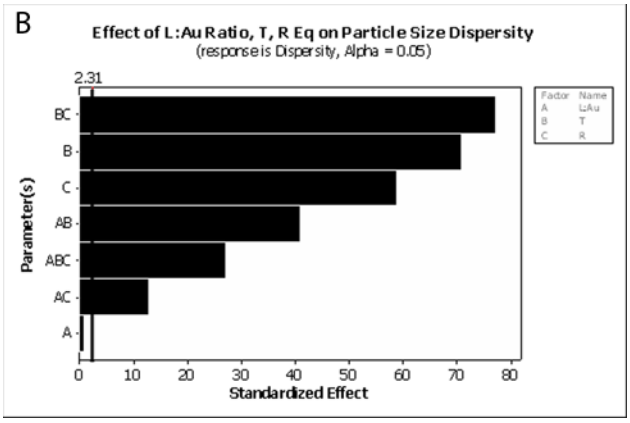

Figure 2.3: Results of the ANOVA analysis for the factorial experiment performed for the Bunte salt synthesis. Factors (L:Au ratio, T, and [R]) were tested at the 0.95 confidence level. Parameters with an effects value greater than 2.31 have a significant impact on the response variable. The analysis indicates that all three factors affect the core diameter of the particles (A), but L:Au ratio has no effect on the dispersity in particle diameter (B). Factor A is L:Au Ratio, Factor B is Temperature, and Factor C is Reducing Agent Equivalents.

Based on the statistical analysis, we conclude that the L:Au ratio can be used to tune particle size over a wide range. At low L:Au ratios, larger particles are more likely to form. Table 2.2 shows that particles with mean diameters of 30.0 nm and 10.1 nm were readily formed at L:Au ratios of 1:4 or less, while at higher L:Au ratios (1:1 or greater), no particles with d_{core} > 3.8 nm were formed. Thus, the L:Au ratio can be used to tune

particle diameters, which is a common means of size control in all nanoparticle syntheses.[1,2,4,7,12] However, the use of Bunte salts as ligand precursors is potentially notable because the range of particle sizes that can be synthesized is quite broad, easily exceeding the range of sizes available via direct synthesis using thiols.[1,2,4,7,12,29] In fact, the range of sizes that can be realized is more comparable to the size ranges available when using weakly stabilizing ligands such as citrate or amines,[2,31] which would be consistent with the hypothesis that the Bunte salts initially act as weak stabilizing agents (allowing access to larger cores), but then eventually are converted to thiols, providing monolayer-protected clusters.

The temperature and reducing agent concentration also strongly influence the core diameter of the product. The data in Table 2.2 show that as temperature decreases, smaller core diameter particles are produced at all L:Au ratios, and statistical analysis confirms that temperature is a significant determinant of core diameter. This decrease in particle diameter is likely caused by the developing ligand shell adsorbing to the particle's surface more strongly at lower temperatures, decreasing the rate of growth and thereby producing smaller particles.[7,14,27] Similarly, higher borohydride concentrations favor the formation of smaller particles, presumably because the higher reducing agent concentration produces a larger number of small nuclei upon addition, limiting the amount of gold precursor available for growth of the particles.[7,12,27] In addition, statistical analysis of the data revealed that the three parameters tested interact synergistically to control core diameter, a not especially surprising, but potentially powerful, observation (Supporting Information). Temperature and reducing agent concentration (by themselves

or in conjunction with the L:Au ratio) provide an additional means of controlling particle size, and can potentially be manipulated to further tune core diameter, when size increases or decreases can no longer be realized by changing the L:Au ratio alone.

The reducing agent concentration also has a significant impact on the polydispersity of the product, in addition to its effect on particle size. Many of the samples tested in the screening experiments at low reducing agent concentration show greater than 32% polydispersity, but at high reducing agent concentrations, the majority of samples show polydispersities of less than 27% (Table 2.2). Statistical analysis of the data found these differences to be significant (Supporting Information). This is typical of many gold nanoparticle syntheses, in which higher reducing agent concentrations produce a more uniform nucleation event, leading to more monodisperse products.[2,4,7,12,27] We found that samples of comparable size and polydispersity could be synthesized at both 5.5 molar equivalents of borohydride and 10 equivalents of borohydride, indicating that further improvements in monodispersity probably cannot be realized simply by further increasing the borohydride concentration. Analogous to what has been observed for the Brust preparation, temperature alone also has a strong influence on particle core diameter dispersity, although seemingly comparably polydisperse samples were observed at both high and low temperature runs for a variety of L:Au ratios and reductant concentrations.[27] Statistical analysis of the data, however, indicates that temperature does have a substantive influence on dispersity, particularly in conjunction with reducing agent concentration.

It should also be noted that at low borohydride concentrations and high temperatures, particularly large gold nanoparticles can also be formed in this synthesis. At the lowest borohydride concentration tested, and at elevated temperatures, 30 nm AuNPs were observed that possessed reasonable core diameter dispersity (~33%, see Table 2.2). This suggests that the borohydride concentration can potentially be used as a means of size control in conjunction with the L:Au ratio. This increases the versatility of the synthesis, and can provide greater flexibility if particularly large particles are desired.

By evaluating the data collected in this study, some general guidelines can be drawn for the synthesis: 1. Core diameter is most affected by the L:Au ratio (given non-limiting concentrations of borohydride), 2. Temperature can be used to tune core diameter with fine control in conjunction with the L:Au ratio, and 3. The reducing agent concentration has the greatest impact on particle polydispersity. Our design of experiments study indicated that a number of these parameters could also be employed synergistically to directly produce monolayer-protected AuNPs with core diameters that traditionally have had to be accessed using multi-step synthetic methods incorporating ligand exchange methods. Bearing the general effects of these parameters in mind, a versatile synthesis was developed in which borohydride concentrations are kept high (~10 molar equivalents with respect to gold) to minimize polydispersity, and size control is primarily provided by L:Au ratio and temperature.

Core Diameter Size Control for Bunte Salt-Based AuNP Synthesis. Applying the guidelines discussed above, we examined the accessible range of core diameters available when using the optimized synthetic conditions (see Experimental). Based on our

investigation of the reaction parameters, we anticipated that small particles would be produced at a combination of high L:Au ratios and low temperatures. Accordingly, we combined the MEEE BS (**1**) and the gold precursor in a ratio of 3:1 and allowed this solution to equilibrate at 2º C. Following borohydride addition, the solution became a rich brown, with a UV-vis spectrum revealing an absorbance at 515 nm, and several smaller absorbance bands at 400 nm and 310 nm (Fig. 2.4). TEM analysis reveals that these particles have a core diameter of 1.6 ± 0.4 nm. By increasing the temperature and decreasing the L:Au ratio (24 ºC, L:Au 1:1), the same synthesis yielded 3.1 ± 1.1 nm particles. The UV-vis and TEM data for the products of this study are displayed in Table 3 and Fig. 4. When the L:Au ratio is decreased to 1:6 a core diameter of 6.1 ± 1.1 nm is achieved, and a further decrease in the L:Au ratio increases the diameter to 10.7 ± 3.1 nm (Table 2.3).

Table 2.3. Determining the Range of Available Core Sizes By Varying L:Au Ratio and Temperature Using the MEEE BS (**1**)

Reaction Conditions			**SPB (λ_{max})**	**d_{core} (nm)**
MEEE BS:Au	T (° C)	Reductant Equivalents[a]		
1:100	60	10	535 nm	21.4 ± --
1:20	60	10	527 nm	10.1 ± 3.6
1:6	24	10	526 nm	6.1 ± 1.1
1:1	24	10	515 nm	3.1 ± 1.1
3:1	2	10	--	1.6 ± 0.4

[a] Molar equivalents of sodium borohydride added with respect to $HAuCl_4$

-- greater than 50% polydispersity

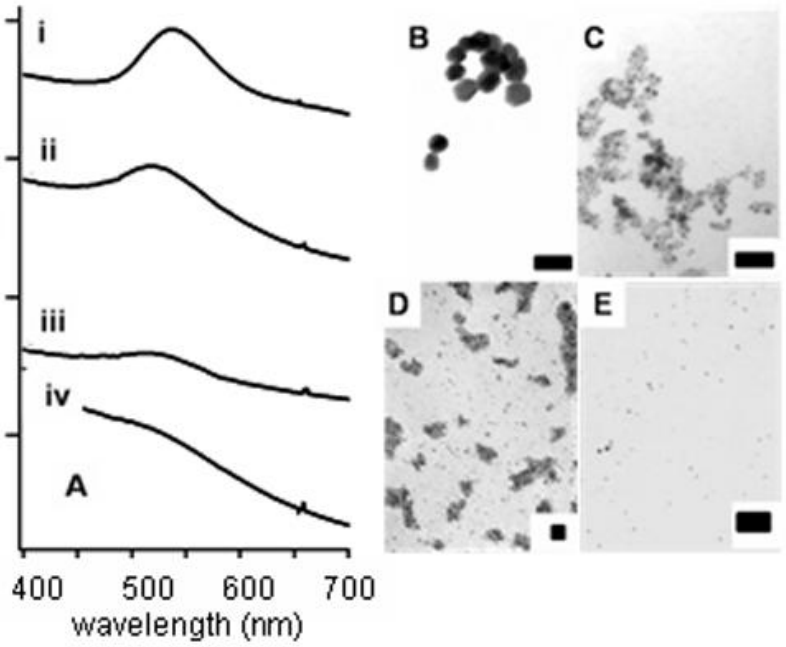

Figure 2.4: Absorbance data and TEM micrographs for various core diameters of MEEE-functionalized AuNPs synthesized using a Bunte salt ligand precursor. By varying the L:Au ratio, temperature, and reducing agent concentration a variety of core diameters between 20.0-1.5 nm can be accessed by this method. Absorbance data (A) and TEM micrographs (B-E) are shown for 21.4 nm particles (i, B), 6.1 nm particles (ii, C), 3.1 nm particles (iii, D), and 1.6 nm particles (iv, E). The maximum accessible core diameter for this method is greater than 20 nm. Scale bars in (B) and (C) are 50 nm. Scale bars in (D) and (E) are 20 nm.

In order to determine the maximum accessible core diameter for this synthesis, we heated the gold precursor in solution to 60 ºC with a limiting amount of ligand (1:100 L:Au). Addition of 10 molar equivalents of borohydride to the solution induces an eventual color change to a rich red-violet. The solution displays a very strong plasmon absorbance centered around 535 nm, suggesting the formation of gold nanoparticles greater than 10.0 nm in diameter. TEM analysis of the solution indicates that the product consists of highly polydisperse gold nanoparticles with a mean diameter of 21.4 nm. This provides final evidence that the Bunte salt-based gold nanoparticle synthesis indeed provides access to core diameters larger than those available in the Brust preparation, but it is also a highly flexible approach, and can be used to synthesize a wide variety of particle core diameters.[7,12,27]

Synthesis of Large Hydrophilic Functionalized AuNPs. In order to examine whether Bunte salt ligand precursors could be used to easily introduce hydrophilic functionalities onto the surface of large gold nanoparticles in a direct synthesis, we attempted to prepare large particles possessing positively charged, negatively charged and neutral hydrophilic functionalities. To do this, the previously prepared ligand precursors (**1**, **2**, and **3**) were reacted with a set amount of $HAuCl_4$ and 10 molar equivalents of sodium borohydride at room temperature. Upon sodium borohydride addition, the reaction mixtures quickly turned from orange or brown to a deep red-violet, indicating the formation of large AuNPs. After three hours of reaction time, a small aliquot of each solution was analyzed by UV-vis and TEM (Table 2.4) to determine the sizes of the nanoparticles produced. We found that for each ligand precursor, the vast majority of particles produced in every sample were larger than 5 nm in diameter, again indicating that Bunte salts can be used to access large core diameter AuNPs even when different ω-functionalities are employed. AuNPs synthesized with a MPTMA BS:Au ratio of 1:2 show a core diameter of 7.8 ± 2.1 nm, while those samples synthesized with 1:6 ratios of the MEEE and MNA Bunte salts show mean core diameters of 6.1 ± 1.1 and 8.4 ± 2.8 nm, respectively (Table 2.4). These measurements are reflected in the UV-vis absorbance data, which shows strong plasmon absorbances for all three samples (Table 3). The ability to access 6-8 nm functionalized AuNPs for a variety of ω-functionalized Bunte salts indicates that the general efficacy of the synthesis is not compromised by the tail group of the ligand precursor.

Table 2.4. Size Analysis, Percent Composition, and Functional Group Content Data for Functionalized Gold Nanoparticles Synthesized with the Chosen Ligand Precursors

L:Au	SPB (λ_{max})	d_{core} (nm)[a]	%Organic (TGA)[b]	S:Au (XPS)[c]
1:2 MPTMA BS:Au	525 nm	7.8 ± 2.1	6.3 %	0.059
1:6 MEEE BS:Au	526 nm	6.1 ± 1.1	3.1 %	0.065
1:6 MNA BS:Au	515 nm	8.4 ± 2.8	3.5 %	--

[a] Core diameter determined by TEM analysis. Mean Diameter and standard deviation determined from n>300 nanoparticle samples. For TEM micrographs, see Supporting Information.

[b] TGA performed on 2.0 mg samples of lyophilized particles that had previously been purified to remove free ligand and small gold salts by diafiltration.

[c] XPS data obtained on a purified sample dropcast on a clean microscope slide. No sample data taken for the MNA-Functionalized AuNPs (--). Ratio given is for the thiolate S2p peak versus the Au 4f peak.

Representative TEM micrographs of all the synthesized particles are shown in Fig. 2.5. It is clear from the size distribution histograms that the majority of the particles in every sample range from 6.0-14.0 nm in diameter, clearly larger than the 6 nm maximum diameter provided by the Brust method.[7,10,12,27] The polydispersity of these reaction products (as synthesized) varied from 18-28% (Table 2.3). This level of polydispersity is comparable to that reported for other direct synthesis methods such as the Brust preparation, but greater than the polydispersity associated with the Turkevich synthesis for citrate-stabilized particles of the same size or recent syntheses of amine-stabilized AuNPs.[4,7,12,27] No Bunte salt-based particle synthesis has yet

reported lower monodispersity than 18%.[18-21] It is important to note that the size distributions reported here are for the reaction mixture as synthesized, and have not been subjected to any size-based purification. There are a number of rapid, size-selective aqueous purification methods that could used to minimize the polydispersity of the reaction product. In particular, the addition of diafiltration to this synthesis may be beneficial as this method has been shown to be effective in separating large and small gold nanoparticles in aqueous samples.[24]

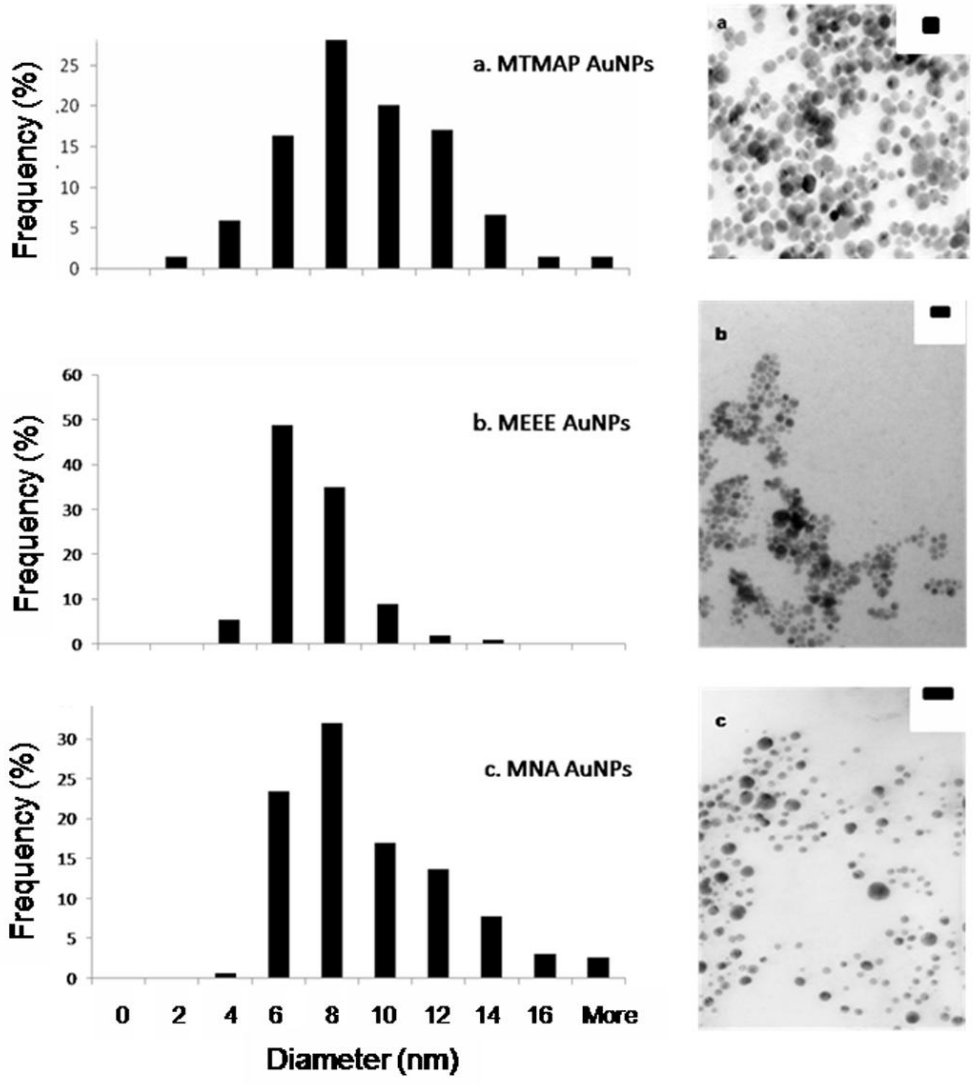

Figure 2.5: Representative micrographs for (a) MPTMA (7.8 ± 2.1 nm), (b) MEEE (6.1 ± 1.1 nm), (c) MNA-functionalized (8.4 ± 2.8 nm) gold nanoparticles. Scale bars are 20 nm.

An unusual feature of these data is that while similar L:Au ratios (1:6) of the MEEE and MNA Bunte salts produced gold nanoparticles of comparable sizes, in the case of the quaternary ammonium ligand, a higher L:Au ratio (1:2 L:Au) could be employed, and large particles could still be produced. Functional group compositional

analysis (FTIR, XPS) have shown that no matter the terminal functionality the Bunte salt carries, the ligand binds through a thiolate linkage to the gold core, suggesting that the observed differences do not result from any difference in the ligand-gold interaction (see Supporting Information). Instead, it is more likely that the bulky ω-functionality carried by this ligand precursor (**3**) makes the monolayer formation on the particle surface a slower process favoring the formation of larger particles. Effects of this kind have been observed in the direct synthesis of gold nanoparticles using thiols, but the origin of these effects is not well understood.[12]

In order to verify the chemical content of the ligand shell, the purified nanoparticles were analyzed by FTIR, TGA, and XPS. XPS analysis revealed a doublet in the S2p region of the spectrum with peaks centered at 162.0 and 164.5 eV (Fig S3, Supporting Information), consistent with the formation of a thiolate linkage between the ligand and the gold core. The S:Au ratio is 0.064 in the XPS spectrum for the MEEE-functionalized AuNPs. From the NP surface area determined based upon from the 10.0 nm average diameter of the Au spheres determined by TEM, and a thiolate ligand has a footprint of 21.4 $Å^2$, the S:Au ratio should be 0.085.[7c] Therefore, the S:Au ratio is in reasonable agreement with the ratio expected for a fully formed monolayer on the surface of the nanoparticle. The slightly lower coverage observed can be rationalized by recalling that Bunte salts tend to form slightly less ordered thiolate monolayers on gold surfaces than thiols, due to the steric demands of the thiosulfate group.[23] TGA data collected for these samples suggest that the nanoparticles are 3.5-6.0% organic by weight, again indicating a well-formed monolayer protecting the particles (Table 2.4). The S2p doublet

at lower binding energy in the XPS spectrum was observed for both the MTMAP- and MEEE- functionalized AuNPs indicate that the Bunte salt ligand precursors form a thiolate linkage to the gold core, regardless of their terminal functionality (Supporting Information). In addition to the peak from the thiolate-gold linkage observed in the XPS, the spectrum also shows a peak at 169.0 eV, consistent with the presence of oxidized sulfur in the ligand shell. Purification of the nanoparticle solution by diafiltration significantly decreases the content of oxidized sulfur in the XPS spectrum, suggesting that the majority of the oxidized sulfur is labile, and comes from excess free ligand and cleaved sulfite remaining in the monolayer. When the oxidized sulfur peaks are included in the S:Au ratio, the ratio increases to 0.15. The presence of even small amounts of thiosulfate groups is expected to increase the ratio because each ligand possesses two sulfur atoms. Although some of the oxidized sulfur is probably present at the particle surface, the rest is likely intercalated into the ligand shell far from the particle surface. The results of the XPS study are consistent with models of Bunte salt-derived monolayers prepared on 2-D gold surfaces.[22] That data indicates that the Bunte salt-derived particles are protected by a monolayer that is fairly close-packed, but retains much of the oxidized sulfur eliminated from the ligand precursor. This phenomenon has previously been observed in monolayers prepared from Bunte salt precursors in aqueous solution on 2-D gold substrates.[23]

FTIR analysis of the functionalized AuNPs verifies that the desired ω-functionalities are displayed by the particles following synthesis. IR analysis of the MPTMA-stabilized AuNPs shows stretches consistent with sp^3 C-H stretching (2890 cm^-

^{1}) and C-N stretches (1080 cm^{-1}), while MEEE and MNA-functionalized AuNPs show O-H stretches consistent with alcohols (3410 cm^{-1}) and carboxylic acids (3078 cm^{-1}) respectively (Supporting Information). MNA-functionalized AuNPs also show a carbonyl stretch consistent with carboxylic acids (1715 cm^{-1}), as well as a carboxylate stretch consistent with the deprotonated acid (1585 cm^{-1}). In addition to the IR data, the nanoparticles' solubilities are consistent with their proposed functionalities: MPTMA-functionalized particles show good solubility in both polar protic and non-polar solvents, MEEE-functionalized particles show a propensity to closely associate on TEM grids (presumably due to strong hydrogen bonding between the ligand shells), and MNA-functionalized nanoparticles display reduced stability in acidic solutions, consistent with the loss of electrostatic repulsion in the ligand shell at low pH.

Conclusions

In conclusion, we have taken advantage of the slow passivation kinetics of functionalized Bunte salts to develop a new and versatile synthesis for the production of hydrophilic functionalized AuNPs with tunable core diameters between 1.5 and 20 nm in diameter. Bunte salts provide access to monolayer-protected particles with core diameters that are larger than those available using the corresponding thiol. The range of nanoparticle sizes afforded by this method is much greater than that provided by direct synthesis using thiols, but size control can still be accomplished using familiar methods. Lower temperatures and higher L:Au ratios favor the formation of smaller particles, while higher temperatures and lower ligand precursor:gold ratios favor the formation of larger particles up to 20 nm in diameter. The use of Bunte salt ligand precursors also

provides an excellent synthetic platform for attaching a wide variety of hydrophilic functional groups to the surface of gold nanoparticles, however, early data suggests that the terminal functionality carried by the Bunte salt may affect the sizes of gold nanoparticles that can be produced. This method has the potential to become a powerful tool, as it provides a common synthetic route to functionalized nanoparticles with both large (d_{core} > 5 nm) and small core diameters. This may have far reaching consequences for the development of functionalized AuNP-based sensors and studies of the biochemical fate and transport of AuNPs.

CHAPTER III

TWO-STAGE LIGAND SHELL FORMATION AT GOLD NANOPARTICLE SURFACES: CONVERSION OF BOUND ALKYL THIOSULFATES TO THIOLATES

Note: The work reported in this Chapter is primarily that of the author, and this manuscript has been submitted to the ACS journal *Inorganic Chemistry*. The work in this Chapter is co-authored. Carmen Lisowski headed the characterization of the 'unstable' and 'stable' MEEE-AuNPs described in this work. Jim Hutchison provided editorial guidance and advice.

Introduction

Among the synthetic methods that produce ligand-stabilized gold nanoparticles,[1-4] the use of ligand precursors has received little attention, despite the synthetic utility of these molecules.[4-12] In this context, a ligand precursor is a molecule that undergoes a significant change in binding mode during its transformation from a precursor to a ligand during a nanoparticle formation reaction. The change in binding mode can provide significant synthetic advantages in gold nanoparticle (AuNP) synthesis. For example,

weak passivation by the precursor might allow growth of larger core diameter particles before the AuNP is more strongly passivated by the ligand.[5,9,12]

Bunte salts (alkyl thiosulfates) are a class of ligand precursors that are transformed to thiolate ligands during the synthesis of gold nanoparticles.[4-8,12] The use Bunte salts in AuNP synthesis has been explored, in part, because they are convenient reagents. They are more resistant to oxidation during storage than thiols, and eliminate the need for phase-transfer reagents in biphasic AuNP syntheses in many cases.[4-8] Recently, we have shown these ligand precursors also permit direct synthetic access to thiol-protected AuNPs with core diameters greater than 5.0 nm. [5] These AuNPs are important synthetic targets for a variety of device assembly, sensing, and bio-imaging applications. [13-28] We hypothesized that larger sizes were attainable using this approach because the Bunte salt provides weak passivation during synthesis, permitting larger core growth before it is transformed to a covalently-bound thiol. However, the details of this synthetically useful transformation are almost entirely unknown.

What is known about the transformation of thiosulfates to thiolates at AuNP surfaces has been derived primarily from studies of thiolate monolayer formation on planar gold films and from analysis of AuNP products produced using the method.[4-8,29-32] The formation of thiolate monolayers on gold films has been shown to proceed *via* the adsorption of thiosulfates to the gold surface, followed by the spontaneous formation of thiolate-Au bonds and the elimination of oxidized sulfur (Figure 3.1A).[29-32] When the use of Bunte salts in nanoparticle synthesis was first investigated, it was proposed that the thiolate ligand shell would form by a similar spontaneous reaction, with the surface of the

gold nanoparticle catalyzing the transformation of the Bunte salt to the thiol (Figure 3.1B).[4] However, a distinct two-stage passivation mechanism for ligand shell formation is supported by the successful synthesis of large core diameter thiol-protected AuNPs, in that there must be a period where growth of the particle is only weakly passivated to allow for the increase in core size.[5] However, the mechanism by which ligand shell formation occurs has received no detailed study. It has previously been proposed that ligand shell formation from ligand precursors of this kind may be a more complex chemical reaction than is observed in monolayer formation on gold films.[5,8] Specifically, it has been speculated that the reducing agent may play a role in the transformation of the Bunte salt to the thiolate, and the role of the AuNP surface in mediating ligand shell formation is unclear.[8]

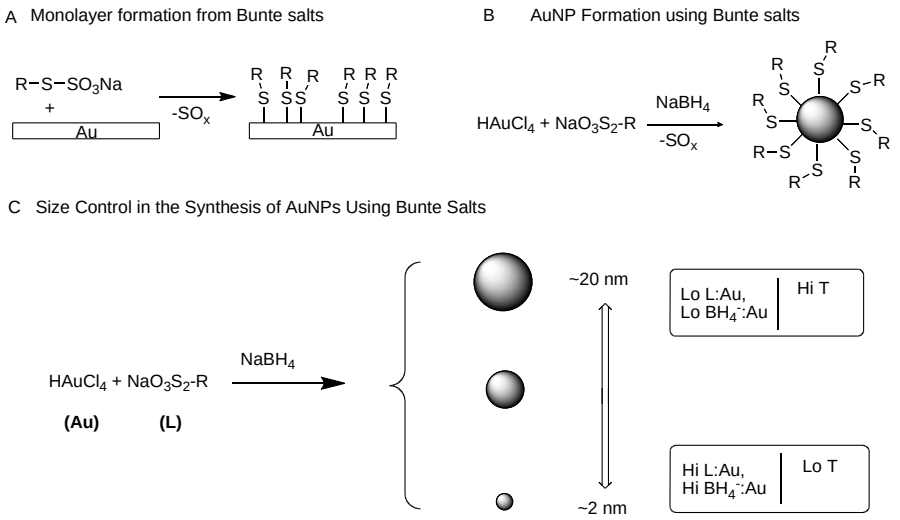

Figure 3.1: Schematic of the general reactions describing the formation of thiolate-protected AuNPs and thiol monolayers using Bunte salt ligand precursors. (A) The formation of thiol manolayers on gold films proceeds by spontaneous reduction of the Bunte salt to the thiolate monolayer. (B)The general AuNP synthesis involves reduction of gold tetrachloroaurate in the presence of the Bunte salt by sodium borohydride to give a thiol-protected gold nanoparticle. (C) The size of the particles produced depends on the L:Au ratio, the ratio of borohydride:gold used, and the temperature at which the reaction is run. Thus, a single general synthetic technique can be used to produce many functionalized AuNPs of various sizes.

We recently observed that gold nanoparticles with core diameters greater than 5.0 nm synthesized using Bunte salts as ligand precursors displayed different chemical behaviors depending on the synthetic reaction conditions. During synthesis, the size of the particles produced may be controlled by varying either the L:Au ratio, the temperature of the reaction, or the amount of reducing agent used (Figure 3.1C), which means there are multiple synthetic routes to produce AuNPs of the same size.[5] We

observed that the reaction conditions also impacted the stability of the AuNPs. Some batches of these AuNPs aggregated irreversibly when exposed to high-*Z* cations,[α] or during concentration and purification. This type of instability is not consistent with thiol-protected AuNPs, but rather with AuNPs that are protected by adsorbed ions. [32-39] This implied that the synthetic reaction conditions not only influenced the size of the AuNP produced, but also its ligand shell composition.[32-35] This observation opened up an opportunity to more closely scrutinize the transformation of Bunte salts to thiolate at AuNP surfaces during synthesis.

The observation that some Bunte salt-derived gold nanoparticles behave like electrostatically passivated, rather than thiol-protected nanoparticles, led us to hypothesize that these particles were protected by an adsorbed layer of Bunte salts. The observation that AuNPs protected only by adsorbed ligand precursors could be produced under certain reaction conditions opened up new questions about the nature of the Bunte salt-thiolate transformation. Could we confirm the identity of these electrostatically-passivated AuNPs? Does the reducing agent used in the synthesis play a role in the formation of the thiolate ligand shell? Can the observations we made here be generalized to all AuNPs produced in this synthesis, or does the size of the AuNP influence the ligand shell formation as well?

Herein, we report the investigation of the transformation of Bunte salt precursors to thiolate ligands on gold surfaces during nanoparticle formation and show that these transformations are more complex than the analogous monolayer formation observed on gold films. On nanoparticle surfaces, the transformation proceeds through a Bunte salt-

protected gold nanoparticle intermediate that can be isolated from the reaction mixture. The extent of thiolate ligand shell formation depends on the synthetic conditions, particularly the sodium borohydride:gold ratio. Ligand shell formation is also influenced by nanoparticle size. This study provides the initial details of the transformation of thiol precursors to thiolates on nanoscale gold surfaces, and has direct practical consequences for the synthesis of AuNP using Bunte salts as ligand precursors.

Experimental

Materials. Hydrogen tetrachloroaurate trihydrate ($HAuCl_4 \bullet 3H_2O$) was obtained from Alfa Aesar. All other reagents including 2 -[2-(2-chloroethoxy)ethoxy]ethanol, sodium thiosulfate, and sodium borohydride were obtained from Aldrich and used without further purification. Water soluble lanthanide salts (e.g.- $Eu(NO_3)_3$ and $Gd(NO_3)_3$) were obtained from Aldrich. The synthesis of the two Bunte salt ligand precursors MEEE BS and MHTMMA BS has been described in our previous work.[5,9] Deionized nanopure water (18.2 MΩ-cm) was purified with a Barnstead Nanopure Diamond system, and was used for the preparation of stock solutions and as a solvent for nanoparticle synthesis.

Analytical Procedures. Nanoparticles were characterized using a combination of transmission electron microscopy (TEM), UV-visible absorption spectroscopy, and X-ray photoelectron spectroscopy (XPS). TEM analysis was performed on a FEI Titan FEG-TEM. Gold nanoparticle samples were prepared for analysis by floating etched silicon dioxide TEM grids[40] on top of a drop of AuNP solution for 1 minute followed by

copious rinsing with Nanopure water. A minimum of 600 nanoparticles per sample were used for size analysis. The TEM micrographs were then processed using Image J software to determine average core diameter, size distribution and standard deviation following the previously reported method.[41] UV-vis Absorption Spectroscopy analysis of the AuNPs was performed on a Mikropack DH-2000 UV-vis-NIR light source equipped with an Ocean Optics USB2000 spectrophotometer. X-ray Photoelectron Spectroscopy (XPS) analysis was performed on a ThermoScientific ESCALAB 250 XPS. NP samples prepared for XPS analysis were first diafiltered with 20.0 volume equivalents of water to concentrate the NP solution and remove free ligand.[42] In the case of the 'unstable' AuNP samples, this was reduced to 5.0 volume equivalents to reduce the likelihood of aggregation during purification. To deposit the AuNP samples for XPS analysis, a 20-uL droplet of concentrated aqueous AuNP solution was placed on the surface of a 1x1 mm segment of silicon wafer that was covered by an approximately 500 Å layer of evaporated chromium. The casting process was repeated 5 times, or until the deposited NPs formed a non-transparent sample layer on the wafer surface. XPS analysis was initiated within half an hour of deposition. The binding energies of all peaks were referenced to the Au 4f peak at 84.0 eV.

Synthesis of Functionalized Gold Nanoparticles. Nanoparticle syntheses were performed using our previously reported methods.[5,12] Briefly, an aqua regia-cleaned 250-mL round-bottom flask equipped with a stir bar was charged with 100 mL of H_2O, 500 μL of $HAuCl_4 \bullet 3H_2O$ solution (0.1 M), and 100 μL of an aqueous MEEE BS solution (0.1 M). The ligand precursor:gold (L:Au) ratio, the temperature at which the reaction was run

(T), and the amount of reducing agent used with respect to gold (BH_4^-:Au) was varied to provide particles samples of different sizes, formed under widely different reaction conditions.[5,12] The reaction mixtures were allowed to stir for 10 minutes, and then between 1.5 and 10.0 mL of a freshly prepared aqueous 0.1 M $NaBH_4$ solution was added rapidly to the reaction mixture (1.5-10.0 molar equivalents of borohydride with respect to gold). The total volume of this addition was held constant, so that the total volume of addition at this stage was 10.0 mL, diluting the borohydride stock as necessary. The borohydride addition induces a color change to deep red or brown (depending on particle size) in the flask. The reaction mixture was allowed to stir for 3 hours. These AuNP products were then analyzed by TEM, UV-vis, and XPS to determine their mean diameter and the extent of monolayer formation on the particle surface. The resulting nanoparticles are filtered through a coarse-fritted glass funnel, and the filtrate was collected and purified *via* diafiltration with twenty volume equivalents of Nanopure water through a 70 K membrane (Pall Corporation).[42]

Assays to Determine AuNP Stability. In order to determine whether AuNP samples were 'stable' or 'unstable' in solution, three assays were employed. First, the successful formation of a 'stable' AuNP was assayed by titration with an aqueous solution of either 0.1 M $Gd(NO_3)_3$ or $Eu(NO_3)_3$. These cations were chosen, as we had previously prepared malonamide-functionalized AuNPs for use as colorimetric lanthanide detectors.[12] The MEEE-functionalized AuNPs should show no colorimetric response to lanthanide addition. If the color of the solution changed after cation addition from red or brown to a pale blue, this was considered evidence of AuNP instability. In addition, 1.5 mL of the

particle solution was centrifuged at 14 000 rpm for 6.0 min to check for irreversible aggregation during centrifugation. If the particles fell out of solution during this process, and could not be re-suspended, this indicated that the AuNPs were 'unstable' in solution-having undergone irreversible aggregation during centrifugation. Finally, during purification using diafiltration, if the AuNP solution changes color to a pale blue after between 10.0 and 20.0 volume equivalents of water have passed through the membrane, this indicated that the AuNPs were unstable and had aggregated irreversibly.

Reaction of MEEE Bunte Salt with Borohydride. In order to determine whether borohydride reduces Bunte salts to thiols, 20 μL of 0.1 M MEEE BS was combined with 0.5 mL of 0.1 M sodium borohydride in 10.0 mL of D_2O. This solution was allowed to stir for three hours. After this time, a small aliquot of this solution was removed and analyzed by ^{1}H-NMR spectroscopy to determine whether the borohydride had reduced the Bunte salt.

Conversion of 'Unstable' AuNPs to Thiolate-Protected AuNPs. In order to test whether the addition of sodium borohydride could convert 'unstable' AuNPs to 'stable' AuNPs, nanoparticle samples were synthesized using the standard synthesis method described above, but with conditions specifically chosen to produce unstable AuNPs (1:6 L:Au, 2.0:1 BH_4^-:Au, 24 °C). Following minimal purification (10.0 volume equivalents diafiltration), for solutions that failed the stability assays, the dark red-purple AuNP solution was divided into thirds, and fractions placed in separate 100-mL round bottom flasks. The effect of additional sodium borohydride addition tested, as was additional ligand precursor plus sodium borohydride, and the experiment was controlled for

dilution. To the first fraction, 5.0 mL of Nanopure water was added. This slowly turned a pale blue color over several hours of stirring. 3.0 mL of aqueous $NaBH_4$ (0.1 M) and 2.0 mL of Nanopure water were added to the second flask. This solution remained a vibrant red color indefinitely during stirring. Identical results were obtained for the fraction which received both ligand precursor and borohydride, suggesting that only borohydride addition was necessary to effect this conversion. All solutions were tested for in solution stability, and it was found that the solution which had received additional borohydride input was stable against cation addition, centrifugation, and purification by diafiltration. Samples of both solutions were retained for UV-vis and TEM analysis. The stable and unstable AuNP solutions were concentrated and prepared for XPS analysis.

Results and Discussion

Our observation that AuNPs synthesized using thiosulfate ligand precursors under certain reaction conditions possess different stabilities indicated that reaction parameters might influence the formation of the ligand shell from Bunte salts. In order to better understand the process of Bunte salt to thiolate transformation at the nanoparticle surface, we sought to first classify the behavior of the 'stable' and 'unstable' Bunte salt-derived AuNPs. We then analyzed the surface chemistry of the two classes of particles in an attempt to correlate the particle's stability and ligand shell composition to the reaction conditions that led to particle formation. We explored the role of borohydride in ligand shell formation by examining the ligand shell composition of 7.0 nm AuNPs synthesized at different borohydride:gold ratios. Finally, we determined how the reduction of the Bunte salt to the thiolate is accomplished at the AuNP surface and studied whether the

details of this transformation were common to AuNPs of all sizes, in order to construct a basic reaction pathway for the formation of the ligand shell.

Instability in Gold Nanoparticle in Response to Cation Addition. In order to understand the phenomenon of AuNP instability that we previously observed, we prepared MEEE- functionalized gold nanoparticles with core diameters of 6.0 nm by performing our standard AuNP synthesis at a L:Au ratio of 1:6 and a BH_4^-:Au ratio of 2.5:1 at 24°C.[9] We found that some of the AuNP batches prepared under these conditions contained 6.0 nm nanoparticles that aggregate irreversibly during purification by diafiltration,[42] or concentration by centrifugation, whereas other 6.0 nm AuNPs (prepared under the same conditions) survived purification with no complications. In addition, those AuNP batches that aggregated were sensitive to the addition of highly charged cations. We isolated aliquots of AuNP solutions of both the 'stable' and 'unstable' AuNPs prepared by this method. We found that both samples possessed similar size distributions by TEM. The 'stable' AuNPs possessed a mean core diameter of 5.3 ± 1.1 nm. The 'unstable' sample possessed a mean core diameter of 6.1± 1.1 nm.

We used the addition of metal cations as an assay to quickly probe the stability of MEEE-AuNP samples, because this is more rapid and controlled than the diafiltration or centrifugation. The particle instability was manifested by irreversible AuNP agglomeration, which was readily apparent in the UV-vis absorbance spectrum of the sample (Figure 3.2). The addition of a 100 μL aliquot of 0.1 M Gd^{3+} to 3.0 mL of the unstable 6.0 nm MEEE AuNPs (Figure 3.2 A, dashed traces) caused a bathochromic shift

and significant broadening in the absorbance spectra (Figure 3.2 A, solid trace). In addition, the absorbance spectra show a distinct rise above the baseline that was consistent with light scattering by agglomerated nanoparticles.[1,43] The 'stable' samples of 6.0 nm MEEE AuNPs also showed no spectral response to an equal addition of Gd^{3+} (Figure 3.2 A, dashed traces), and TEM analysis of this NP sample revealed that the NPs discrete (Figure 3.2, B). Conversely, in the case of the 'unstable' AuNP samples, large agglomerated masses of NPs were seen across the grid surface (Figure 3.2, C).

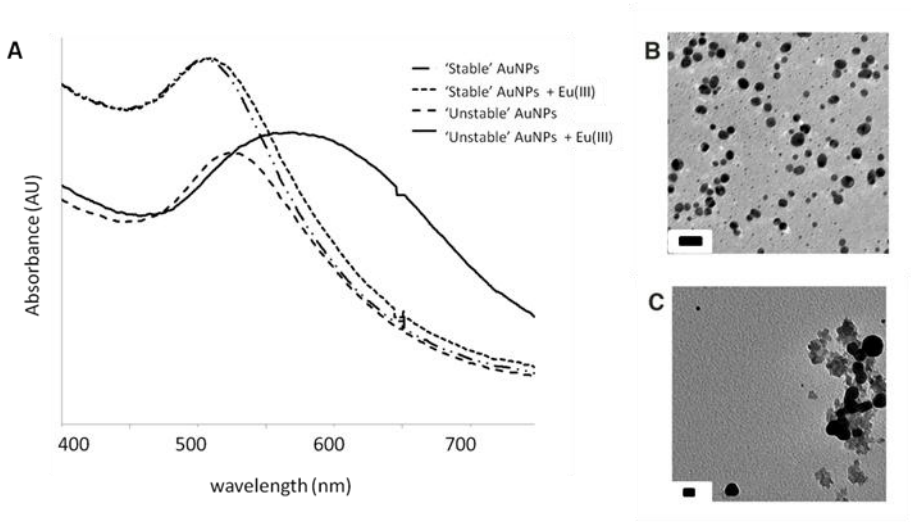

Figure 3.2: UV-vis spectra and TEM micrographs reveal that 6.0 nm MEEE-functionalized AuNPs produced in different batches under particular synthetic conditions (1:6 L:Au, 2.5:1 BH_4^-:Au, 24 °C) have different in-solution stability. Both 'stable' and 'unstable' MEEE particles have a plasmon absorbance at 520 nm, characteristic for NPs greater than 3 nm in size (A, dashed traces). The 'stable' MEEE-AuNPs show no response to the addition of Gd^{3+} (A, dashed trace), suggesting the particles remain dispersed in solution. The addition of Gd^{3+} results in a rise of the baseline and bathochromic shift in the absorbance spectra of the 'unstable' MEEE-AuNPs (A, solid trace), indicating particle aggregation. TEM images support these UV-vis results, where the stable MEEE particles remain dispersed on the grid (B), and large aggregated clusters$^{\alpha}$ of NPs dominate the unstable MEEE AuNP sample (C). Scale bars are 10 nm. These batch-to-batch differences in particle stability were not observed in AuNP samples prepared under different synthetic conditions (e.g. 1:10 L:Au, 10:1 BH_4^-:Au, 24 °C).

The sensitivity to ionic strength and multivalent cation addition in the 'unstable' AuNP samples are not consistent with the behavior of monolayer-protected gold clusters (MPCs) with neutral, non-chelating ω-functionalities (like MEEE).[30-32] This type of sensitivity is more characteristic of ionically-stabilized AuNPs, such as citrate or ascorbic acid-protected AuNPs.[35-39] AuNPs synthesized using the MEEE thiol, under analogous

reaction conditions, did not show any instability. We also did not observe the same particle instability in the synthesis of MEEE-AuNPs using Bunte salts when using higher borohydride:gold ratios (e.g. 1:10 Au:BH_4^-) were employed. These differences in properties implied that there were key differences in the compositions of the ligand shells between AuNPs prepared using Bunte salts under different synthetic conditions). These differences in stability have not previously been reported.[4,5,9,30-32] Therefore, we hypothesized that the 'unstable' MEEE-AuNPs were unstable because they were not protected by a thiolate ligand shell. Having successfully defined the instability observed in these MEEE-AuNP samples, we attempted to correlate the stability of the AuNPs with their surface chemistry.

Correlation of Ligand Shell Composition with Stability. In order to determine whether the stability of the AuNP samples correlates with thiolate ligand shell formation, XPS analysis of the 'stable' and 'unstable' samples was performed. Careful examination of the XPS spectra of the purified AuNPs reveals two sulfur species present in different amounts in both the ligand shell of the 'stable' MEEE-AuNPs and the 'unstable' MEEE-AuNPs. In addition to the gold-bound thiolate doublet observed at 162.5 eV, doublets are seen at 163.5 eV, and 168.6 eV in both the 'stable' and 'unstable' MEEE-AuNP samples.[4,5,28,29] These two sets of doublets correspond to the two sulfur atom types in the Bunte salt ligand precursor (Figure 3.3). Inspection of the spectra shows that the 'stable' particles possess significantly more thiolate in their ligand shells than the 'unstable' samples. The spectra of the 'unstable' MEEE-AuNPs show that the Bunte salt doublets (and some additional oxidized sulfur, 168.6 eV) dominate the spectrum,[β] with only a

small contribution from the thiolate doublet, indicating that the 'unstable' particles are primarily protected by adsorbed Bunte salts. These observations are further borne out by a determination of the thiolate:Au ratio in each sample.

We found that the thiolate:Au ratio observed in the stable particle sample was 0.15 ± 0.02, while that of the unstable sample was 0.04 ± 0.02, confirming that the stable AuNPs are protected by a thiolate monolayer, but the unstable AuNPs are not. Assuming a footprint for the thiolate of 21.0 $Å^2$, for a 5.0 nm particle protected by a fully formed thiolate monolayer, the thiolate:Au ratio should be 0.17, while for a 7.0 nm AuNP, the thiolate:Au ratio should be 0.10.[28,29] Thus, analysis of the thiolate:gold ratios confirms the observations made in the cursory analysis of the XPS spectra, as the 'stable' AuNPs possess a much more complete thiolate ligand shell (~90% of the ideal thiolate:Au ratio for a full monolayer) than the 'unstable' AuNPs (< 33% of the ideal monolayer coverage), and demonstrates that AuNP instability is correlated with the lack of a thiolate monolayer on the particle surface.

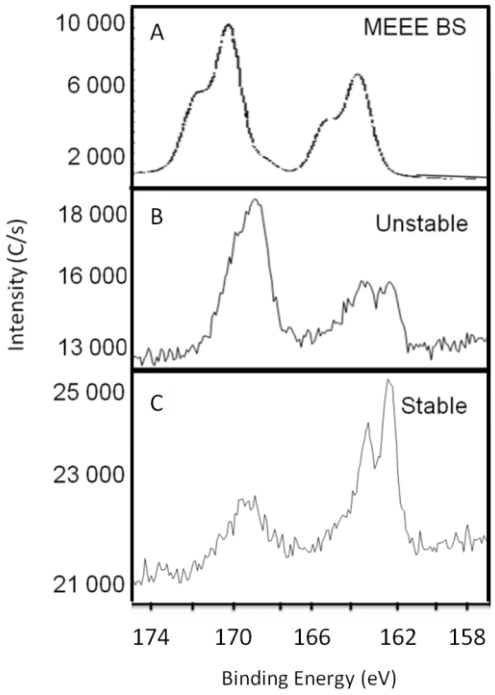

Figure 3.3: XPS analysis shows that stable and unstable gold nanoparticles have distinctly different monolayer characteristics. (A) XPS spectrum of the MEEE Bunte salt. (B) XPS spectra of 6.0 nm gold nanoparticles (AuNPs) with ligand shells primarily composed of adsorbed Bunte salts ('unstable' particles) and (C) completely monolayer-protected 'stable' particles. Both AuNP spectra indicate the presence of oxidized sulfur, but the analysis of the stable particles shows a much higher thiolate:Au ratio (0.17), compared to the unstable AuNPs (thiolate:Au = 0.05). This indicates that the stable particles are protected by a fully-formed thiolate monolayer (162.5 eV), while the unstable particles are not. Both spectra show evidence of adsorbed Bunte salt (163.5, 168.5 eV), but this species is much more prevalent on the surface of the 'unstable' MEEE-AuNPs. Some additional oxidized sulfur (168.5 eV) is also present in the spectra of the unstable AuNPs, probably a sulfite-like species retained after cleavage of the sulfur-sulfur bond in the Bunte salt. Binding energies were referenced to Au 4f (84.0 eV).

Given that AuNPs with a higher Bunte salt content in their ligand shell are susceptible to agglomeration in the presence of multivalent cations, it is likely that this

agglomeration is the result of particle cross-linking brought about by Bunte salts on adjacent particles complexing the metal cations. The ligand shells of the 'unstable' AuNPs will have an abundance of negatively charged thiosulfate groups available on the particle surface. Thus, any Bunte salts that have the negative thiosulfate group exposed to solution may complex with the cations, and the cations may induce cross-linking between two AuNPs, leading to the observed irreversible aggregation.[33-34] The ligand shell of the stable AuNPs, by contrast, is composed neutral thiolates that do not complex with multivalent cations, and form a significant physical barrier to agglomeration, so cation addition does not induce particle cross-linking.

It is not immediately clear, however, why in the synthesis of some MEEE-AuNPs, the thiolate ligand shell failed to form. The synthesis of AuNPs protected primarily by adsorbed Bunte salts has no direct precedent, nor have AuNPs or bulk gold films prepared using Bunte salts have ever been shown to possess a surface coating composed primarily of the unconverted ligand precursor.[4-8,25-27] The successful isolation of these Bunte salt-stabilized intermediates suggests that some reaction parameter affects the extent of monolayer formation on the AuNP surface.[γ] Given that the Bunte salt must be reduced to the thiolate to form a bond to the AuNP surface, the most likely parameter that might affect the conversion of the Bunte salt to the thiolate is the borohydride:gold ratio used in the synthesis. We have also previously observed no evidence of particle instability or a lack of thiolate ligand shell formation when Bunte salt-derived AuNPs are synthesized at higher borohydride:gold ratios.[5]

The Role of Sodium Borohydride in Thiolate Monolayer Formation from Bunte Salts. In order to test whether the borohydride:gold ratio influenced the formation of stable AuNPs, we prepared 7.0-10.0 nm MEEE-stabilized gold nanoparticles using various borohydride:gold molar ratios (1.5:1, 5:1, and 10:1 BH_4^-:Au). We attempted to prepare particles of similar size in order to control for the possibility that AuNP size might influence the extent of ligand shell formation. The L:Au ratio and gold precursor concentration were held constant in each case.

The borohydride:gold ratio used in the synthesis had a noticeable effect on AuNP stability. The 1.5:1 BH_4^-:Au sample of AuNPs was not stable for long periods of time, and produced 10.0 nm AuNPs that agglomerated after 1.5 hours of stirring. The 5:1 BH_4^-:Au reaction produced AuNPs with a mean core diameter of 7.6 ± 0.7 nm, while the 10:1 BH_4^-:Au ratio produced AuNPs with a mean core diameter of 6.1 ± 1.1 nm (for TEM micrographs and further characterization, see the Supporting Information). The 5:1 and 10:1 BH_4^-:Au MEEE-AuNP samples were stable. Irreversible aggregation of these AuNPs could not be induced by cation addition, nor by extensive purification. This suggested that the 5:1 and 10:1 BH_4^-:Au MEEE-AuNP samples were protected by a thiolate ligand shell, while the 1.5:1 sample was not.

The elemental composition of the monolayers of all the samples, including the agglomerated material obtained at the lowest borohydride:gold ratio was analyzed by XPS (Figure 4). XPS analysis indicated that the AuNPs prepared with 5-10 molar equivalents of $NaBH_4$ were protected by a monolayer that was dominated by covalently bound thiolate ligands, but AuNPs produced with smaller amounts of sodium

borohydride showed significantly more oxidized sulfur in the XPS analysis, and appeared to be protected by adsorbed oxidized sulfur species (primarily Bunte salts). Indeed, the XPS analysis of the product prepared at a BH_4^-:Au ratio of 1.5:1 showed no bound thiolate sulfur at all. In contrast, the AuNP syntheses performed at higher BH_4^-:Au ratios show extensive thiolate-gold bonding, with thiolate:Au ratios that are consistent with extensive thiolate monolayers on the AuNP surface.

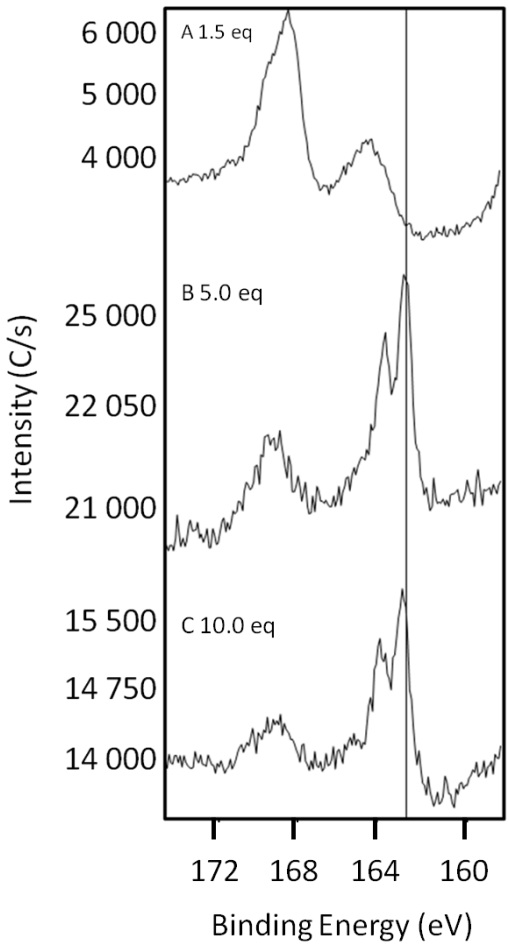

Figure 3.4: XPS analysis of 7.0 nm AuNPs prepared using increasing amounts of borohydride at a constant gold (III) concentration. The data show that as the amount of reducing agent used in the synthesis increases, the extent of thiolate monolayer formation (162.5 eV) increases. (A) aggregated AuNPs prepared with 1.5 mols of borohydride with respect to gold (III) and 7.0 nm AuNPs prepared (b) with 5.0 mols of borohydride with respect to moles of gold, (c) with 10.0 mols of borohydride with respect to mols gold (III). As the concentration of borohydride increases, the thiolate:Au ratio increases, indicating a more fully-formed monolayer. At low borohydride concentrations, only strongly oxidized sulfur (168.5 eV) and adsorbed Bunte salts (163.5, 168.5 eV) are present on the AuNP surface. The line marks the 162.5 eV binding energy. All spectra were referenced to Au 4f at 84.0 eV.

The XPS analysis clearly demonstrates that ligand shell formation correlates strongly with the reaction conditions, particularly a large excess of borohydride. Therefore, when synthesizing AuNP using Bunte salt ligand precursors, the borohydride:gold ratio's effect on the ligand shell, as well as the size of the core should be considered. A borohydride:gold ratio of 5.0:1 or greater is required for thiolate ligand shell formation. At much lower ratios (< 2.0:1 BH_4^-:Au), AuNPs protected solely by adsorbed Bunte salts will be the predominant product, and these 'unstable' AuNPs will be susceptible agglomeration. The conditions under which we observed batch-to-batch variability between 'stable' and 'unstable' AuNP samples (~2.5:1 BH_4^-:Au), represents a "threshold" value, where additional reaction parameters may influence the formation of the ligand shell, and various combinations of oxidized sulfur species, Bunte salts, and bound thiolate may be observed in the ligand shell.[γ] Therefore to achieve reproducible thiolate ligand shell formation in this synthesis, a significant excesses of borohydride should be employed (> 5.0:1 borohydride:gold).

Formally, the conversion of the Bunte salt to the thiolate requires a reduction of the sulfur atom that will bond to the gold surface, and it is reasonable to expect that the reducing agent might play a role in this reaction. However, the participation of borohydride in this process represents a marked difference between the process of monolayer formation on gold films (where thiolate monolayer formation is spontaneous) and the formation of the ligand shell on AuNP surfaces. The details of the reduction of the Bunte salt to the thiolate is also not clear based on this XPS analysis. Is the

borohydride alone is sufficient to reduce the Bunte salt to the thiolate, or is it some cooperative interaction between borohydride and the AuNP surface that effects the reduction? It is also not yet clear whether the correlation between the borohydride:gold ratio and ligand shell formation may be generalized to all AuNP sizes, or whether there is a size-dependency in the ligand shell formation reaction.

Two Stage Conversion of Thiosulfates to Thiolates at the AuNP Surface. We next investigated whether the reduction of the thiosulfate occurs in solution or at the AuNP surface. It is known that the reduction of Bunte salts in solution is one method to generate thiols, but whether borohydride-induced reduction with proceed under these synthetic conditions has ot been investigated. Ju-Nam et al. showed several years ago that the reduction of a Bunte salt with borohydride in the presence of methyl iodide produced a thioether, but did not investigate the possibility that borohydride treatment alone could reduce the thiosulfate to the thiol.[8] In order to determine whether Bunte salt-thiolate conversions are accomplished in solution or at the surface of the growing AuNPs, we performed two experiments. We first treated an aqueous solution of the MEEE Bunte salt with sodium borohydride (at synthetically relevant concentrations) and examined the reaction by ^{1}H-NMR. We also attempted to isolate and convert AuNPs protected by adsorbed Bunte salts to thiolate-protected AuNPs by adding more borohydride to the 'unstable' particles (i.e.- treating the Bunte salt-protected AuNPs as isolable intermediates in the formation of thiolate-protected AuNPs).

In the ^{1}H-NMR experiment, we treated the Bunte salt of MEEE with sodium borohydride alone in aqueous solution (at concentrations identical to those that produce

thiolate-protected AuNPs), and monitored the solution for subsequent reactions. We found that the Bunte salt was not reduced simply by the addition of borohydride. Even after several hours of reaction time, the addition of borohydride to the MEEE Bunte salt produced no discernable reaction. Therefore, it is more likely that the participation by borohydride occurs after the ligand precursor has adsorbed to the AuNP surface. If sodium borohydride is responsible for Bunte salt conversion to the thiolate *after* Bunte salt adsorption to the AuNP surface, the addition of further sodium borohydride to an 'unstable' nanoparticle solution should initiate the formation of a thiolate ligand shell on the AuNP surface.

In order to test the ability of sodium borohydride to convert adsorbed Bunte salts to a thiolate ligand shell on gold nanoparticle surfaces, a sample of purified, 'unstable' MEEE AuNPs was treated with additional borohydride and the resulting changes in surface chemistry were evaluated using XPS analysis. The initial particle sample was prepared at room temperature using a 1:10 L:Au ratio and 2.0 molar equivalents of borohydride with respect to gold. The reaction produced a red solution of AuNPs with a mean core diameter of 9.8 ± 2.7 nm (Figure 3.5). The particles, as synthesized, aggregated upon addition of Gd^{3+} or after extensive diafiltration (> 20.0 volume equivalents). However, if the particle solution was minimally purified by diafiltration (10.0 volume equivalents), a solution of purified MEEE BS-protected AuNPs could be isolated, and stored for up to five hours before irreversible aggregation of the cores occurred. If these unstable MEEE BS-protected AuNPs are then treated with an additional 3.0 molar equivalents of borohydride (with respect to the original amount of

tetrachloroaurate, bringing the overall borohydride:gold ratio to at least 5.5:1), the particles display a slight blue shift in the surface plasmon resonance of the solution, and no longer agglomerate with the addition of Gd^{3+}. This indicates the successful conversion 'unstable' AuNPs to 'stable' AuNPs. In order to confirm that this conversion was indicative of a change in monolayer coverage, the composition of these particles' ligand shells were analyzed by XPS.

The purified AuNP solutions, one treated only once with sodium borohydride, and the other treated twice with borohydride, were analyzed by XPS. The spectra of the two samples showed that only Bunte salts and oxidized sulfur species were present on the surface of the particles that had received one borohydride addtion. However, after treatment with further borohydride, thiolate bonds to the gold core developed, with the thiolate:Au ratio increasing from 0.02 ± 0.02 in the first sample to 0.10 ± 0.02 in the twice-borohydride-treated sample (Supporting Information). Some oxidized sulfur and adsorbed Bunte salts were still observed in the ligand shell of the treated AuNPs, but the thiolate:gold ratio for the borohydride-treated sample suggests that thiolate coverage on the AuNP surface is extensive (the theoretical thiolate:Au ratio for a 10.0 nm AuNP is approximately 0.10). This XPS data confirms that borohydride plays an important role in the formation of the AuNP ligand shell in this size regime, but the presence of borohydride, and the surface of the gold nanoparticle are both required to effect the reduction of the Bunte salt. The unstable Bunte salt-protected AuNPs can therefore be regarded as isolable intermediates in the formation of large thiolate-protected AuNPs using this synthetic method.

The ability to isolate and manipulate these weakly-passivated AuNPs may have important synthetic consequences. The ability to convert the 'unstable' particles to ligand-stabilized clusters, coupled with the ^{1}H-NMR study of the reaction of borohydride with free Bunte salt in solution provides strong evidence that the Bunte salt adsorbs to the AuNP surface prior to thiolate formation, and can then converted, with the participation of the reducing agent, to the thiol. The ability to isolate Bunte salt-protected AuNPs may be useful in the synthesis of extremely large thiolate-protected AuNPs, as the ability to synthesize these weakly-passivated AuNPs may permit the growth of extremely large gold cores, which can then be converted to ligand-stabilized AuNPs simply by the addition of further sodium borohydride. In addition, the ability to generate these weakly-passivated AuNPs may open new synthetic strategies for the synthesis of AuNPs with mixed ligand shells.

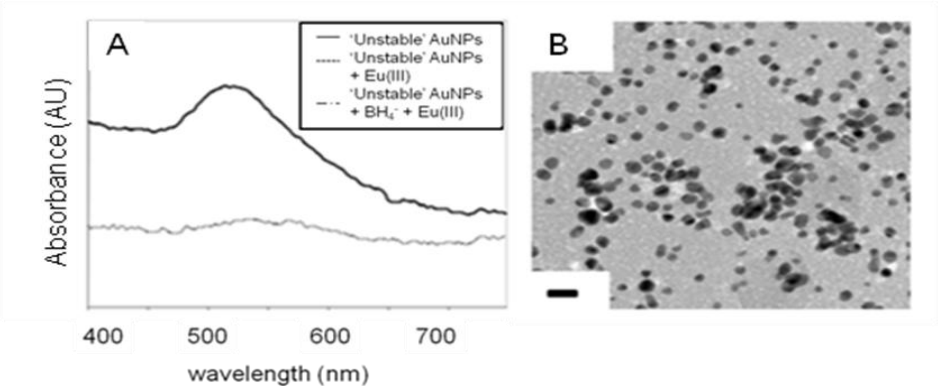

Figure 3.5. The addition of sodium borohydride to solutions of 'unstable' MEEE-functionalized AuNPs converts them to thiolate-protected AuNPs. (A) Absorbance data for unstable MEEE-AuNPs after the addition of further borohydride, and following the addition of europium nitrate. The AuNPs synthesized at a borohydride:gold ratio of 2:1 aggregate irreversibly upon cation addition. However, after treatment of the 'unstable' MEEE-AuNPs with further borohydride, the absorbance spectrum for the AuNPs remains unchanged following cation addition. This indicates that the additional borohydride has generated a thiolate monolayer on the AuNP surface, from the adsorbed Bunte salts. (B) TEM micrograph of the particles following treatment with further borohydride, and the addition of Gd^{3+}. TEM analysis confirms that addition of the lanthanide no longer induces AuNP aggregation, suggesting that the 'unstable' AuNPs have been successfully converted to 'stable' AuNPs. Scale bar is 20 nm.

Size-Dependent Surface-Catalyzed Monolayer Formation. In contrast to the studies just described for 5.0-10.0 nm MEEE-AuNPs, when small (d_{core} < 4.0 nm) AuNPs were synthesized using this method, the small particles were always stable to cation addition and purification, regardless of the synthetic conditions. We synthesized small gold nanoparticles using two different sets of reaction conditions: 1:1 L:Au ratio, with 4.0 molar equivalents of borohydride at 60°C produced AuNPs with a core diameter of 3.2 ± 0.7 nm, while at 3:1 L:Au, with 2.5 molar equivalents of borohydride at 2°C particles with a diameter of 2.1 ± 0.4 nm were produced. We investigated the ligand shell

composition of these small MEEE AuNPs by XPS. Both these particle samples were shown to have predominately thiolate monolayers by XPS analysis (Supporting Information). For the 3.0 nm AuNPs, the thiolate:Au ratio was found to be 0.27 ± 0.01, compared to an idealized thiolate:Au ratio of 0.31 for a 3.0 nm AuNP.[33,34] For the 2.0 nm AuNPs, the thiolate:Au ratio was determined to be 0.47 ± 0.02, compared to a calculated thiolate:Au ratio of 0.45.

These data suggest that borohydride does not play as significant a role in the formation of thiolate monolayers on the surface of AuNPs when the core diameters are less than 4.0 nm. Thus, the transformation of Bunte salts to thiolates at the AuNP surface is a size-dependent process, and for small AuNPs, the surface of the particle strongly affects the composition of the ligand shell. On the other hand, for AuNPs with core diameters greater than 5.0 nm, borohydride plays a larger role in determining the composition of the ligand shell. For small AuNPs, we could not isolate the same Bunte salt-protected AuNPs that we obtained in the synthesis of the larger AuNPs, regardless of the reaction conditions, suggesting that if this intermediate species occurs in the reaction pathway, it is transient, and rapidly converted to a thiolate-protected AuNP. Based on our observations, the process of ligand shell formation on small AuNPs is more similar to the mechanism of ligand shell formation proposed by Shon et al in the first synthesis of AuNPs using Bunte salts. The participation of borohydride in the formation of the ligand shell on small AuNPs cannot be entirely ruled out, but small AuNPs (d_{core} < 4.0 nm) have been shown to catalyze a number of organic oxidation and reduction reactions, and this may also extend to the reduction of Bunte salts to thiolates.

Reaction Pathway for the Formation of AuNP Ligand Shells from Bunte Salts.

Figure 6 describes the reaction pathway by which the thiolate ligand shell forms from Bunte salts at the gold nanoparticle surface during synthesis. The precursor compounds react with borohydride to produce a gold nanoparticle that is protected by an adsorbed layer of Bunte salts (Figure 6). The weak passivation by the Bunte salt is evidenced by the XPS analysis of our 'unstable' MEEE-functionalized gold nanoparticles, which clearly showed the adsorbed Bunte salt to be a prevalent species on the AuNP surface. This species represents an intermediate in the formation of the thiolate-protected AuNPs, and can be isolated for analysis or post-synthetic modification under the right conditions. For core diameters greater than 4.0 nm, this species will eventually aggregate irreversibly if no additional borohydride is available to reduce the Bunte salt. When excess borohydride is available, the Bunte salt undergoes a surface-mediated reduction to the thiolate. In the case of small gold nanoparticles ($d_{core} < 4.0$ nm), the Bunte salt-protected intermediate is transient, and the conversion of the Bunte salt to the thiolate appears to be rapidly effected by the particle surface, with minimal participation from sodium borohydride. In both size ranges, this reaction ultimately results in a particle that is protected by covalently bound thiolate, with some adsorbed Bunte salts occupying defect sites in the monolayer, depending on the solubility of the ligand and ligand precursor.[4,5,29-32]

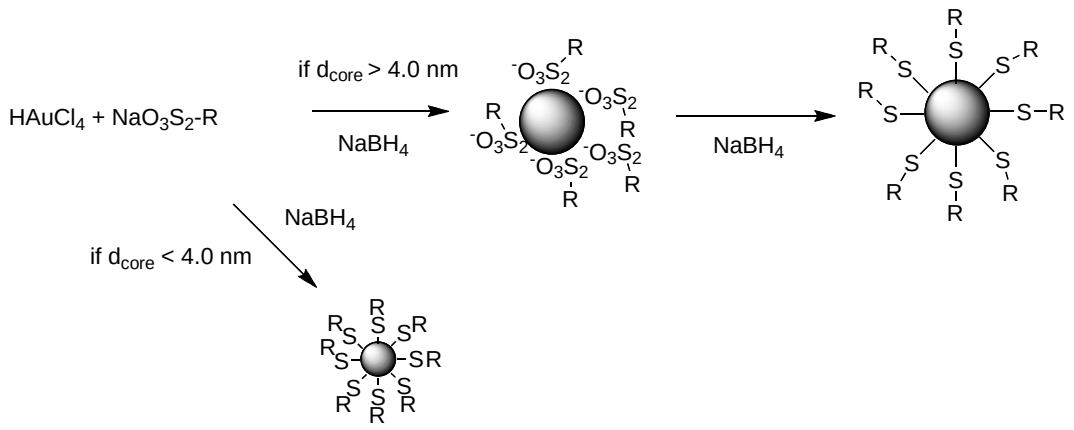

Figure 3.6: New proposed model for thiolate monolayer formation from masked thiols on the surface of AuNPs. The gold precursor and Bunte salt are reduced by borohydride to form a weakly-passivated AuNP intermediate. The formation of a thiolate monolayer on the AuNP surface is then assisted by the participation of further sodium borohydride, depending on the size of the particle generated. In the absence of additional borohydride, large AuNPs cannot be stabilized by a thiolate monolayer, and ultimately aggregate irreversibly. Small AuNPs do not require the same level of participation from borohydride, and quickly proceed through the intermediate species shown to form thiolate-protected AuNPs.

Conclusions

The stability assays and XPS analyses undertaken in this study provide the first look into the reaction pathway by which Bunte salts are converted to thiolates at the surface of gold nanoparticles. This study demonstrates that the process by which the Bunte salts are converted to thiolate ligands on the nanoparticle surface is a size-dependent process that occurs in two separate steps. In the first step, the Bunte salt adsorbs to the surface of the growing gold nanoparticle, forming an electrostatically-

passivated intermediate. These Bunte salt-protected gold nanoparticles can be isolated from the reaction mixture for further study or conversion to thiolate-protected gold nanoparticles in a separate step. In the second step, the adsorbed Bunte salt is converted to a gold-bound thiolate, and the formation of this organized ligand shell passivates nanoparticle growth. Nanoparticle synthetic reaction conditions (particularly the borohydride:gold ratio) actually influence ligand shell composition, in addition to the size and dispersity of the AuNPs produced. However, the ligand shell formation process is size-dependent. The formation of the thiolate ligand shell is much less dependent on sodium borohydride for AuNPs with core diameters less than 4.0 nm. It is clear that the formation of the thiolate ligand shell from Bunte salts on AuNP surfaces is a more intricate chemical process than spontaneous thiolate monolayer formation from Bunte salts on gold films. It is possible that some of the key findings regarding ligand shell formation made here may be generalized to all protected thiols (thioacetates, Bunte salts, thiocyanates), which may in turn increase the synthetic utility of these specialized ligands. The observation that Bunte salt-protected gold nanoparticles can be synthesized, isolated, and independently converted to thiolate-protected gold nanoparticles may have consequences for the direct synthesis of extremely large thiolate-protected AuNPs or for the control of ligand shell composition.

Transition 3: The Role of Flow Reactors in the Synthesis of High-Performance Nanoparticles

The majority of gold nanoparticle synthetic reactions are performed in round-bottomed flasks or similar small-scale reaction vessels, and typically produce milligram

scale quantities of material.[2,46] However, as nanomaterial synthesis in the laboratory transitions towards the production of high-performance nanomaterials, a higher priority is placed on the ability to precisely control and monitor nanoparticle properties while simultaneously synthesizing nanomaterials on a gram scale (at minimum). Typical laboratory syntheses of nanomaterials are ill equipped to deal with these challenges.[46]

One approach to large-scale nanomaterial synthesis involves the use of flow reactors as synthetic platforms. Flow reactors provide an opportunity to produce large quantities of nanomaterials without changing the scale at which the synthesis is actually performed. Although the mixing of the reagent stream still occurs with μL or mL volumes, by continuously introducing new reagent stock into the reactors, large amounts of materials may produced. In addition to providing a method for large-scale synthesis, the design of the reactor provides opportunities to precisely control the timing and volume of reagent addition.[46] Flow reactors also provide an opportunity to incorporate various characterization techniques at different points (residence times) within the reactor structure. These monitoring methods can be used for quality control in synthesis, but can also be extended to the investigation of nanoparticle formation kinetics.

We anticipated that by adapting the synthesis developed in Chapter II for use in a flow environment, we could take a significant step in developing high-throughput methods for thiol-protected AuNP synthesis. In addition, the synthesis of nanomaterials in a flow reactor environment might provide a successful strategy for investigating the kinetics of nanoparticle core growth to complement our investigation of the chemistry of

ligand shell formation described in Chapter III. The strategy we took to achieve these goals involved three stages.

1. The synthesis of thiol-protected AuNPs in a simple microfluidic device with an in situ UV-vis observation cell was attempted as a proof-of-concept study to show that nanoparticle properties (such as size) could be controlled effectively and monitored in the microfluidic environment. This study is described in Chapter IV.
2. We adapted the synthesis for a larger-scale, more flexible synthetic platform, a capillary flow reactor with a specially designed observation cell that allowed for simultaneous UV-vis and SAXS monitoring. This reactor setup provided an opportunity to quantitatively determine AuNP core diameters immediately following synthesis. This study is described in Chapter V.
3. We utilized the capillary flow reactor platform to study the growth of AuNPs during the synthesis described in Chapter II. This study is described in Chapter VI.

Notes:

α- The stability of AuNPs against cation addition became part of our standard analysis for AuNP stability during our investigation of AuNPs as colorimetric lanthanide detectors.[12] We tested the stability of the AuNP solution against the addition of lanthanides (such as Eu^{3+} and Gd^{3+}), as well as multivalent transition metals (Fe^{2+}, Cu^{2+}, etc.). We used mercapto-ethoxy-ethoxy-ethanol (MEEE) AuNPs as non-lanthanide-binding controls.

β- In this context, we are using aggregation to denote the assembly of nanoparticle clusters in solution (as evidenced by a red-shift and broadening of the surface plasmon absorption in the UV-vis spectrum). After TEM analysis, we found that during aggregation, the gold cores of the AuNPs had fused together (agglomeration). Hereafter, we will refer to this irreversible aggregation as agglomeration.

γ- We tested the effect of a variety of associated reaction parameters on the tendency to form 'stable' or 'unstable' AuNP samples at the threshold conditions (0.25:1:2.5 L:Au:BH_4^-). We found that reaction parameters such as stirring rate and the timing of reagent addition had an influence on the tendency to form 'stable' and 'unstable' AuNPs under these conditions. The details of these studies are provided in the Supporting Information.

CHAPTER IV

SYNTHESIS OF THIOL-STABILIZED GOLD NANOPARTICLES IN A SIMPLE MICROFLUIDIC DEVICE WITH PRODUCT MONITORING PROVIDED BY REAL-TIME UV-VIS ABSORBANCE SPECTROSCOPY

Note: The work presented in this chapter is the result of a collaboration between the author and Corey Koch, PhD, a graduate of the chemistry program at Oregon State University in Vincent Remcho's laboratory. The chapter was written entirely by the author. The microfluidic device described here was designed and tested by Corey Koch, while the author designed the nanoparticle synthetic reaction and characterized the nanoparticle products. The operation and monitoring of the device during nanoparticle synthesis was performed by both collaborators.

Introduction

The synthesis of functionalized gold nanoparticles with narrow size distributions and tunable core diameters remains a pertinent synthetic challenge, particularly when attempted on the gram scale.[1-3] The application of functionalized gold nanoparticles in biomedical treatments, imaging, and sensing applications has produced a demand for quantities of high-quality functionalized nanomaterials that existing laboratory-scale syntheses are ill-prepared to meet.[4-8] The synthesis of gram scale quantities of complex

nanomaterials by standard synthetic methods is often challenging, because changing the volume of reaction vessels or the concentration of reagents can introduce small variations into the concentration gradients across the volume of the reaction vessel, altering the properties of the product.[1,3,5] This has previously been circumvented by using seeded growth strategies to better separate the nucleation and growth of the nanomaterials, which provides an opportunity to retain the necessary control over size and shape. This approach is not suitable for many functionalized nanomaterials, however, such as thiol-protected gold clusters, whose growth kinetics are too rapid, and ligand shell passivates the particle surface too quickly for seeded growth approaches to be an effective route to their gram-scale synthesis.[1,3,5]

An alternative approach to addressing the challenge of synthesizing high-performance nanomaterials at scale involves using flow reactors as synthetic platforms to provide improved throughput and flexibility in the synthetic approach, and control over product properties.[5] Flow reactors have been used in a variety of chemical syntheses in order to prepare products with increased throughput.[2,5,9-22] Numbering up microfluidic devices to achieve high-throughput nanomaterial synthesis is a potential path to gram-scale nanomaterial synthesis because the continuous movement of the reaction mixture through the device permits the synthesis of significant quantities of material without changing the actual scale on which reagent mixing must occur.[5] In addition, flow reactors linearize synthetic reactions (i.e.- product passing through the reaction channel at a distance 5.0 cm away from the mixer will always represent a specific reaction time point in the synthesis), providing an opportunity to monitor product properties continuously

over the course of the reaction.[5] Finally, the ability to alter the geometry of the mixers in flow reactors, and to engineer the placement of various reagent addition points in the structure of flow reactors provides a method to precisely control reagent addition and mixing in ways that are not possible in batch syntheses.[5,14,23] Thus, flow reactors provide a potentially very appealing synthetic platform for the large-scale, controlled synthesis of complex chemical targets, like functionalized nanomaterials.

Many classes of nanoparticles have been synthesized in microfluidic devices, with varying degrees of success, but the synthesis of functionalized metal nanoparticles in microfluidic devices has yet to be extensively studied.[5,10-12,15,17-21,24,25] Many complex nanomaterial targets, including ligand-stabilized quantum dots and "encoded" multifunction nanoscale polymers have been synthesized in microfluidic devices.[5,24,25] However, the synthesis of metal nanoparticle in microfluidic devices has been restricted to very simple synthetic targets, primarily spherical gold nanoparticles (AuNPs) protected by adsorbed organics.[5,17-19] However, the synthesis of more complex gold nanoparticle targets, such as thiol-protected gold nanoparticles and anisotropic gold nanoparticles has not been investigated in microfluidic devices to any significant degree,[5,17-19] even though these AuNPs are relatively simple to synthesize in the laboratory *via* batch methods and are the preferred materials for most applications. ω-functionalized, thiol-stabilized AuNPs are desirable synthetic targets because they possess excellent stability and the composition of their ligand shell is tightly controlled.[32] To date, however, there has been only one reported direct synthesis of thiol-protected AuNPs in a microfluidic device, and

this was accomplished without demonstrating a reliable method for size control or any improvement in synthetic performance or product quality versus the synthesis in batch.[5]

The synthesis of more complex nanomaterial targets in microfluidic devices is just one challenge in the development of flow-based synthesis for functionalized nanomaterials. Song et al. recently highlighted a number of key challenges that need to be addressed in order to develop flow syntheses that are appropriate for large-scale nanomaterial synthesis of functionalized nanomaterials. In addition to the synthesis of more sophisticated nanomaterials in flow reactors, appropriate methods for NP shape and size control must be demonstrated, sufficient quantities of these materials must be amassed to demonstrate that their composition and properties are identical to their batch counterparts, and the ability to incorporate new analytical techniques into the structure of the reactor must be demonstrated.[5] Circumventing these challenges requires the exploration of new nanomaterial syntheses in flow reactors, as well as more extensive characterization of the product materials, which in turn requires the application of new strategies for reactor design and the application of new monitoring techniques.

This chapter describes the first synthesis of thiol-protected gold nanoparticles with controllable core diameters in a microfluidic device. This synthesis is performed in a versatile microfluidic device that incorporates a flow cell for continuous *in situ* qualitative monitoring of AuNP size during synthesis. The AuNPs can be synthesized with core diameters from 2.0-10.0 nm in diameter by varying the L:Au ratio used in the synthesis. The dispersity in core diameter (1σ) associated with the product, was between 20 and 25%, a slight improvement in monodispersity over what has been achieved in the

batch synthesis. However, the microfluidic device was found to be susceptible to fouling caused by deposition of nanoparticles within the reactor itself, necessitating that for the large-scale production of AuNPs, further modification to the reactor design (or the synthetic approach) must be made.

Experimental

Materials. Gold tetrachloroaurate trihydrate ($HAuCl_4 \bullet 3H_2O$) was obtained from Strem, sodium hydroxide caplets (Alfa Aesar), and sodium borohydride (99%) from Aldrich. The Bunte salt analogs of 2-[2-(2-mercaptoethoxy)-ethoxy] ethanol (MEEE BS), 6-mercaptohexanoic acid (MHA BS), and mercaptopentyl(tri-methylammonium) chloride (MPTMA BS) were synthesized as detailed in Chapter II. Deionized water (18.2 MΩ-cm) was purified with a Barnstead Nanopure Diamond system, and used where "water" is indicated for all experiments. All materials were used as received, unless otherwise stated.

Fabrication of the Microreactor. The microfluidic device was fabricated from a glass plate and a PDMS block by replica-molding polydimethylsiloxane. Reactor features were cast from molds made from SU-8 (Microchem, SU-8 2015, 2050, 3050) lithographic masters on silicon substrates.[14] PDMS chips were plasma-bonded to glass slides in order to prepare the finished reactor. Fluidic interconnections to the syringe pump and the UV-vis flow cell were formed by plasma-bonding Upchurch nanoports to the PDMS upper layer of the reactor.[14] This portion of the reactor was connected to a PDMS flow cell with fiber-optic adapters to allow for UV-vis absorption spectroscopy. The design and

fabrication of the UV-vis absorbance flow cell have been previously described.[23] The flow reactor utilizes a simple Y-mixer design for geometric focusing and faster diffusive mixing. The channels of the microreactor are 100 μm in diameter, and the exit port is 50 μm wide. The total length of the reactor is 3.5 cm. The UV-vis analysis flow cell is an additional 1.0 cm in length and the channel is 210 μm wide. The dimensions of the flow cell and the reactor setup are diagrammed in Figures 4.1 and 4.2.[14,23]

Characterization of Mixing Within the Microfluidic Device. The microfluidic mixer mixes primarily by diffusion and is features of a simple Y-geometry that mixes with geometric focusing. The mixing of the two solution streams in the mixer is described using the Einstein mixing model, which provides theoretical basis to evaluate the mixing time required for the two streams to completely join. Based on this model applied to a Y-mixing geometry, the diffusion distance (σ_x) can be calculated as follows:

$$\sigma_x = (2Dt)^{1/2} \qquad (1)^{14}$$

Where D is the diffusion distance across the mixer, and t is time. The length required for complete mixing can be calculated from:

$$l_{mix} = \mu\, w_l^2/2D \qquad (2)^{14}$$

Here, μ is the mean velocity (flow rate of the fluid) in the channels and w_l is the laminar width. For this system, the theoretical mixing time is projected to be on the order of 0.5 s. The geometry of the reactor is detailed in Figure 4.2. Complete mixing within the device was found empirically to occur within 0.27 s, as determined by the analysis of the formation of the iron thiocyanate by UV-vis absorbance spectroscopy.[14,23]

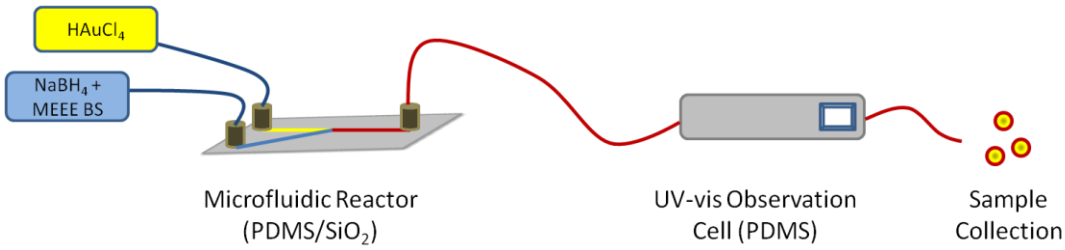

Figure 4.1: The microfluidic device used in these studies is composed of a PDMS-glass reactor containing a simple Y-mixer, which is connected to a PDMS flow cell monitoring device which allows for *in situ* monitoring of the AuNP product by UV-vis absorbance spectroscopy. The reactor system is driven by a simple syringe pump, connected to the reactor by check valve-mediated Nanoport attachments. The AuNP product is collected after exiting the observation flow cell.

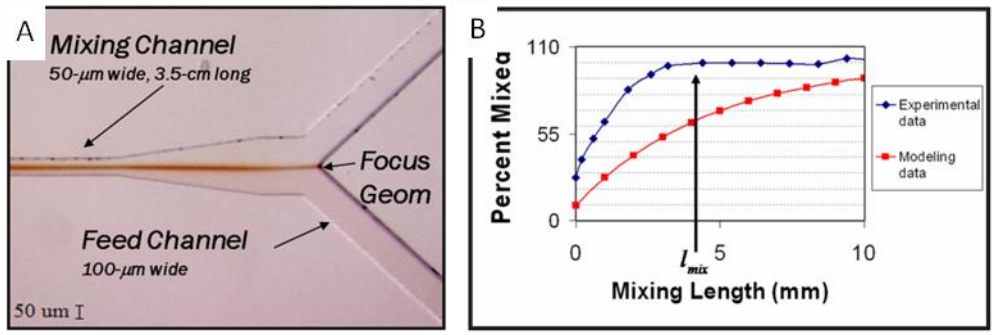

Figure 4.2: Geometry of the reactor mixer and mixing time profile for the microfluidic device. (a) The mixer portion is PDMS on the top and glass on the bottom, and possesses a Y-geometry that decreases the mixing time using geometric focusing. Here, the mixing line is visualized using an optical microscope and an iron thiocyante compound. (b) The percentage of the total volume of the sample mixed as a function of mixing length. The blue dots represent experimental measurements taken by UV-vis absorption spectroscopy using the formation of iron thiocyanate as a test reaction. The red dots represent the theoretical model data for the system.[14,23] (Reproduced with permission).

Gold Nanoparticle Synthesis. Gold nanoparticles were synthesized using a modified procedure based on the synthetic method described in Chapter II.[26] Two reagent stock solutions were prepared- one for the gold and ligand solution, and one for the reducing agent. To prepare the gold solution, 500 μL of 0.2 M $HAuCl_4$ was combined with 2.0 mL of 0.1 M NaOH. This solution was diluted to a final volume of 10.0 mL. The borohydride stock solution was prepared by dissolving 20.0 mg of sodium borohydride in 20.0 mL of water with variable amounts (10 μL-1.0 mL) of 0.01 M ligand precursor (Bunte salt) solution. These two solutions were inverted thoroughly to mix, and then allowed to stand for ten minutes.

Two syringes were filled with the stock solution described above and placed in a dual syringe pump (Kloehn 50300). The syringes were driven at a flow rate of 2.0-50.0 μL/min, and the mixing in the microfluidic device was monitored with an optical microscope attached to a camera, to ensure that mixing occurred reproducibly from run to run. Nanoparticle formation was evidenced by the formation of a faint red line in the middle of the reaction channel, which gradually spread to the entire width of the channel by the time in reached the end of the mixer.

In order to observe the effect of flow rate on nanoparticle size and aggregation, the flow rate at which the reaction mixtures were delivered to the device was varied from 6.0 μL/min to 50.0 μL/min. The particle size was monitored using UV-vis and TEM analysis.

Gold Nanoparticle Size Analysis. Gold nanoparticle samples were prepared for analysis by floating etched silicon dioxide TEM grids[27] on top of a drop of AuNP solution for 1 minute followed by copious rinsing with Nanopure water. A minimum of 200 nanoparticles per sample were used for size analysis. The TEM micrographs were then processed using Image J software to determine average core diameter, size distribution and standard deviation following the previously reported method.[28] UV-vis Absorption Spectroscopy analysis of the AuNPs was performed on a Mikropack DH-2000 UV-vis-NIR light source equipped with an Ocean Optics USB2000 spectrophotometer.

The size of the AuNPs produced can also be determined from the UV-vis absorbance data. Haiss et al. have shown that size can be quantitatively determined from the analysis of the UV-vis absorbance spectrum, by comparing the absorbance of the sample at 450 nm to the absorbance at the surface plasmon (SPR) absorbance maximum.[29] The relationship between the core diameter and the absorbance data is given by Equation 4.3:

$$d = \exp\left(3.00\left(A_{spr}/A_{450}\right) - 3.11\right) \qquad (3)^{29}$$

Haiss et al. demonstrated that this model provided a quantitative determination of AuNP core size that provides excellent agreement with TEM analysis of amine and citrate-protected AuNPs with core diameters between 3.0 and 100.0 nm. It should be noted, however, that while this model could be adapted to provide concentration data for AuNP solutions, successful application of the model provides no information on AuNP core

diameter dispersity. We anticipated that the use of this model might permit real-time quantitative monitoring of AuNP core size for sample synthesized within the reactor, but were mindful that changes in dispersity or the dielectric environment at the AuNP surface might prevent the acquisition of reliable quantitative core diameter data for all AuNP sizes.

Results and Discussion

In this proof-of-concept study, we attempted to demonstrate that thiol-protected gold nanoparticles of various desired sizes could be synthesized within the confines of a microfluidic device with real-time monitoring of product properties. We first sought to demonstrate that the UV-vis flow cell incorporated into the reactor provided adequate real-time monitoring of AuNP core diameter during the course of the synthetic reaction, and discuss the potential use the UV-vis analysis for quantitative monitoring of AuNP core diameter. We then attempted to demonstrate that core diameter could be controlled by varying simple reaction parameters, including the L:Au ratio. We also attempted to make comparisons, where possible, between the performance of the microfluidic synthesis and the analogous batch synthesis with respect to product properties and performance in terms of yield and throughput. We specifically detail the effective use time of a single reactor in this synthesis, and discuss the potential for device fouling due to AuNP aggregation within the reactor.

Gold nanoparticles can be readily synthesized within the confines of the microfluidic device, by mixing the two reagent solutions at various flow rates. The

standard gold nanoparticle synthesis is performed at a flow rate of 40.0 µL/min. When the two reagent stock solutions met in the mixer, a faint red line forms, indicating the formation of gold nanoparticles at the interface of the two reagent streams. This red color gradually spreads across the length of the channel, and the formation of AuNPs is confirmed when the product stream passes through the UV-vis flow cell, which shows a strong absorption near 520 nm, corresponding to the surface plasmon resonance absorption associated with gold nanoparticles. Upon exiting the reactor, the particle solution is diluted 1:4 (v/v) in water, and a small aliquot is removed for TEM analysis.

Assessing Product Properties Using UV-vis Absorbance Analysis *in Situ*. UV-vis absorbance spectroscopy provides a simple, rapid method for monitoring of AuNP size, both qualitatively and quantitatively.[2,26,29,30] UV-vis absorbance spectroscopy measurements can be obtained with millisecond time resolution, making UV-vis absorbance spectroscopy one of the few analytical techniques that can acquire real time data on the growth of gold nanoparticles.[2,9] The flow reactor utilized in this study employs a unique PDMS flow cell that contains a 1.0 cm path length, providing superior detection for UV-vis monitoring in nanoparticles synthesis devices, where the micron scale reaction channels otherwise reduce the amount of absorbing species present between the source and the detector at any given time.[14,23] It has previously been shown that the size of AuNPs greater than 3.0 nm in diameter can be determined quantitatively by monitoring the surface plasmon resonance absorption of gold nanoparticles, and comparing the maximum absorbance value to the absorbance at 450 nm, according to equation 4.3.[29] In addition to the quantitative size determination provided by Haiss'

model, UV-vis absorbance spectroscopy can also be used as a qualitative analysis method to monitor AuNP size. The rapidity and versatility of UV-vis absorbance spectroscopy make it an ideal simple analytical technique for real-time monitoring of AuNP size.

In order to assess the suitability of the *in situ* UV-vis apparatus for quantitative AuNP core diameter monitoring, we took absorbance data for solutions of AuNPs possessing different core diameters in the UV-vis flow cell, and compared the spectral signature and the sizes obtained to the TEM size analysis of the corresponding sample. The two AuNP samples contained mercaptohexanoic acid (MHA) functionalized AuNPs, the sizes of which were determined by TEM to be 5.5 ± 1.6 nm and 2.8 ± 0.8 nm, respectively. The TEM and UV-vis absorbance spectra for these samples are presented in Figure 4.3. Analysis of the UV-vis absorbance data using Haiss' model gave the sizes of the AuNP solutions as 5.0 and 1.2 nm respectively. The UV-vis-based size determination of the larger core diameter AuNP sample is in good agreement with the TEM data, but the analysis of the smaller core diameter AuNPs is not. This disparity is likely related to the relatively weak plasmon absorbance of 2.0-3.0 nm AuNPs,[31] making quantitative determinations of AuNP size by this method unreliable for AuNPs 4.0 nm and under. Therefore, we utilized the UV-vis absorbance measurements as a qualitative real-time measurement of AuNP core diameter during synthesis.

The disagreement between the TEM and UV-vis determination of AuNP size (for small AuNPs) observed in this study indicates that UV-vis absorbance spectroscopy is not a sufficient quality control method for monitoring gold nanoparticle size during synthesis within the flow reactor. Although UV-vis absorbance spectroscopy provides an

adequate qualitative monitoring technique to assess discrepencies between batches, additional instrumental analysis techniques must be utilized to determine AuNP size for good quality control in flow reactor-based synthesis. In addition, the failure of Haiss' model in the analysis of small AuNP sizes by UV-vis absorption spectroscopy indicates that Haiss' model may need further refinement to account for the effects of dispersity and possibly different passivating agents that are encountered during synthesis. With this in mind, we utilized a combination of UV-vis absorption spectroscopy and ex situ TEM analysis to assess how AuNP size could be controlled during synthesis in the microfluidic device.

Controlling AuNP Core Diameter Within the Microfluidic Device. The size of gold nanoparticles prepared in batch is typically controlled by varying the Ligand:Au ratio used in the reaction, and we anticipated that this method would also be effective within the microfluidic reactor.[2,7,30,32] By increasing the local concentration of the ligand relative to the gold precursor, more rapid passivation of nanoparticle growth is achieved, generating smaller AuNPs. Although this method of size control is the standard method used in batch, there has not been a demonstration that this technique can be used to control the size of thiol-stabilized AuNPs prepared in microfluidic devices. In our system, the concentration of the ligand was increased from 0.1 mM to 2.0 mM, while keeping the gold concentration constant at 1.0 mM, which resulted in the production of a red solution in the former case and a brown solution in the latter, indicating the formation of AuNPs with core diameters larger than 4 nm in the former case, and less than 3 nm in the second case. UV-vis absorption analysis supports this observation, as the solution synthesized at

a L:Au ratio of 1:10 shows a strong SPR absorption, while the 1:1 L:Au solution shows only a very shallow SPR absorption (Figure 4.3), consistent with the optical properties of much smaller AuNPs. This observation is further confirmed by TEM analysis, which shows that the AuNPs synthesized at a L:Au ratio of 1:10 possess a mean core diameter of $d_{core} = 5.5 \pm 1.6$ nm, while the solution synthesized at a L:Au ratio of 1:1 has a mean core diameter of 2.8 ± 0.8 nm.

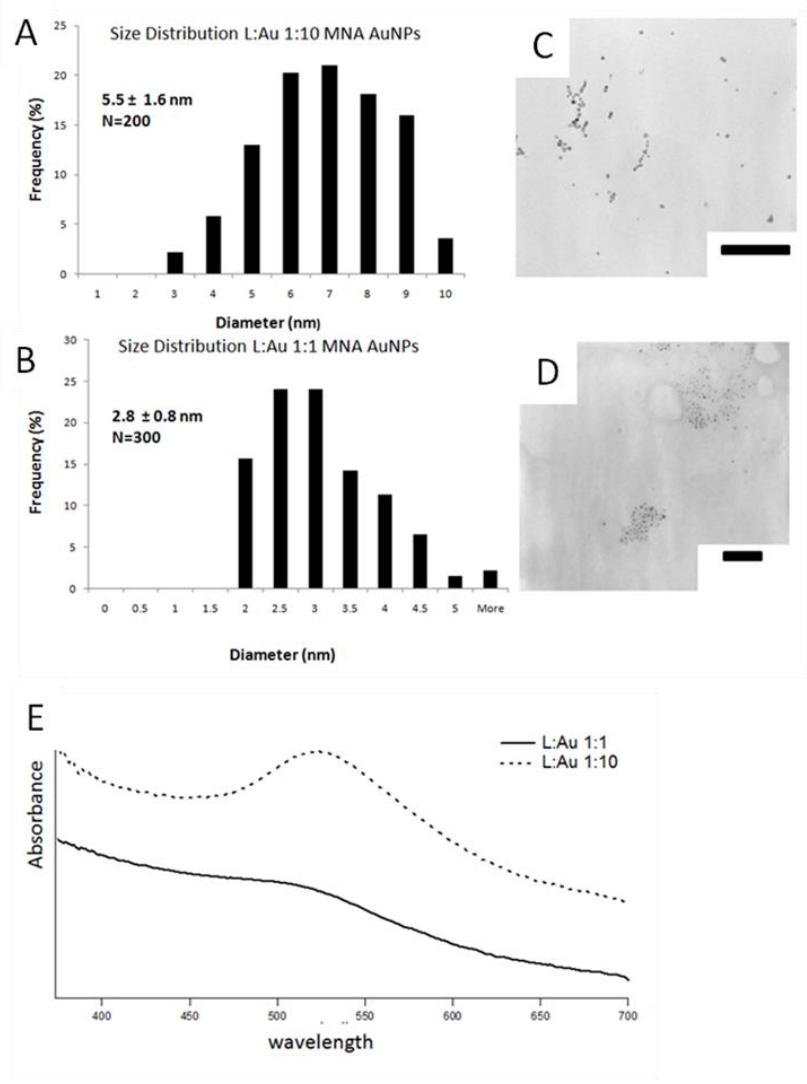

Figure 4.3: The size of the monolayer-protected cluster produced in the microfluidic device can readily be controlled by varying the L:Au ratio used in the reaction. (A) Size distribution data for a AuNP sample prepared using a L:Au ratio of 1:10- the mean diameter is 5.5 ± 1.6 nm. (B) When the L:Au ratio is increased to 1:1, the mean diameter changes, being reduced to 2.8 ± 0.8 nm. (C) TEM micrograph of the 1:10 L:Au sample, scale bar is 100 nm. (D) TEM micrograph of the 1:1 L:Au sample. Scale bar is 50 nm. (E) UV-vis absorbance analysis of the two samples shows that they have very different absorbance properties, consistent with the change in size observed by TEM.

This study represents the first time this level of size resolution has been achieved in the synthesis of monolayer-protected AuNPs within a microfluidic device. The fact that this level of size control can be achieved simply by varying the L:Au ratio bodes well for the use of this type of synthetic platform in the production of functionalized AuNPs, as relatively complex ligand-stabilized AuNPs can be prepared using simple synthetic strategies. Using this reactor, we have successfully demonstrated core diameter size control by varying the L:Au ratio for MEEE (mercaptoethoxy-ethoxy-ethanol), MTMPA (mercaptopentyl tri-methyl ammonium chloride), and MNA (mercaptononanoic acid)-functionalized AuNPs. The range of AuNP sizes achieved in this study is somewhat less than the range of particle sizes that has been produced in the analogous batch synthesis (1.5-20 nm),[26] though it is possible that by manipulating additional parameters (flow rate, reducing agent concentration, etc.) in the microfluidic synthesis of nanomaterials, that the range of available particle sizes can be expanded. We also observed that varying the flow rate and the reducing agent concentration used in this fluidic synthesis also influenced the core diameters of AuNPs produced by this method, but these methods of size control did not provide the same fine level of size control that the L:Au ratio provides in this particular device.

Comparison of Fluidic Synthesis Product Properties to Batch Products. Although we have demonstrated that the microfluidic device described here can be used to synthesize functionalized AuNPs with controlled properties, the quality of the AuNPs produced is also an important consideration. In the context of thiol-stabilized AuNP synthesis, product quality is measured primarily in two areas: the dispersity of core

diameter in the product and the coverage and order of the ligand shell on the particle surface.[32] While the dispersity in core diameter can readily be determined from the TEM analyses previously given, the compositional analysis of the ligand shell requires larger amounts of material (~milligram scale), which was not easily produced in the existing reactor setup because of frequent reactor fouling.

The core diameter dispersity of AuNPs produced in this reactor environment is comparable to the analogous nanoparticle synthesis prepared in batch. At all L:Au ratios observed, the polydispersity of the sample produced in the microreactor (1σ) was approximately 20% of the mean core diameter, with no size-based purification performed. Typically, after purification, most batch syntheses of monolayer-protected gold nanoparticles have polydispersities of 18-25% of the mean core diameter.[32] The batch synthesis of thiol-protected AuNPs using Bunte salts typically produced products with core diameter dispersities 20-27% of the mean core diameter.[26] Thus, there has been no significant improvement in the monodispersity of the product, a trend which has been observed in many syntheses of gold nanoparticles performed in microfluidic devices. Though it has previously been proposed that the increased control provided by microfluidic devices may extend to improving the dispersity of product versus batch synthesis, this has yet to be demonstrated for the synthesis of metal nanoparticles.[5]

In this particular case, deposition of gold nanoparticles within the reaction channel has increased the dispersity associated with these samples. AuNP deposition on the walls of the reactor was frequently observed (evidenced by blue plating on the walls of the reactor), and small, sub-micron scale pieces of this deposited material have been

observed to break off of the walls and enter the product stream. These large aggregates have been observed in the TEM analysis of the products (Figure 4.4). These liberated materials appear as large twinned-crystalline AuNPs. The appearance of these large AuNP species provide evidence that all AuNPs present in the product stream do not experience the same residence time within the reactor, but instead, AuNPs that remain within the reactor for extended times increase significantly in size, broadening the size distribution of the product. During the course of the average synthetic run, this particle aging only affects the size distribution, but over extended periods of operation, this type of nanoparticle aggregation can lead to complete reactor failure.

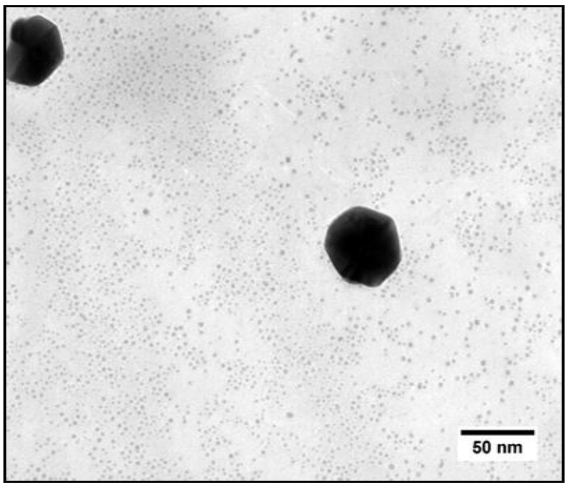

Figure 4.4: TEM micrograph of small AuNPs prepared at a flow rate of 40.0 uL/min. Even at these high flow rates, large AuNPs escape the confines of the reactor, having broken free from AuNP material adsorbed to the sides of the reactor walls. The presence of these poly-crystalline AuNPs broaden the size distribution of the AuNPs in the product stream, and over time, uncontrolled material deposition within the reactor can lead to device failure.

We were not able to generate sufficient material from these reactors to characterize the composition of the AuNP ligand shell, and confirm that the product AuNPs were protected by a thiolate monolayer. XPS and TGA analysis typically require milligram quantities of material, and frequent reactor fouling prevented the collection of sufficient material to perform the requisite analyses. Compositional analysis of nanoparticles produced by fluidic synthesis has often been an overlooked aspect of characterization in previous studies, but analyzing the composition of the ligand shell is an extremely important aspect of characterization in the synthesis of thiol-protected AuNPs. Therefore, the ability to adapt the existing reactor setup in order to generate more material per reactor (or per run) is a weakness of the device design investigated here that must be addressed in order to confirm the quality of the AuNPs produced in this system.

Adsorption of Nanoparticulate Material Within the Reactor Leads to Fouling. We observed that when the microfluidic device was operated for extended periods of time, even at high flow rates or decreased reagent concentration, extensive deposition of nanomaterial occurred within the reactor channels. This phenomenon could be readily observed through the camera situated above the device, and was evidenced by an extensive blue discoloration within the reaction channel. Over time, the blue material (deposited nanoparticle aggregates) would form a plug in the reaction channel (Figure 4.5), which would completely block fluid flow through the channel, and the build-up of pressure would lead to the rupture of the microfluidic device along the glass-PDMS seam.

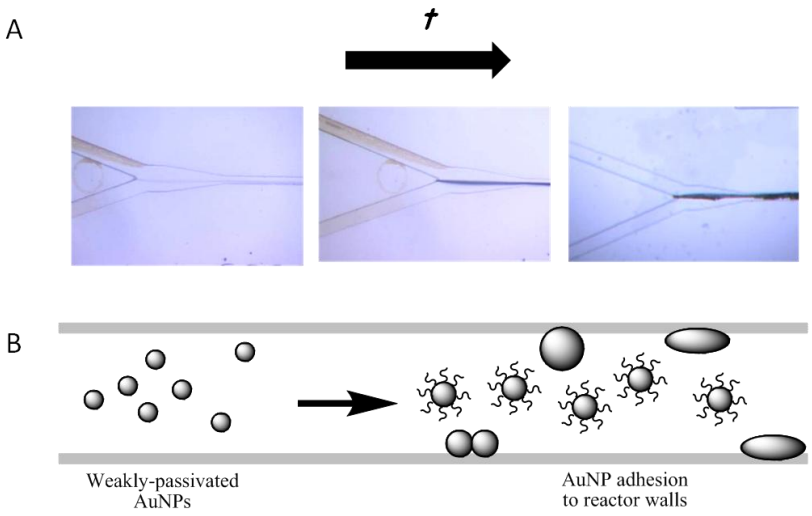

Figure 4.5: During the course of multiple synthetic reactions in the microfluidic device, aggregation on the walls of the channel causes significant fouling. (A) Captured images of the microfluidic device mixer during synthesis. Over time, nanoparticle formation (initially visualized as a thin red line in the center of the channel) leads to aggregation on the reactor walls, which ultimately leads to fouling and device failure. (B) Schematic of the adsorption process leading to fouling. Growing AuNPs with incomplete ligand shells deposit on the reactor walls, but fully protected AuNPs pass through directly. Adsorbed AuNPs grow to massive proportions as they experience longer and longer residence times. Ultimately, these deposits on the walls may restrict fluid flow to the point where the reactor fails.

The origin and chemical identity of the material deposited in the channels of the microfluidic device was not immediately clear. Such deposition and fouling had two likely origins, however. It is possible that the adsorption in the reaction channel was initiated by the non-specific uptake of ligand-stabilized AuNPs near the edges of the fluid flow, where there is contact between the liquid and the reactor walls. It is also possible that this AuNP adsorption results from the deposition of AuNPs that do not have a fully formed monolayer, and plate out onto the surface of the reaction channel, and this process

continues until a clog forms and the chip fails. This second scenario seemed more likely, as deposition of the particle material is first observed in the mixer itself, suggesting that particles at early residence times are more likely to deposit on the reactor walls.

In order to test whether the reactor fouling was due to non-specific adsorption of "finished" or "incomplete" AuNPs, we flowed AuNPs that had been previously synthesized through the microfluidic device at a concentration equivalent to the approximate concentration of gold nanoparticles achieved after synthesis is complete. We observed no deposition (i.e.- no development of dark blue film) of nanomaterial in the reactor when previously synthesized nanoparticles flowed through the system, even after multiple flows or extended run times. No deposition was observed regardless of the terminal functionality (positively charged, negatively charged, or neutral functionalized thiols) displayed by the gold nanoparticles. Nor did soaking a thin PDMS block or clean glass slide in concentrated AuNP solutions result in visible adsorption of the nanoparticles to these surfaces. This suggests that monolayer-protected AuNPs will not adhere to the reaction channels of the device, and that the reactor fouling observed during synthesis was the result of AuNPs not protected by a complete thiol monolayer plating out in the reaction channel.

Reactor fouling is a phenomenon that is common in the synthesis of nanomaterials within microfluidic devices.[5] There are several strategies by which the adhesion of particles to the reactor channels can be reduced, or the propensity for fouling can be decreased.[5] The interior of the reactor may be treated to reduce particle adhesion to the surface (a PDMS-glass microfluidic device is not well-suited for modification by

these processes), engineering solutions may be utilized to prevent synthetic mixture contact with the reactor walls, or the reactor dimensions may be increased, moving out of the microfluidic flow regime. If a reactor with larger channels is employed, there is less material in contact with the walls relative to the volume of liquid moving through the device, resulting in less deposition/unit volume, and reducing the frequency of device failure. In addition, larger reactors may be assembled out of low-cost, disposable components, eliminating the need to fabricate an entirely new system every time the reactor fouls.

Due to the significant aggregation that occurred within the microfluidic device, we were forced to conclude that this particular platform is not well-suited to the synthesis of functionalized gold nanoparticles on a significant scale, as the reactor cannot be operated for longer than approximately thirty minutes without fouling. Because of the frequent aggregation and reactor fouling, we were not able to successfully collect enough material from the microfluidic device in order to quantitatively compare the throughput of the microfluidic synthetic platform to the throughput of the analogous batch synthesis described in Chapter II. Based on the UV-vis absorbance data collected, we determined the concentration of AuNPs in the UV-vis flow cell, and from this, calculated a theoretical throughput (mg AuNP/min).[29] We found that the throughput for a single device was nearly twenty times lower than the throughput provided by the batch reaction (0.015 mg/min versus 0.3 mg/min). Thus, nearly twenty microfluidic devices would have to operate simultaneously to equal the synthetic output of a single batch reaction, and the

challenge of nanoparticle deposition within the reactor will have to be circumvented in order to keep the devices running effectively at long times.

Conclusions

The proof-of-concept study presented here successfully demonstrates that thiol-stabilized AuNPs can be synthesized in a microfluidic device, with size control afforded by varying simple reaction parameters, such as the L:Au ratio. In addition, the microfluidic device design described here permits real-time monitoring of product size by UV-vis absorbance spectroscopy. Over extended run times, uncontrolled aggregation occurred within the reactor channels, ultimately causing fouling of the reactor. Although the synthetic method was successfully realized within the confines of the microfluidic device, the fouling problems, the limited throughput of a single device, and the unsuitability of this device for quantitative assessment of AuNP properties during synthesis suggest that we might be better served by carrying out further investigations of AuNP synthesis using a different flow reactor design.

CHAPTER V

A SIMPLE CAPILLARY FLOW REACTOR PLATFORM FOR THE CONTROLLED SYNTHESIS OF THIOLATE-STABILIZED GOLD NANOPARTICLES WITH REAL-TIME QUANTITATIVE PRODUCT MONITORING

Note: The work presented here is primarily that of the author. Certain portions of the experiments were performed with the assistance of Patrick Haben and Sarah Brady. Sarah Brady was instrumental in the testing and assembly of the basic flow reactor setup, which was based on a flow reactor design originally developed by Lallie McKenzie. Patrick Haben led the initial study demonstrating that this flow reactor setup could be used to determine AuNP size during synthesis using SAXS and UV-vis absorption spectroscopy, with the assistance of the author. The author developed an effective synthesis that could be performed in the capillary flow reactor and investigated how the synthetic parameters could be used to control AuNP properties in different ways. The author also performed the *ex situ* characterization of all the NP samples described in this chapter. The authors would like to thank Steve Kevan, Alex Hexamer, and beam line scientists at the Advanced Light Source (Berkeley National Labs) for their assistance with SAXS measurements of gold nanoparticles in the flow reactor.

Introduction

The synthesis of functionalized nanoparticles in flow reactors potentially provides a number of advantages over the synthesis of nanoparticles in batch, but the translation of batch synthetic techniques of flow reactor systems also presents unique challenges.[1-9] The structure and geometry of flow reactors permits improved control over temperature and the timing of reagent introduction, which should result in nanoparticle products with better controlled properties.[1,8,9] In addition, flow reactors provide improved opportunities for monitoring, permitting the incorporation of *in situ* monitoring techniques to analyze the reaction mixture at different reaction times for the purpose of quality control or mechanistic investigations.[1-10] This versatility in reaction control and analysis makes flow reactors capable of acting as modular synthesis and characterization systems.[1,10-12] Despite the potential appeal of these systems, the field of nanoparticle synthesis is in flow reactors is still young and is faced with a number of challenges. Key challenges in the implementation of these syntheses include developing reactor-based syntheses for increasingly complex nanomaterials, complete characterization of the structure and composition of flow-synthesized nanomaterials relative to their batch counterparts, and demonstrating the incorporation of new monitoring techniques into the reactor's structure.[1]

While flow reactor syntheses for nanomaterials performed in microfluidic devices has received the most research attention, these pre-fabricated systems are not the only type of flow reactor platform.[1-10] Though a number of successful nanoparticle synthetic reactions and mechanistic investigations have been demonstrated successfully in

microfluidic devices, the micron-scale dimensions of these reactors present challenges in synthetic performance and characterization. For instance, the extremely small-scale reaction channels of microfluidic devices make these devices relatively susceptible to fouling, and when a device fails, the entire reactor must be replaced, which requires additional fabrication. In addition, the narrow reaction channels of these devices make it challenging to interface certain analytical characterization methods with microfluidic reactors, limiting the flexibility of these systems for reaction monitoring.[1] In contrast, larger-scale flow reactors (e.g- capillary flow reactors) can provide similar control over reagent addition, can be assembled primarily out of commercially available materials, providing additional flexibility in synthesis and analysis. The wider flow channels of the capillary flow reactors can reduce the frequency of fouling, and the flexibility of their configuration also allows for the facile incorporation of many complex analytical techniques, including small-angle x-ray scattering (SAXS).[12-17] When incorporated into capillary flow reactors, SAXS has been shown to be a valuable tool in the quantitative determinations of nanoparticle size and dispersity at different reaction times.[12-17] Despite the utility of a reactor platform that provides precise control over reagent addition with the ability to easily interface with complex monitoring techniques, the use of capillary flow reactors for nanomaterial synthesis has received little investigation.

The synthesis of nanoparticles in flow systems has thus far been primarily restricted to spherical particles protected by adsorbed organic molecules and polymers, even though more complex nanoparticles (ligand-stabilized nanoparticles, core-shell structures, and anisotropic nanoparticles) are generally more pertinent and applicable

materials.[1] Specifically, the majority of fluidic syntheses have focused on citrate or polymer-protected AuNPs, and isotropic quantum dots.[1-10,17-25] Thiol-stabilized AuNPs are an applicable synthetic target because of their exceptional stability, tightly controlled surface chemistry, and utility in sensing and bio-medical applications.[26-29] We recently developed an entirely aqueous direct synthesis for thiol-protected gold nanoparticles that utilizes hydrophilic-functionalized Bunte salts as ligand precursors in the formation of the AuNP ligand shell.[30] This synthetic method is well-suited for the synthesis of AuNPs in a flow reactor environment, as the batch synthesis offers core diameter size control *via* a number of different variables. In addition, this aqueous synthesis is completely compatible with the materials flow reactors are fabricated from and does not require a sophisticated mixing apparatus to be employed in the reactor (being a single-phase synthetic reaction).

A simple capillary flow reactor designed for the synthesis of 11-atom gold clusters was recently assembled in our laboratory by Lallie McKenzie.[32] This capillary flow reactor includes an observation cell that allows for simultaneous monitoring of the reaction mixture at various residence times by UV-vis Absorbance and Small-Angle X-Ray Scattering (SAXS). The reactor is assembled from commercially available Teflon tubing and T-mixers, connected to an observation cell cast from Kel-F, with mica windows, and can, with minor modifications, be adapted for the synthesis of thiolate monolayer-protected clusters (Figure 5.1). The design of the reactor allows the observation cell to be deployed at various reaction times by changing the length of tubing between the final mixer and the observation cell. This provides an opportunity to monitor

the properties of the AuNPs as they are synthesized. The observation cell also allows for simultaneous UV-vis absorbance and SAXS analysis. This reactor configuration provides an opportunity to qualitatively and quantitatively determine the size of gold nanoparticles produced *in situ* simultaneously, and may provide a simple method to investigate AuNP growth kinetics in real time.

In this chapter, we describe the construction of a capillary flow reactor as a platform for the *simultaneous* synthesis and characterization of thiolate-protected AuNPs We show that the capillary flow reactor functions as a versatile, high-throughput synthesis platform that can be adapted to meet a variety of needs, while providing *in situ* quantitative determination of AuNP size distributions as they are synthesized. We also demonstrate that thiol-protected AuNPs can be synthesized with core diameters between 2.0 and 7.0 nm using this device by varying synthetic parameters. For the first time, we also characterize the surface chemistry and composition of thiol-stabilized AuNPs produced in a flow environment. Finally, we demonstrate how the capability to simultaneously synthesize and characterize AuNPs in a single device permits the rapid and continuous synthesis and analysis of nanoparticles possessing discrete properties. The ability to synthesize and quantify NP properties in a flow reactor significantly increases the throughput for both nanoparticle synthesis and characterization versus traditional synthetic methods.

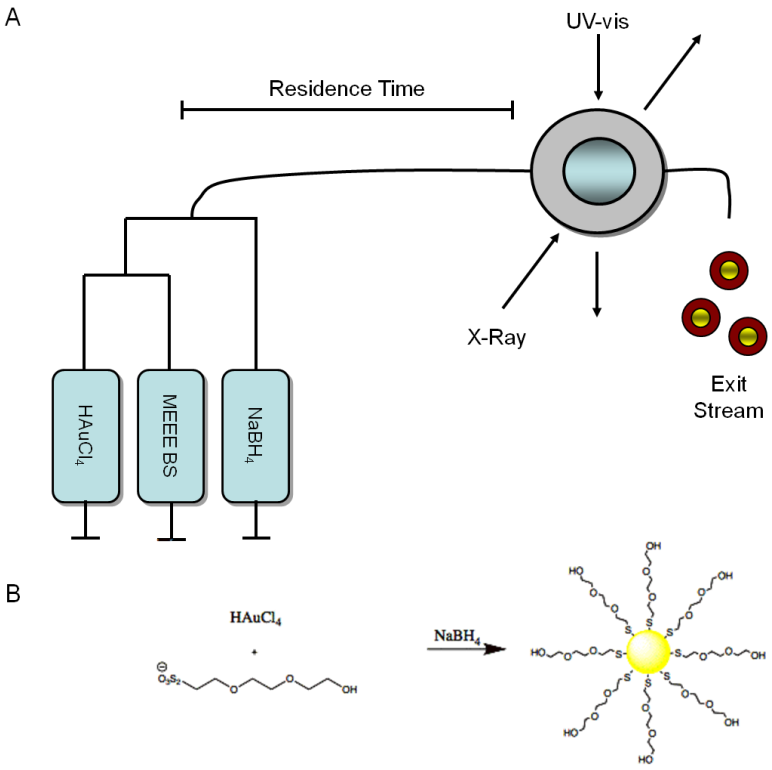

Figure 5.1: Flow reactor setup (A) optimized for investigation of AuNP syntheses and reaction cheme (B) for AuNP synthesis. Three syringe pumps are stocked with the three reagents necessary for AuNP synthesis. The fluid streams come together in simple t-mixers, and the tubing feeds into a KEL-F observation cell which allows for simultaneous UV-vis absorbance and SAXS analysis. The AuNP product is then collected directly as the material exits the reactor without reaction quenching. General reaction scheme (B) depicts AuNPs generated by using $HAuCl_4$ as the Au source, the MEEE BS (Bunte salt analog of mercapto-ethoxy-ethoxy-ethanol) ligand as the precursor to the passivating agent and $NaBH_4$ as reducing agent.

Experimental

Materials and reagents. Gold tetrachloroaurate trihydrate (Alfa Aesar), sodium borohydride (Aldrich), sodium hydroxide (Aldrich), and 2-[2-(2-chloro)-ethoxyethoxyethanol] (Aldrich), were obtained from their suppliers and used as received. The synthesis of the mercapto-ethoxy-ethoxyethanol Bunte salt analog (MEEE BS) was performed as previously described.[30] The capillary flow reactor was constructed from Teflon tubing (ID 760 μm, IDEX Health and Science 1520 XL) and t-mixers (Upchurch) that are commercially available.[32] The interior diameter in the flow channel of the observation cell was slightly smaller than that of the Teflon tubing (0.5 mm versus 760 μm). The flow reactor was driven by three Kloehn syringe pumps (Kloehn Versa 6 P/N, 54022), equipped with two 10.0 mL syringes, and one 25.0 mL syringe, respectively. The pumps were run using the programming software included with the Kloehn pumps. The path length for SAXS measurements in the observation cell was 750 μm. The observation cell included a port for UV-vis fiber optics, and recessed mica windows to allow for SAXS analysis. Absorbance data was acquired using an Ocean Optics USB 400 detector with an Ocean Optics DTS-Mini-20 Halogen/Deuterium lamp light source.

Reactor Assembly and Operation. The reactor consists of three computer-operated syringe pumps (Figure 5.1.A) connected by Teflon tubing with a 750 μm inner diameter to two T-mixers (500 μm id). The design of the capillary flow reactor has been described previously,[32] but briefly, three syringe pumps each contain one reagent stream (gold tetracholoraurate$_{(aq)}$, MEEE BS$_{(aq)}$, and sodium borohydride in basic solution,

respectively). The gold reagent stream mixes with the ligand precursor in the first T, and these reagents coexist in a single stream for five seconds prior to mixing with the sodium borohydride in the second T-junction, which initiates AuNP synthesis. The observation cell is then positioned a set distance from the second t-mixer, in order to observe specific residence times.

Gold nanoparticles were prepared using a variation of the standard method for MPC synthesis using Bunte salt ligand precursors.[30] In brief, a 5.0 mM aqueous solution of $AuCl_4$ was placed in syringe 1, a 1.0 mM solution of MEEE BS was placed in syringe 2, and a 2.0 mM solution of $NaBH_4$ in syringe 3. The sodium borohydride solution is made basic by the addition of sodium hydroxide, with the pH adjusted to approximately 10.5. This improves the synthesis of the AuNPs, reducing the tendency of the particles to aggregate within the reactor, as presumably the addition of the hydroxide makes the reduction of gold(III) to gold(0) more energetically favorable, providing for faster nanoparticle formation. The ligand precursor:gold ratio used in the synthesis could be adjusted to tune the AuNP core diameter, as can the BH_4^-:Au ratio. Once the AuNPs had exited the reactor, the particle solution was collected in a Corningware tube and diluted 1:2 with nanopure water. The NP solutions were dropcast onto copper-coated SiO TEM grids (Ted Pella), and after drying, underwent immediate TEM analysis. Size analysis was performed on the micrographs using an ImageJ-based analysis method. The monodispersity of the sample was measured by comparing the standard deviation in the mean core diameter in each sample (1σ).

The solutions were purified (removing small gold clusters and free ligand precursors) by diafiltration in a 50 kD membrane prior to compositional analysis by XPS.[31] Throughput was determined by taking the purified sample and lyophilizing a set volume to determine the dry weight. The same was done for the purified batch sample performed under the corresponding conditions. For XPS analysis, 20.0 μL of the purified solution was dropcast onto a Cr-treated silicon wafer, and allowed to air dry. Immediately after deposition, the sample was analyzed by XPS. The binding energies in these spectra were referenced to the Au 4f peak at 84.0 eV.

The flow rate of the reaction can be varied by altering the speed at which the syringe pumps operate. The standard synthesis (*vide supra*) was performed at three flow rates: 3.0 mL/min, 6.0 mL/min, and 9.0 mL/min, with a constant residence time of thirty seconds. The properties of the AuNPs that result from these synthetic conditions were determined by TEM and UV-vis Absorbance analysis.

UV-vis Absorption Analysis of Gold Nanoparticle Growth in Real Time. UV-vis absorption spectroscopy can be used as a semi-quantitative analysis technique to establish AuNP core diameter. In addition to collecting the full absorbance spectrum (300-800 nm) of the AuNP solutions at every residence time, we used a model for determining AuNP size from UV-vis absorption data that ratios the absorbance at the SPR maximum absorption to the absorbance at 450 nm.[33,34] This method provides accurate AuNP size determinations at a given residence time, but is less effective for AuNPs with core diameters less than 5.0 nm, and provides no data on AuNP dispersity at a given time. Therefore, we used UV-vis analysis as a qualitative analytical technique to provide rough

AuNP sizes at different residence times, and quantitative determinations of AuNP size were made by SAXS analysis.

SAXS aAnalysis of AuNP Populations at Specific Residence Times. SAXS analysis of the nanoparticle populations analyzed at each residence time provides quantitative size determinations for the trends indicated by the UV-vis absorbance data.[35-38] Small angle X-ray scattering provides a very sensitive quantitative method for determining AuNP mean size and dispersity at a given residence time. SAXS measurements were performed at Beam Line 7.3.3 at the Advanced Light Source (ALS, Lawrence Berkeley National Labs, Berkeley, CA). The X-ray source (mediated by a Mo/BC double multilayer monochromator) provides monochromatic X-rays at 10 keV, and the spot size at the sample is 1 mm horizontal × 0.24 mm vertical. The scattering intensity was recorded using Pegasus CCD detectors. The total *q* range provided by the detector system is between 0.004 and 8.7 A^{-1}. The total acquisition time for each SAXS measurement was approximately 5 min.[32] Several measurements were taken for each sample and averaged to determine scattering intensity. The observed scattering intensities were corrected by subtraction of the background (scattering of the solvent-filled observation cell).

Modeling and Analysis of SAXS Data. A full treatment of the method employed for analysis of the AuNP sample populations has been described previously.[32] Briefly, solutions of gold ions and small atomic gold species scatter X-rays minimally, so after proper background subtraction, the scattering signal will only result from the growing gold nanoparticles.[32] The scattering intensity can be related to the size distribution of the gold nanoparticles using the following equation:

$$I(q)= (\Delta\rho)^2 (n\int f(r)\, V(r)^2\, P(q,r)\, dr) \quad (1)^{32}$$

Where V(r) and P(q,r) are the volume and form factor for a sphere of radius r, while f(r) is the size distribution of the particle sample, which is obtained by fitting the SAXS data to a Gaussian distribution (2). $\Delta\rho$ is the difference in electron density between the particle material (gold) and the solvent (water). SAXS data were processed using IGOR Pro v6.02A software. SAXS data averaging, background subtraction, and conversion from 2D CCD images to 1D plots were performed using the Nika v1.17 macro. Application of models to the SAXS plots was performed using the Irena v2.27 macro. The agreement between the calculated patterns and the experimental patterns are excellent, as is the agreement between the sizes observed in each case and the sizes determined by UV-vis data.

Results and Discussion

We assembled a simple, versatile flow reactor with a multi-use observation cell in order to perform a direct synthesis of monolayer protected Au clusters in a flow reactor, while simultaneously characterizing the AuNP properties. We first demonstrated that the reactor permits *simultaneous* synthesis and quantitative analysis of nanoparticle samples by SAXS and UV-vis. Synthetic parameters, including reducing agent concentration, ligand-to-gold ratio, and flow rate, were varied to elucidate their effect on particle size and dispersity. In order to confirm the successful formation of thiolate-protected nanoparticles, the AuNPs were thoroughly characterized both with respect to their physical dimensions, and their atomic composition. We also assessed the reactor's utility

in the rapid synthesis of discrete nanomaterial products, including the ability to synthesize multiple nanomaterial targets from a single reagent stock. Finally, we project how this reactor can be employed as a self-contained system for simultaneous high-throughput gold nanoparticle synthesis and characterization.

Reactor Construction. The reactor was assembled using commercially available syringe pumps, tubing, mixers, and a custom-made observation cell machined from Kel-F (Figure 5.1A**)**.[32] The reactor was driven by three syringe pumps- one for each reagent stock solution. The syringe pumps were connected by tubing joined using standard T-mixers, which provided simple, but rapid mixing of reagents with complete mixing occurring in less than 3 seconds. The gold tetrachloroaurate and the MEEE BS solutions were mixed for five seconds before joining a basic sodium borohydride solution at the second t-mixer. For quality control purposes, the mean nanoparticle diameter could be determined simultaneously *via* UV-vis and SAXS, as enabled by the dual-axis observation cell (Figure 5.1A). Nanoparticles were synthesized using a direct synthesis method (originally developed as batch synthesis) in which functionalized Bunte Salts are used as ligand precursors to produce thiol-protected AuNPs (Figure 5.1.B). During the single-phase, aqueous reaction, Bunte Salts eliminate oxidized sulfur species to provide thiol-protected AuNPs where size control can be achieved by varying L:Au ratio and reducing agent concentration.

Simultaneous Synthesis and *in Situ* Analysis. An important feature of the reactor used in this study is the ability simultaneously synthesize and quantitatively monitor gold nanoparticles. Traditionally, gold nanoparticle core diameters are determined by ex situ

characterization methods (TEM, XRD, SEM, etc.) following synthesis. This significantly decreases the throughput associated with nanoparticle characterization, as TEM sample preparation and analysis may take up to one hour per sample. UV-vis analysis can provide a qualitative in situ determination of AuNP core size, but this is not usually a sufficient for the unambiguous determination of AuNP core size following synthesis. Small-angle X-ray Scattering provides an appealing alternative method for quantitative AuNP size determination that permits high-throughput AuNP size determinations. The observation cell incorporated into the flow reactor provides an opportunity to determine particle size quantitatively by SAXS and UV-vis at any given residence time either during synthesis or post synthesis.[32] This has implications for both quality control during synthesis and the ability to use this reactor setup for mechanistic studies of nanoparticle growth under actual synthetic conditions.

The successful size analysis of AuNPs by SAXS and UV-vis in this observation cell has previously been demonstrated, but the size analysis of AuNPs immediately following synthesis has not been evaluated. In order test the quality of data that we could garner on AuNP samples that had been synthesized within the reactor, we collected UV-vis, SAXS and TEM data for gold nanoparticle samples that had apparently completed their core growth within the reactor immediately prior to analysis (determined by examining UV-vis absorbance spectra over time, the AuNPs appear to have completed their growth after ~30s).

We used three independent methods to determine the size of AuNPs obtained at 60 seconds residence time, with a ligand:gold:borohydride ratio of 1:5:1 (Figure 5.2). The

60 s residence was time was chosen, because AuNP growth is complete in the reactor after 30s (as determined by UV-vis and TEM), and analysis of AuNPs that had completed their growth reactions would permit more accurate *ex situ* TEM characterization. The 60s AuNP nanoparticle solution was a strong red color, and showed a moderately strong plasmon absorbance at 518 nm.[33,34] Haiss et al. have shown that AuNP size can be quantitatively determined from the analysis of the UV-vis absorbance spectrum, by comparing the absorbance of the sample at 450 nm to the absorbance at the SPR absorbance maximum. The relationship between the core diameter and the absorbance data is given by Equation 5.2:

$$d = \exp\left(3.00\left(A_{spr}/A_{450}\right) - 3.11\right) \qquad (2)^{33,34}$$

Using this method, the size analysis yields an average diameter of 3.7 nm. It should be noted that Haiss' method dose not permit a determination of dispersity from the UV-vis spectrum.

The core diameter of the AuNP can also be determined by relating the scattering pattern observed in the SAXS analysis to the particle volume using Equation 5.3:

$$I(q) = |\Delta\rho|^2 \int |F(q,r)|^2 V^2(r)\, NP(r)\Delta\rho \qquad (3)^{32,35-38}$$

Here, the intensity of the scattering (I(q)), is related to the scattering contrast between the particles and the solvent ($\Delta\rho$), the form and structure factor (F(q,r)), the number of particles (N), the volume of the mean particle (V(r)) and the probability that the particle possesses a radius *r* (P(r)). Size analysis of the sample by SAXS gives a size distribution of 4.4 ± 1.9 nm.

In order to determine whether these two techniques gave accurate representations of the mean nanoparticle diameter, the resulting AuNP sample was analyzed by TEM. TEM size analysis gives the average core diameter as 4.6 ± 1.8 nm for the 60 s residence time sample. SAXS analysis of AuNP core diameter has previously been shown to provide excellent agreement with TEM analysis of AuNPs between 0.8 and 5.0 nm in diameter.

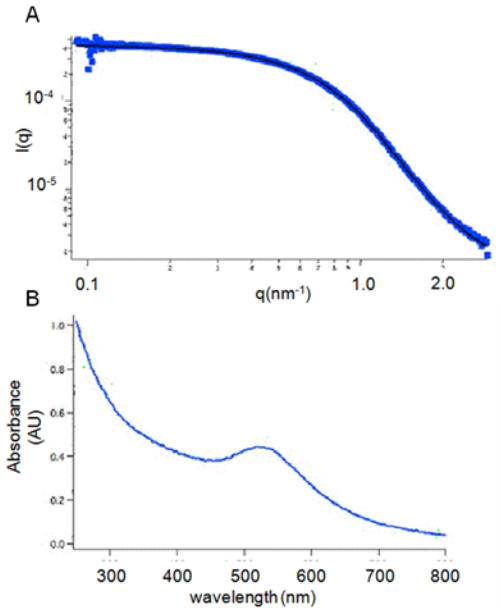

Figure 5.2: (A) SAXS pattern for AuNPs synthesized under 1:5:1 L:Au:BH_4^- conditions at 60-second residence time. The model fit to these data results in a size distribution of 4.4 ± 1.9 nm (compared to 4.6 ± 1.8 nm by TEM). (B) UV-vis absorbance spectrum for AuNPs synthesized under 1:5:1 conditions at 60-second residence time. Quantitative size analysis based on the UV-vis data indicates a diameter of 3.7 nm. The excellent agreement between the SAXS and TEM data provides an example of how *in situ* SAXS can be used quantitatively characterize AuNP size as the particles are synthesized.

The three techniques provide good agreement with one another, with the TEM and SAXS being in excellent agreement, and the UV-vis data, though typically within the standard deviation of the other measurements, reporting a smaller size in both cases (~ 80% of the diameter by TEM). In order to test the performance of these methods in quantitating AuNPs with smaller core diameters, we also analyzed AuNP samples prepared at a L:Au:BH_4^- ratio of 1:2:2 (60 s residence time) and found that the mean core diameter was 2.8 nm by UV-vis, 3.5 ± 0.4 nm by SAXS, and 3.3 ± 0.7 nm by TEM. There may be a bias in the use of Haiss' model for quantitating AuNP size at core diameters below 6.0 nm, as the absorbance properties of AuNPs change drastically between 5.0 and 2.0 nm, and other factors, such as the dispersity of the sample, or the refractive index/dielectric effects of the ligand shell may have a greater influence in this size regime.[29] Therefore, the data indicates that while the AuNP samples can be analyzed using two analytical techniques simultaneously as they grow within the reactor, UV-vis absorbance spectroscopy is more generally useful to assess the AuNP size qualitatively, while SAXS provides rapid and accurate quantitative analysis of the mean size of the particle sample.

Furthermore, the capillary flow reactor demonstrates that nanoparticle synthesis and *in situ* quantitative analysis can be coupled in a single device. The data presented above show that *in situ* SAXS provides accurate characterization data for AuNPs as they are being synthesized and that the size distribution data collected by SAXS reveals the same core diameter and dispersity data provided by TEM analysis. However, the ability to determine AuNP core diameter by SAXS significantly reduces the time required for

size analysis, as complete size data for a given sample can be collected during the AuNP synthesis, rather than requiring additional time for sample preparation and microscopy.

Synthetic Control Over AuNP Core Diameter. We next sought to assess the degree of synthetic control over AuNP size provided by the capillary flow reactor in this configuration. Previous research on the synthesis of citrate and ascorbic acid protected AuNPs in flow has shown that NP size can be influenced by changing the L:Au ratio, reducing agent concentration, and the rate of mixing.[26-29] By increasing the L:Au ratio, superior packing of the ligand on the developing AuNP surface contributes to the formation of smaller AuNPs. Similarly, by increasing the reducing agent concentration, nanoparticle nucleation is favored over monomer growth, decreasing the overall size of the AuNPs produced.[26-29] Finally, by increasing the flow rate of the fluids within the reactor, the mixing rate of the fluid streams should increase, which would again lead to more rapid nucleation and a decrease in the AuNP core diameter.[1] In order to demonstrate that AuNP size can be controlled within the flow environment, we investigated the effect of these reaction parameters on AuNP core diameter. We found that the L:Au ratio was sufficient for controlling AuNP core diameter over a wide size range (7.0 to 2.0 nm), but varying the BH_4^-:Au ratio or flow rates provided additional opportunities to control particle size.

Varying the L:Au ratio provides a simple approach for controlling AuNP size by a method that is analogous to how size control is typically effected in batch syntheses.[26-29] We synthesized batches of AuNPs using L:Au ratios of 1:10, 1:5, and 1:0.625, and determined the size of the NPs produced by *in situ* UV-vis and subsequent TEM analysis

(Figure 5.3). We found that, as expected, an increase in L:Au ratio resulted in a decrease in particle diameter. The UV-vis analysis indicated that the 1:10 solution possessed a strong plasmon resonance, consistent with AuNPs > 5.0 nm in diameter. In the 1:5 sample, a broad plasmon was present, consistent with particles 3.0-5.0 nm in diameter while the 1:0.625 sample showed a weak plasmon absorbance indicating the presence of ≤ 3.0 nm particles. TEM analysis confirmed the spectral observations. The resulting particle diameters were 6.1 ± 1.6 nm for the 1:10 sample, 4.3 ± 1.1 nm for the 1:5 sample, and 3.0 ± 0.8 nm for the 1:0.625 sample. This represents the first time that MPCs have been synthesized in a flow reactor with this degree of core diameter control, and additional size control can be afforded by adjusting the BH_4^-:Au ratio or varying the flow rate.

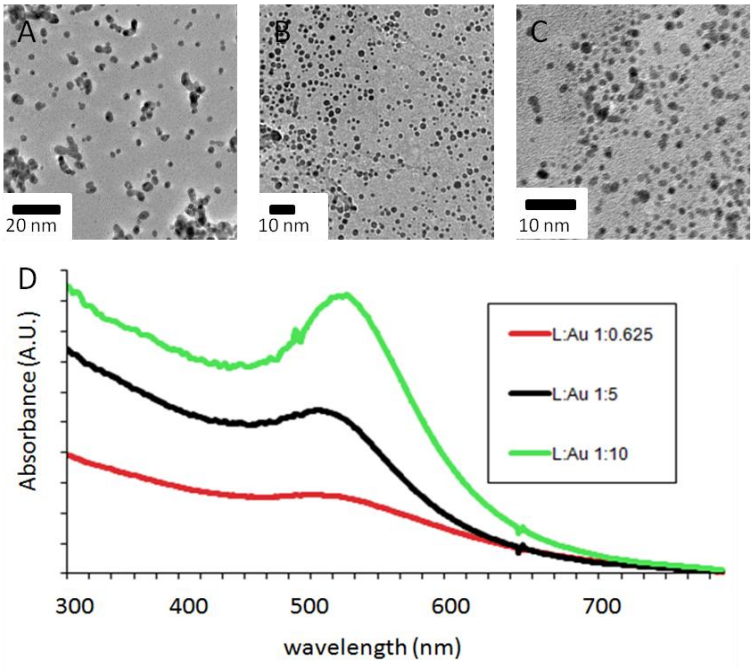

Figure 5.3: The effect of L:Au ratio on the diameter of AuNPs synthesized within the capillary flow reactor. (A) TEM micrograph of AuNPs synthesized at a L:Au ratio of 1:10 having a core diameter of 6.1 ± 1.6 nm. (B) TEM micrograph of AuNPs synthesized at a L:Au ratio of 1:5 having a core diameter of 4.3 ± 1.1 nm. (C) TEM micrograph of AuNPs synthesized at a L:Au ratio of 1:0.625, having a core diameter of 3.0 ± 0.8 nm. (D) In situ UV-vis absorbance analysis confirms that as L:Au ratio increases, particle size decreases.

The ability to tune particle size by changing the reducing agent concentration in flow syntheses where $NaBH_4$ acts as the reductant has not been extensively examined, though this behavior is well documented in the batch synthesis. For the flow synthesis described here, we investigated BH_4^-:Au ratios of 1:5, 2:5, and 3:5, to determine the effect on particle size. UV-vis analysis indicates that as reducing agent concentration increases, nanoparticle size decreases, and this was confirmed by TEM analysis. We also tested the effect of flow rate on nanoparticle core diameter by performing the synthesis at three different flow rates (3.0, 6.0, and 9.0 mL/min). We found that as flow rate increased, particle size decreased. UV-vis analysis shows that increased flow rate results

in a blue-shifted, less intense plasmon peak, indicating smaller particle sizes. TEM analysis shows particle sizes for 3.0 mL/min, 6.0 mL/min, and 9.0 mL/min of 5.5 ± 1.5 nm, 4.3 ± 1.0 nm, and 2.5 ± 1.2 nm respectively. Previous studies have shown that increasing the flow rate at which the synthesis is performed decreases the core diameter of the resultant particles, as the increased flow rate increases the rate of mixing. This faster mixing results in more extensive nucleation, leading to smaller particle sizes.[26-29]

Run-to-run Reproducibility in the Operation of the Reactor. We also wanted to assess the run-to-run reproducibility of the flow reactor setup. We found that the reactor could be run up to four successive times without replacing any components to yield products that were identical by UV-vis. After each successive run, there is visible nanoparticle deposition on both the mixer and the tubing shortly thereafter. If the reactor is run further (6-8 synthesis runs), eventually particle aggregation within the system will foul the mixer, causing the reactor to fail. The mixer and tubing can easily be replaced, making this reactor setup a more economically viable method to produce AuNPs than true microfluidic synthesis, where reactor fouling remains an all-to-common problem that necessitates fabricating an entire new reactor. Nevertheless, particle deposition within the tubing remains a concern on extended runs, as particles can break free of the tubing walls and affect the dispersity of the final product. Therefore methods to circumvent particle adsorption to the reactor walls must be investigated, including but not limited to surface treatments of the tubing interior.

Ligand Shell Composition of the Reactor Product. As mentioned earlier, there have been a number of microfluidic nanoparticle syntheses reported in the literature.[1-11]

However, there have been few examples of the synthesis of *functionalized* AuNPs. As a consequence, the size distributions of these particles have been extensively characterized, but the surface chemistry of these particles has been largely ignored. In the case of thiol-stabilized gold nanoparticles, it is especially important to verify that the ligand shells on these particle surfaces are comparable in quality to those prepared in batch. Therefore for the first time, we have investigated the ligand shell composition of AuNPs synthesized in flow by FTIR and XPS.

FTIR analysis indicates that the AuNPs are indeed functionalized with MEEE, as the spectra show bands for OH stretching (3400 cm^{-1}), CH_2 stretching (2850 cm^{-1}), and CO stretching (1120 cm^{-1}). The FTIR for the MEEE AuNPs is identical to the FTIR spectrum of MEEE AuNPs produced in batch. XPS analysis of unpurified 6.0 nm particles shows three sulfur oxidation states in the S2p region of the spectrum (Figure 5.4). The first doublet at 162.5eV corresponds to thiolate bound to Au, and this sulfur type occurs in a 1:6 ratio vs. Au. This further indicates that the particles are protected with a fully-formed thiolate monolayer, as we would expect that 6.0 nm thiol-protected AuNPs would show a thiol:Au ratio of ~1:5.[28] In the crude sample, two other sulfur oxidation states are apparent, with doublets occurring at 163.5eV and 168.6eV. These sulfurs peaks correspond to the two sulfur types in the MEEE Bunte Salt. In the purified sample, the oxidized sulfur peaks have almost entirely been removed while the thiolate peak remains, indicating that the ligand shell is primarily composed of thiol bound to gold with a few defects containing unreduced Bunte Salt, consistent with the monolayer characterization of the same MEEE-AuNPs produced in batch.

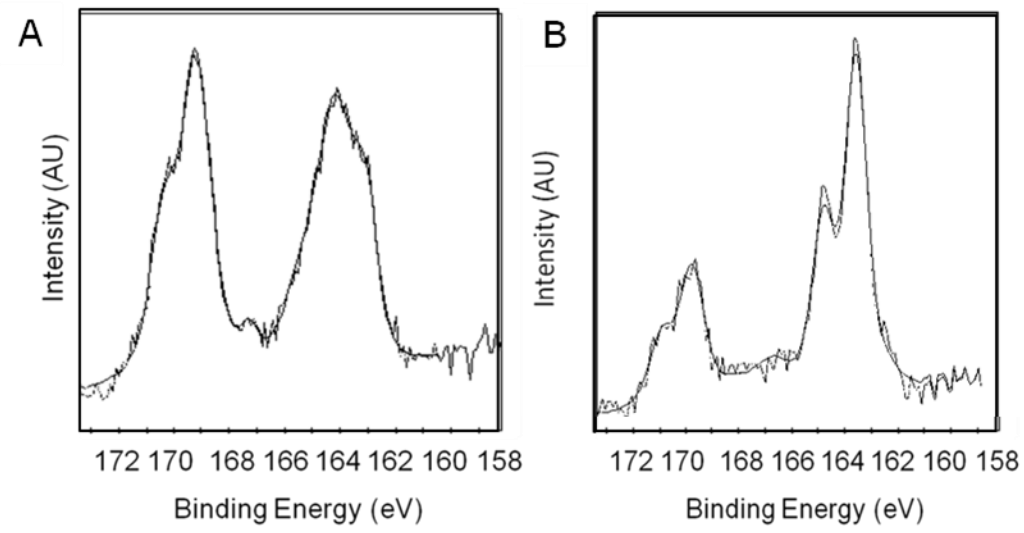

Figure 5.4: XPS spectra of unpurified (A) and purified (B) 6.0 MEEE AuNPs prepared in the capillary flow reactor. The XPS analysis suggests that the MEEE ligand shell is fully formed on the particle surface, after a residence time of approximately 30s. In the purified sample, only the thiolates remain on the surface with the presence of a small amount of the Bunte salt also detected.

The flow synthesis produces ligand-stabilized AuNPs in less than a minute of residence time while it takes nearly 3 hours to prepare these thiol-protected AuNPs in batch.[31] The point at which ligand shell formation on the MEEE-functionalized AuNPs is essentially complete can be assessed by removing an aliquot of the synthetic mixture and adding a small amount of aqueous lanthanide ions (see Chapter III).[28] It is potentially useful that monolayer formation on the particle surface occurs much more rapidly in flow. The rapidity with which ligand-stabilized AuNPs form in the capillary flow reactor is potentially useful for the analysis of nanoparticle properties or the rapid optimization

of syntheses. The origin of this rapid ligand shell formation is likely related to the speed of mixing within the reactor. Previous studies in our lab have indicated that $NaBH_4$ plays a role in converting the Bunte Salt to bound thiolate at the gold nanoparticle surface.[28] Therefore, it is likely that the improved mixing provided by the flow reactor allows for more effective action of the sodium borohydride, favoring the formation of high-quality thiol-protected AuNPs much more rapidly than is possible in batch. The rapid formation of the ligand shell on the particle surface also opens up the possibility that new nanoparticle ligand shell chemistry may be performed in the flow synthesis environment.

Synthetic Throughput in the Reactor. We suspected that this flow reactor platform could significantly improve the synthetic throughput of our Bunte Salt-based AuNP synthesis, because of the rapid rate at which nanoparticles are formed in the flow reactor (30 seconds vs. 3 hours in batch). In order to quantify the throughput, we ran three replicates of both a batch and a flow synthesis of MEEE-AuNPs and calculated the throughput for each synthetic setup, by lyophilizing the purified AuNP samples in order to determine the mass of AuNPs produced by each method. We found that the flow reactor setup provided approximately three times more material per unit time: 0.89 mg/min in the capillary flow reactor versus the 0.35 mg/min in the batch synthesis. The throughput of the capillary flow synthesis is perhaps surprisingly modest, but this value does take into account the rinses that must be performed between synthesis runs, and the swapping out of components that needs to occur to keep the reactor free from aggregates that may lead to fouling. The throughput of the flow reactor could potentially be improved by replacing the syringe pumps with peristaltic pumps, allowing for longer

synthesis runs. The improved synthetic throughput provided by the flow reactor opens up the possibility that this synthetic platform could be used for the rapid gram-scale synthesis of thiol-stabilized AuNPs, as only hours of continuous run time would be required to produce a gram of purified material.

Synthesis of Multiple Core Diameter AuNPs from a Single Reagent Stock. We attempted to demonstrate the versatility of the capillary flow reactor as a synthetic platform. Given the number of synthetic parameters that influence nanoparticle size in the flow reactor, this reactor system provides a number of options for controlling nanoparticle properties. As discussed earlier, changing the flow rate within the reactor will affect the mixing rate of the reagents and thereby influence particle size. The ability to synthesize particles possessing different properties or structures (in this case, different core diameters) during a single reactor run is potentially appealing for the controlled production of nanoparticle-based devices as well as research and development analyses that require the synthesis of a high volume of samples with different properties in a short period of time.[39-41] The ability to incorporate real-time SAXS analysis as a high-throughput method for nanoparticle characterization in this flow reactor enhances the potential utility of this platform for research and development studies.

We successfully synthesized AuNPs possessing discrete core diameters from a single reagent stock solution by adjusting the flow rate to 3.0 mL/min, 6.0 mL/min, and 9.0 mL/min while flowing the same reagent stock solution (1:5:1 L:Au:BH_4^-). We found that significantly different core diameters were produced at each flow rate, providing three distinct nanoparticle solutions. The 3.0 mL/min sample possessed a core diameter

of 5.7 ± 1.3 nm, the 6.0 mL/min sample had a core diameter of 3.5 ± 0.8 nm, and the 9.0 mL/min sample had a core diameter of 2.7 ± 0.7 nm. The difference between the particle solutions was obvious by UV-vis absorbance spectroscopy (Figure 5.5.A). The nanoparticle solutions could easily be deposited in small volumes from the reactor outlet port onto a prepared substrate (Figure 5.5.B). TEM micrographs and size distributions are given for the 3.0 mL/min and 6.0 mL/min AuNP samples (Figure 5.5.C-F). The three nanoparticle samples (5.0 mL of each) were prepared in less than fifteen minutes, indicating that nanoparticle samples with discrete properties can rapidly be prepared using the flow reactor.

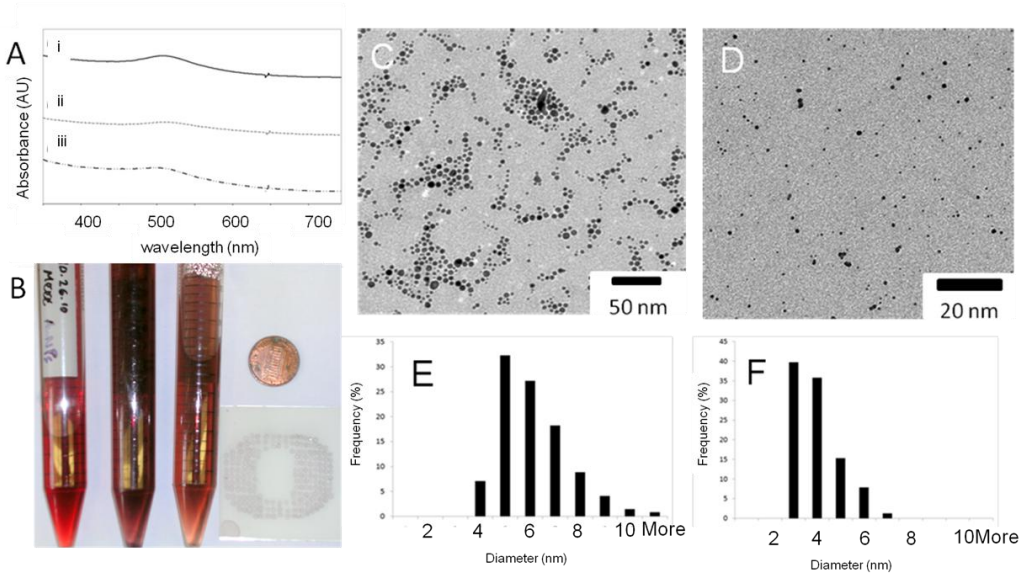

Figure 5.5: The capillary flow reactor can be used to synthesize different sizes of AuNPs from a single set of reagent stock solutions, providing an opportunity to rapidly generate and characterize AuNP products with discrete properties. By varying the flow rate of the reaction from 3.0 to 9.0 mL/min and using a set L:Au:R of 1:5:1, AuNPs from 2.5 to 7.0 nm in diameter can be synthesized. (A) UV-vis absorbance data collected in situ for AuNP samples prepared at different flow rates: i.-iii. = 3.0-9.0 mL/min. (B) AuNP solutions prepared by this method (L-R: 3.0 mL/min, 6.0 mL/min, and 9.0 mL/min), and dropcast onto a TLC plate. (C,E) TEM data for the 3.0 mL/min AuNP sample. (D,F) TEM data for the 6.0 mL/min sample.

We have successfully demonstrated that this simple flow reactor setup can be used to generate nanoparticles with discrete properties rapidly. The ability to rapidly synthesize and analyze nanoparticle samples is becoming increasingly important in approaches for the investigation of nanoparticle structure-function relationships and the optimization of nanoparticle synthetic methods.[39-41] Combinatorial chemistry approaches are becoming increasingly utilized in both these areas, and require the rapid synthesis of

nanomaterial samples with discrete properties.[39-41] The ability to analyze nanoparticle properties in real time, as an integral portion of the synthetic platform, can be of further benefit in these types of studies. Flow syntheses of the type described here provide examples of how the fluidic synthesis of nanomaterials may be used to quickly generate and assess the properties of functionalized nanomaterials, or rapidly assay reagent conditions to achieve a specific synthetic target.

Conclusions

In this chapter, we have demonstrated that a simple capillary flow reactor can serve as an effective platform for the synthesis of thiol-stabilized AuNPs while simultaneously providing *in situ* quantitative characterization of their dimensions. The flow reactor provides a high-throughput platform for the synthesis of thiol-protected AuNPs (less than one minute for a complete reaction), while providing effective size control *via* a number of reactions parameters. The surface chemistry of thiol-stabilized AuNPs produced in a flow reactor were investigated for the first time, and it was shown that the thiolate ligand shell forms rapidly on the AuNP surface within the flow reactor, producing ligand-stabilized AuNPs within 30 s of residence time. The reactor incorporates multiple analytical techniques simultaneously (e.g.- UV-vis absorbance spectroscopy and SAXS) that permit an opportunity to quantitatively determine nanoparticle size during synthesis. The success of this relatively simple setup in the rapid synthesis and analysis of AuNPs suggests that flow reactors may provide a unique platform to develop new strategies for investigations of the link between nanoparticle structure and performance properties.

CHAPTER VI

MONITORING GOLD NANOPARTICLE GROWTH KINETICS IN REAL TIME USING SIMULTANEOUS SAXS AND UV-VIS ANALYSIS

Note: In this chapter, we present a demonstration of how the capillary flow reactor described in the previous chapter can be used to monitor the growth of gold nanoparticles in real-time using SAXS. We also present a short review of three of the primary proposed models of gold nanoparticle growth mechanisms and describe how SAXS data can be used to distinguish between them. The kinetic analysis of nanoparticle growth described in this chapter was a collaborative effort between the author, Pat Haben, and Ed Elliot of the Hutchison laboratory. The author helped develop the AuNP synthesis examined in the chapter, and identified and demonstrated the use of the quantitative analysis by UV-vis and SAXS used to determine AuNP concentration during synthesis. The author also provides the review of the nanoparticle growth mechanisms and a demonstration of how SAXS data can be used to distinguish between them. Pat Haben developed the final observation cell (based on a prototype designed by Lallie McKenzie) contained within the flow reactor and led the study of nanoparticle growth by SAXS, which the author and Ed Elliot also participated in. We would like to thank Steve

Kevan, Alex Hexamer, and beam line scientists at the Advanced Light Source (Berkeley National Labs) for their assistance with SAXS analysis of gold nanoparticles in the flow reactor.

Introduction

The mechanistic details of metal nanoparticle growth during synthesis remain obscure for many synthetic systems.[1-5] Understanding the details of functionalized nanomaterial formation permits new developments in improved property control, synthetic efficiency, and the opportunity to rationally design alternative synthetic approaches or purification strategies.[1-5] Because of the challenges associated with monitoring nanoparticle growth, for many of the most ubiquitous synthetic methods, even general mechanistic information such as rate constants, basic reaction orders, the identity of important intermediate species, and the distribution of products remain entirely undetermined. [2,3,4,6-13] Currently, mechanistic investigations of nanomaterials growth are focused on two aspects of the synthetic reaction: monitoring the kinetics of nanoparticle formation,[1,3-10] and identifying key chemical species present in the reaction pathway.[2,10-13]

The stages of gold nanoparticle (AuNP) growth are generally defined by analogy to La Mer's description of colloidal sulfur formation, dividing metal particle growth into three stages: nucleation (the formation of new nanoparticles),[α] monomer addition to the nuclei (growth), and passivation (the formation of a ligand shell on the AuNP surface, preventing further monomer addition). [15-19] Application of the principles of this model to a variety of synthetic systems has led to significant gains in size, shape, and dispersity

control in the past, but synthetic control of these physical properties is still less effective than many researchers might desire.[11,21,22] Therefore, developing much more detailed and specific mechanistic models are necessary in order to design syntheses that allow for precise control over NP physical properties.[10,17-22] Already, it has been shown that a number of syntheses that have been in use for decades possess important mechanistic features that the traditional model of AuNP formation does not account for.[2,20] These include the merger of nuclei to generate larger AuNPs (coalescence),[1,3-5] and the evolution of AuNP nuclei from gold nanowire-like species.[6,20]

The ability to analyze the formation kinetics of gold nanoparticles is a significant challenge in refining the classic model of gold nanoparticle growth.[3-5,23,24] Traditionally, real-time quantitative kinetic investigations of gold nanoparticle growth have been hamstrung by a lack of appropriate monitoring techniques. [3-5,23,24] *Ex situ* analysis methods, such as TEM, are poorly suited for following the growth of AuNPs, as sample preparation methods may introduce artifacts that will alter the perceived size of the AuNPs under analysis.[23,25,26] Recently, various new *in situ* methods for nanoparticle size determinations have begun to yield significant new mechanistic insights into metal nanoparticle growth.[1-6,26-37] Liquid cell microscopy techniques for the analysis of single nanoparticle growth in real time have been developed, but this type of kinetic investigation requires extensive analysis times, and sophisticated data analysis to generate statistically relevant conclusions.[23,24] In contrast, the use of scattering analyses, particularly small-angle x-ray scattering (SAXS), has provided an opportunity to quantitatively analyze AuNP growth for entire samples with sub-second time resolution,

while rapidly providing information on core diameter, size distribution, and concentration.[1-7,25,26,32-34] The application of SAXS monitoring of AuNP growth has already been realized for several AuNP growth reactions,[1-7,25,32-34] however, the syntheses of more complex functionalized AuNPs (e.g.-thiol-protected AuNPs) have not yet been investigated using *in situ* methods.

The implementation of flow reactors for nanomaterials synthesis provides a new opportunity analyze the size and shape of nanomaterials at various residence (reaction) times using quantitative in situ analysis methods.[10] We recently developed a simple capillary flow reactor that can be used for the synthesis of thiol-protected gold nanoparticles, and allows for the quantitative determination of nanoparticle size by simultaneous UV-vis absorption spectroscopy and SAXS analysis at different reaction times (see Chapter V). The continuous flow of reaction solution through the reactor system means that SAXS data collection can be performed for extended periods, while the versatility of the flow reactor platforms means that any reaction time greater than one second can be analyzed by two instrumental techniques simultaneously, and the synthesized material can easily be collected at the conclusion of the run for further analysis.[26] A similar flow reactor setup has recently been employed to quantitatively analyze pre-prepared AuNPs by simultaneously SAXS and UV-vis absorbance analysis, but has not previously been employed in kinetic investigations of AuNP growth.[26]

In this chapter, we report the adaptation of the capillary flow reactor described in Chapter V for the real-time quantitative determination of gold nanoparticle size as a function of time during synthesis. We examined the growth of thiol-stabilized AuNPs

under various synthetically relevant reaction conditions using simultaneous UV-vis spectroscopy and SAXS analysis. We demonstrate that the growth rate of the nanoparticle core varies with gold concentration. By examining the concentration of gold nanoparticles over time, we also show that a coalescence mechanism is involved in growth of gold nanoparticles produced by this synthetic method. The reactor used in this study provides a simple and adaptable investigatory platform that may be applicable for future studies of the kinetics and mechanism of many nanoparticle syntheses.

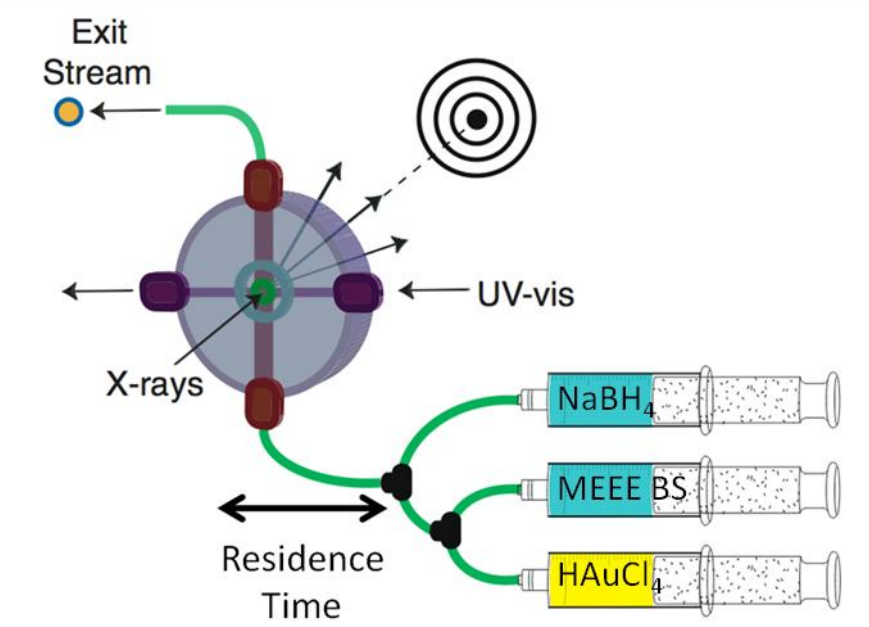

Figure 6.1: The reactor platform used for the mechanistic analysis of gold nanoparticle growth consists of three syringe pumps connected by t-mixers to an observation cell that allows for orthogonal UV-vis and SAXS analysis of the nanoparticle solution. Gold tetracholoaruate and the Bunte salt (MEEE BS) are allowed to mix together prior to the addition of sodium borohydride, which initiates AuNP formation. The residence time observed can be varied by changing the length of tubing between the final mixer and the observation cell.

Experimental

Materials and Reagents. Gold tetrachloroaurate trihydrate (Alfa Aesar), sodium borohydride (Aldrich), sodium hydroxide (Aldrich), and 2-[2-(2-chloro)-ethoxyethoxyethanol] (Aldrich), were obtained from their suppliers and used as received. The synthesis of the mercapto-ethoxy-ethoxyethanol Bunte salt analog (MEEE BS) was performed as previously described.[38] The capillary flow reactor was constructed from Teflon tubing (ID 760 μm, IDEX Health and Science 1520 XL) and t-mixers (Upchurch) that are commercially available. The interior diameter in the flow channel of the observation cell was slightly larger than that of the Teflon tubing (1.0 mm versus 760 μm). The flow reactor was driven by three Kloehn syringe pumps (Kloehn Versa 6 P/N, 54022), equipped with two 10.0 mL syringes, and one 25.0 mL syringe, respectively. The pumps were run using the programming software included with the Kloehn pumps. Stovall Bubble Traps were used in order to eliminate the likely formation of bubbles in the observation cell during analysis. The observation cell used in the experiments was configured as described in Figure 1, and based on the design reported by McKenzie, with the SAXS and UV-vis absorbance analyses taken orthogonally to one another.[26] The path length for SAXS measurements in the observation cell was 750 μm. The observation cell included a port for UV-vis fiber optics, and recessed mica windows to allow for SAXS analysis. Absorbance data was acquired using an Ocean Optics USB 400 detector with an Ocean Optics DTS-Mini-20 Halogen/Deuterium lamp light source.

Reactor Assembly and Operation. The reactor consists of three computer-operated syringe pumps (Figure 6.1) connected by Teflon tubing with a 750 μm inner diameter to two T-mixers (1000 μm id). The design of the capillary flow reactor has been described previously,[26] but briefly, three syringe pumps each contain one reagent stream (gold tetracholoraurate$_{(aq)}$, MEEE BS$_{(aq)}$, and sodium borohydride in basic solution, respectively). The gold reagent stream mixes with the ligand precursor in the first T, and these reagents coexist in a single stream for five seconds prior to mixing with the sodium borohydride in the second T-junction, which initiates AuNP synthesis. The observation cell is then positioned a set distance from the second t-mixer, in order to observe specific residence times. The reactor setup and the general synthetic scheme are shown in Figure 6.1. We analyzed two different synthetic conditions by SAXS and UV-vis to develop gold nanoparticle growth curves. The molar ratios used in each case were 1:2:2 Bunte salt:gold(III):borohydride and 1:5:2 Bunte salt:gold(III):borohydride. The particle size was determined at seven different residence times for each set of conditions- 3s, 5s, 10s, 15s, 30s, 45s, and 60s. For both reaction conditions, each residence time was observed three times, and the system was flushed three times with water in between each acquisition.

UV-vis Absorption Analysis of Gold Nanoparticle Growth in Real Time. UV-vis absorption spectroscopy can potentially be used as both a qualitative and quantitative analysis technique to establish AuNP core diameter. In addition to collecting the full absorbance spectrum (300-800 nm) of the AuNP solutions at every residence time, we used a model for determining AuNP size from UV-vis absorption data that ratios the

absorbance at the SPR maximum absorption to the absorbance at 450 nm.[39,40] This method purports to provide accurate AuNP size determinations at a given residence time, but we found the model to be less accurate for AuNPs with core diameters less than 5.0 nm, and provides no data on AuNP dispersity at a given time. Therefore, we used UV-vis analysis as a qualitative analytical technique to provide rough AuNP sizes at different residence times, and the data was then collaborated by SAXS analysis.

SAXS analysis of AuNP Populations at Specific Residence Times. SAXS analysis of the nanoparticle populations analyzed at each residence time provides quantitative size determinations for the trends indicated by the UV-vis absorbance data.[1-7,26] Small angle X-ray scattering provides a very sensitive quantitative method for determining AuNP mean size and dispersity at a given residence time.[41-44] SAXS measurements were performed at Beam Line 7.3.3 at the Advanced Light Source (ALS, Lawrence Berkeley National Labs, Berkeley, CA). The X-ray source (mediated by a Mo/BC double multilayer monochromator) provides monochromatic X-rays at 10 keV, and the spot size at the sample is 1 mm horizontal × 0.24 mm vertical. The scattering intensity was recorded using Pegasus CCD detectors. The total q range provided by the detector system is between 0.004 and 8.7 A^{-1}. The total acquisition time for each SAXS measurement was approximately 5 min. Several measurements were taken for each sample and averaged to determine scattering intensity. The observed scattering intensities were corrected by subtraction of the background (scattering of the solvent-filled observation cell).[26]

Modeling and Analysis of SAXS Data. A full treatment of the method employed for analysis of the AuNP sample populations has been described previously.[26] Briefly, solutions of gold ions and small atomic gold species scatter X-rays minimally, so after proper background subtraction, the scattering signal will only result from the growing gold nanoparticles. The scattering intensity can be related to the size distribution of the gold nanoparticles using the following equation:

$$I(q)= (\Delta\rho)^2 (n\int f(r)\, V(r)^2\, P(q,r)\, dr) \qquad (1)^{41\text{-}44}$$

Where V(r) and P(q,r) are the volume and form factor for a sphere of radius r, while f(r) is the size distribution of the particle sample, which is obtained by fitting the SAXS data to a Gaussian distribution. $\Delta\rho$ is the difference in electron density between the particle material (gold) and the solvent (water). SAXS data were processed using IGOR Pro v6.02A software. SAXS data averaging, background subtraction, and conversion from 2D CCD images to 1D plots were performed using the Nika v1.17 macro. Application of models to the SAXS plots was performed using the Irena v2.27 macro. The agreement between the calculated patterns and the experimental patterns are excellent, as is the agreement between the sizes observed in each case and the sizes determined by UV-vis data. The relative concentrations of gold nanoparticle samples at each time can be related to the intensity of the scattering at q=0 by equation 6.2.

$$I(0) = N(V)^2\Delta\rho^2 \qquad (2)^{41\text{-}44}$$

In this equation, N is the number of scatterers present in the volume of the sample analyzed at any given time. By determining N, and dividing by the volume of the solution

element analyzed, the relative concentration of AuNPs at any residence time can be determined.

Results and Discussion

The synthesis of gold nanoparticles in a flow reactor with a built in observation cell provides a unique opportunity to monitor the kinetics of gold nanoparticle growth as they are synthesized. Using the capillary flow reactor described in detail in Chapter V, we determined the gold nanoparticle core diameter at various reaction times (between 3s and 60s) using SAXS analysis paired with simultaneous UV-vis absorbance spectroscopy. We analyzed the growth of gold nanoparticles at two different sets of reaction conditions: 1:5:2 L:Au:BH_4^- and 1:2:2 L:Au: BH_4^- (molar ratios). We plotted the gold nanoparticle diameter versus time, and determined the dependence of the growth rate on the gold concentration. From the SAXS data, we also developed plots of core diameter dispersity and concentration versus time, from which, we have been able to develop some basic conclusions about the mechanism by which gold nanoparticles form in this synthesis.

UV-vis Monitoring of AuNP Diameter Versus Time. In order to qualitatively monitor the evolution of particle size between 3s and 60s, we used UV-vis absorption spectroscopy to track the evolution of the AuNP core (Figure 6.2). UV-vis analysis reveals that the core diameter increases significantly in the 60s of residence time for the 1:5:2 L:Au:BH_4^- conditions, as evidenced by the significant increase in intensity and red-shift of the surface plasmon absorbance (SPR), suggesting that the AuNPs have achieved a core diameter greater than 5.0 nm by the end of this time period. The absolute change in

size under lower gold concentration conditions is less dramatic, as the change in the absorbance data is much more subtle over the same time period, and the final particle size appears to be less than 3.0 nm, as the plasmon absorbance is still very broad and weak at this residence time.

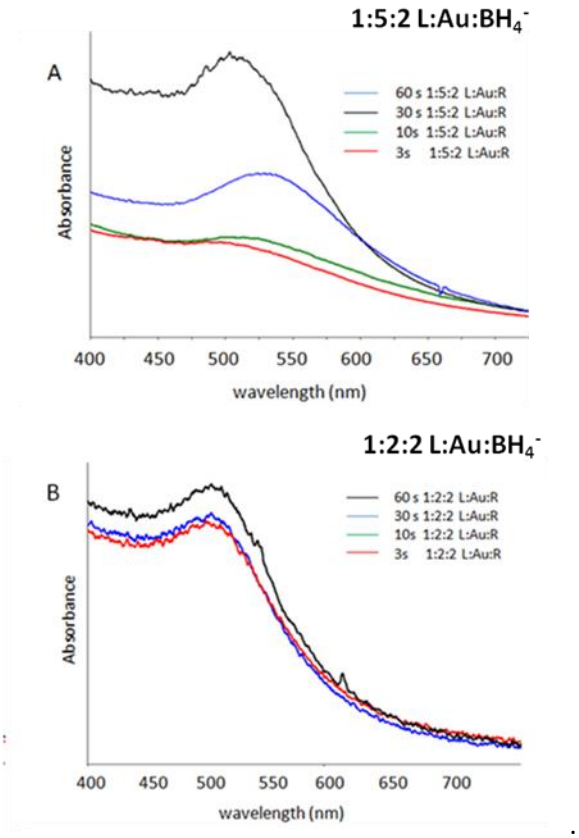

Figure 6.2: The UV-vis absorbance data for the nanoparticle reaction times observed in the reactor under different synthetic reaction conditions are shown here. The UV-vis data for residence times of 3s, 10s, 30s, and 60s are given. (A) shows these data for the 1:5:2 L:Au:BH_4^- reaction conditions and (B) provides the same data for the 1:2:2 L:Au:BH_4^- reaction conditions. The higher gold concentration (A) shows a quite rapid growth over the first 60s, but the growth over the same time period for the lower gold concentration is much slower.

SAXS Analysis of Core Growth over Time. SAXS analysis of the same residence times provides a quantitative determination of AuNP core diameter over time. SAXS analysis reveals that the AuNPs prepared under 1:5:2 L:Au:BH_4^- conditions grow from a size of approximately 3.1 ± 1.3 nm (3s) to 5.7 ± 1.1 nm by 60s. At the lower gold concentration (1:2:2 L:Au:R) the AuNPs grow from 2.5 ± 1.1 nm to 3.3 ± 1.2 nm (Figure 4.3). Thus, the SAXS data supports the UV-vis absorbance data taken at the same residence times, but allows for a quantitative evaluation of the same phenomenon.

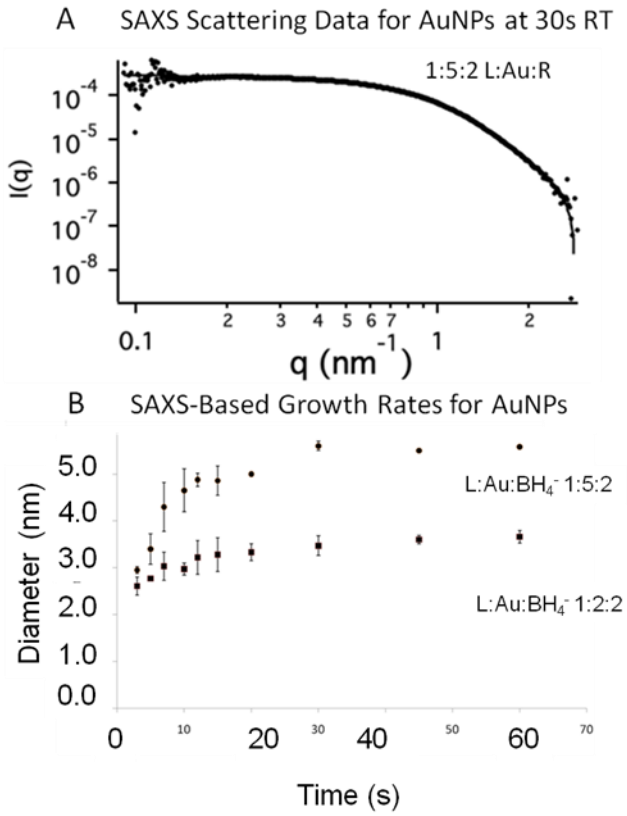

Figure 6.3: SAXS data obtained for gold nanoparticle growth in the flow reactor reveals that the rate of nanoparticle formation depends on the concentration of gold used in the reaction mixture. (A) A representative SAXS pattern is given here, corresponding to 30s residence time under the reaction conditions 1:5:2 L:Au:BH_4^-. Modeling of the data indicates that the AuNP population at this residence time has a mean diameter of 5.9 ± 1.7 nm. (B) Plotting the mean core diameter (SAXS) versus time for both reaction conditions as a function of reaction time reveals that the growth rate of AuNPs depends significantly on the concentration gold used in the synthesis. Under the 1:5:2 L:Au BH_4^- conditions, AuNP growth occurs much more rapidly then under the 1:2:2 conditions, and achieves a larger final core diameter.

An interesting feature of this data is the very similar sizes of the AuNPs observed at 3s, regardless of the reaction conditions, with the AuNPs at this time, under both reaction conditions being nearly 3.0 nm in diameter. This *implies* that the nuclei size is

quite comparable under both reaction conditions, suggesting that the size of the initial particle formed in this synthetic reaction may be independent of the gold concentration. Interestingly, along with varying the concentration of gold, the L:Au ratio used in the synthesis has been altered, yet the same nuclei size apparently results (although as previously stated, we lack the time resolution to observe the nuclei size directly). This may indicate that the L:Au ratio has no effect on the size of the nuclei produced in the synthesis. As the L:Au ratio is one of the most commonly used synthetic reaction parameters for controlling the size of AuNPs during synthesis, this potentially indicates that size control provided by the L:Au ratio is effected during the growth and passivation phases of AuNP formation.[10,16] The nucleation phase of the reaction is worthy of much more detailed study, though the current capillary flow reactor setup is ill-suited to the analysis of sub-1 s reaction times.

The SAXS data collected under both reaction conditions can be fit by a simple exponential function over this period of nanoparticle growth (Figure 6.3 B), but the growth rate is much more rapid at the higher gold concentration. The difference in growth rate between the two curves clearly show that the growth rate of gold nanoparticles in this synthetic system depends on the concentration of gold in the reaction mixture, and therefore, gold must participate in (or prior to) the rate-limiting step in the reaction pathway. Previous AuNP syntheses that are initiated by borohydride reduction have previously been shown to possess similar exponential growth profiles.[33] The full extent of the growth curve is not visible in this study, as we are unable to resolve particle sizes at reaction times of less than one second. This means that while the growth and

passivation portions of nanoparticle formation are clearly observed in this study, nucleation (which in the synthesis of gold nanoparticles has been shown to occur on a millisecond time scale), cannot be observed using the existing setup.[1] The shape of the growth curve does not immediately suggest the mechanism by which particle growth occurs, but there are three likely pathways by which gold nanoparticle growth has been proposed to occur: monomer-diffusion,[11-15,33] coalescence,[1,3,5] and Ostwald ripening.[4] Further information can be extracted from the X-Ray scattering data that provides a method to differentiate between the three mechanisms.[33]

Mechanisms of Gold Nanoparticle Growth. There are typically three mechanistic models invoked to describe the "growth" phase of gold nanoparticle formation: monomer diffusion, coalescence, and Ostwald ripening. Monomer diffusion involves the diffusion of gold atoms, or sub-nanometer gold clusters through solution to specific addition sites on the developing nanoparticle surface.[33] Coalescence involves the merging of multiple nuclei to form new polycrystalline AuNPs.[1] Ostwald ripening is typically thought to be restricted to the ripening of AuNPs that occurs following the initial passivation of AuNP growth, but is manifested by the transfer of small amounts of gold from smaller gold nanoparticles to larger gold nanoparticles, and results in size-focusing in the particle population (the decrease in core diameter dispersity).[4] Schematic representations of these growth mechanisms are shown in Figure 6.4, along with the characteristic data that can be gleaned from SAXS analysis that distinguish the three mechanisms.

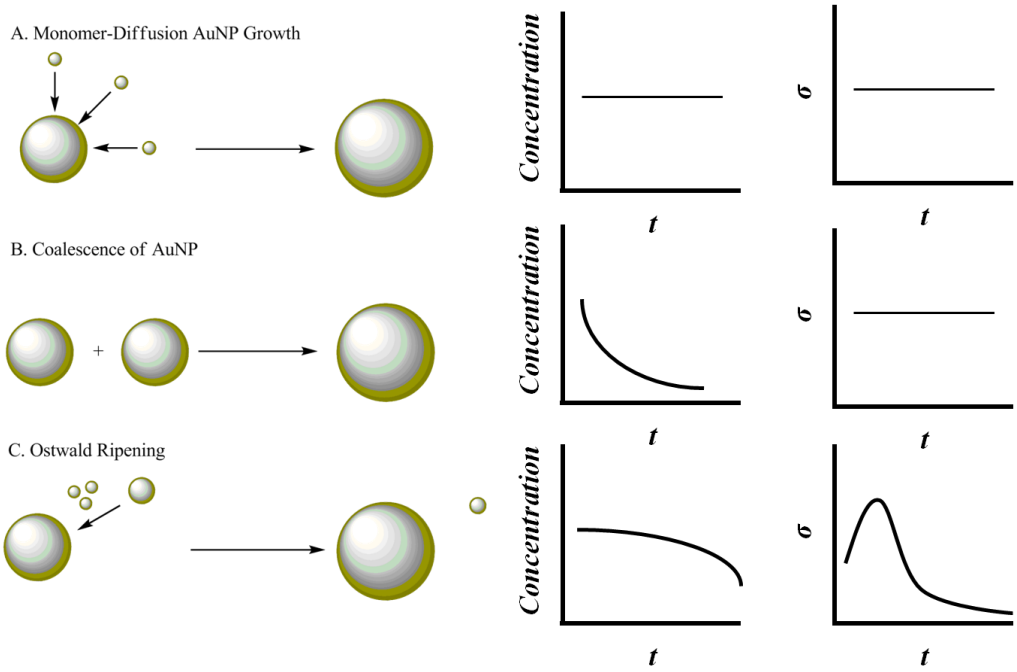

Figure 6.4: Three mechanisms of gold nanoparticle formation are commonly proposed. (A) Monomer-diffusion is the classical model for nanoparticle growth, involving the diffusion of small gold species to available sites on the nanoparticle surface. In this mechanism, the AuNP concentration remains constant over the course of growth, as does the dispersity of the AuNP core diameter over time. (B) In the coalescence model, gold nanoparticle nuclei merge to form new poly-crystalline AuNPs, causing a drop in particle concentration over time, but the dispersity remains relatively constant over the reaction time. (C) Ostwald ripening is thought to occur primarily at longer times, and involves the transfer of small amounts of matter from small particles to large particles. This means the concentration of the AuNPs remains relatively constant until longer times, when the smaller particles have been completely consumed. The dispersity of the sample initially increases, but is then minimized at longer times, once the small particles have been consumed. σ (standard deviation) represents dispersity in the graphs shown.

The three common mechanisms can be readily distinguished by examining the behavior of particle concentration and dispersity with time, and both pieces of data can be readily determined from the SAXS analysis. Modeling of the SAXS data provides information on particle dispersity (along with the mean core diameter) at various

residence times, and the scattering intensity can be related to the gold nanoparticle concentration. These two pieces of data can be used to distinguish between the three models of nanoparticle growth, as two of the mechanisms involve the disappearance of nucleated AuNPs in the formation of larger particles.

In monomer diffusion, small gold species are added to existing nuclei with the rate controlled by the diffusion of the monomer, and the availability of suitable addition sites on the AuNP surface.[11-15,33] This model traditionally assumes that nanoparticle nucleation is temporally separated from the growth of the cores, so no new nuclei form once the growth phase has begun. As a consequence, the concentration of AuNPs remains constant throughout the entire reaction. The dispersity should also remain constant throughout the course of the reaction, reflecting the size distribution of the initial nuclei, assuming no size-dependency in monomer addition. Monomer diffusion based-growth has been shown to generally occur on a reaction time scale of seconds to minutes, though the rate may be influenced by the nature of the particle ligand shell.[33] Monomer diffusion is the classical model for metal nanoparticle growth, invoked by Frens and Sugimoto to describe the process by which nanoparticle nuclei grow.[11-15] Very recently, however, AuNP growth has been proposed to occur by another method- coalescence of the nuclei.

In contrast to diffusion-limited growth, coalescence requires a reduction in nanoparticle concentration as existing nuclei merge, forming larger, polycrystalline AuNPs.[1,3-5] Coalescence mechanisms have increasingly been invoked in kinetic studies of gold nanoparticle growth in recent years, for AuNP formation initiated by both weak (ascorbic acid, citrate) and strong (sodium borohydride) reductants.[1,3-5] The dispersity of

particles growing by this mechanism should remain essentially constant over the course of the reaction, though this assumes that small-small or small-large particle coalescence is not preferred.[1] Analysis of particle concentration versus time should show a substantial decrease in AuNP concentration over time, and the larger the final particle size, the more significant the drop in AuNP concentration will be. Thus, AuNP growth *via* coalescence should be distinguishable from diffusion-limited growth by examining the change in AuNP concentration over time. It has also been proposed that AuNPs that grow by coalescence will necessarily lead to polycrystalline, twinned AuNPs, while AuNPs that grow by monomer diffusion will be single-crystalline, but TEM analysis of AuNPs has not been shown to provide an unambiguous determination of the growth mechanism.

The final proposed growth mechanism, Ostwald ripening involves the transfer of mass from small AuNPs to large AuNPs.[4] This mechanism is primarily invoked to explain particle size focusing (reducing dispersity while trending towards larger core diameters) that occurs in nanoparticle populations over the course of hours or days. Ostwald ripening requires that the particle concentration remains essentially constant throughout the reaction, until the complete consumption of the smaller AuNPs, at which time, the concentration begins to decrease (Figure 6.4 C).[4] The dispersity of the AuNPs will initially increase, as the magnitude of the bimodality in the AuNP population increases (small AuNPs get smaller, while large AuNPs get larger), but will eventually be minimized as the smaller AuNPs are fully consumed. Generally, Ostwald ripening mechanisms are invoked only at extremely long reaction times, generally to explain the

further growth of AuNPs after passivation of nanoparticle growth is considered to be complete.[4]

Each of the three mechanisms presented here possess characteristic concentration and dispersity behaviors that permit them to be distinguished by careful analysis of the SAXS data (Figure 4.6). While Ostwald ripening can almost be ruled out immediately, because mass transfer on this scale generally requires much longer times (hours or days), we must carefully examine the SAXS data to distinguish between diffusion-limited growth and coalescence, while remembering that these models represent limiting cases when describing the growth of gold nanoparticles. In all likelihood, the growth of AuNPs may proceed by a process that invokes elements of both mechanisms, and interpretation is further complicated by the fact that nucleation and growth are assumed to be temporally separate, but in practice, these two processes may actually occur concurrently to some extent.

Concentration of AuNPs and Dispersity of AuNPs over Time in the Fluidic Reaction. Sufficient information can be obtained from the SAXS analysis of the nanoparticle growth reaction so that the concentration of nanoparticles over time and the dispersity over time can be determined. These pieces of data provide the fundamental basis for determining between several likely mechanisms of nanoparticle growth. By evaluating equation (6.2) at q=0, the relative number of gold nanoparticles scattering at each time point can be determined.[1,33] The absolute concentration cannot be determined from the SAXS data alone, due to nature of the analysis and the detector employed.[α] However, the relative concentration of scatterers can be obtained, and the concentration

of AuNPs at 60s can be determined from the UV-vis data. Scaling the relative concentration obtained from the SAXS data by the concentration obtained *via* UV-Vis absorbance data provides a means to calculate AuNP concentration quantitatively at each time point.[26,33,40] Figure 6.5 presents the concentration versus time data for the L:Au:BH_4^- 1:2:2 run. This data reveals that the concentration of AuNPs decreases slowly over time. The concentration of AuNPs over the course of the entire reaction lies in the nano molar range (1.4 x10^{-7} M at 3s), and decreases by approximately a factor of five over 60s of reaction time.

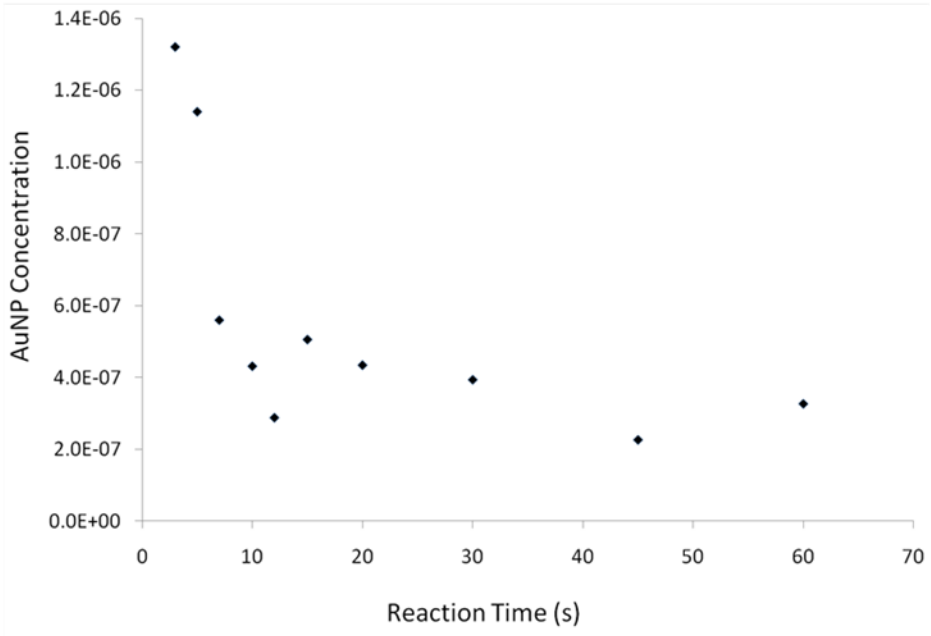

Figure 6.5: Determining how gold nanoparticle concentration varies with reaction time provides a means to make initial conclusions about the mechanism of nanoparticle growth. The SAXS data indicates that AuNP concentration versus time decreases rapidly, decreasing to approximately one-fifth of the initial concentration over the course of the AuNP growth. This rapid decrease in AuNP concentration is consistent with core growth by a coalescence mechanism.

The decrease in concentration observed in this study is consistent with the approximate loss of nanoparticle concentration that would occur during growth by coalescence. Given that the initial diameter observed in the 1:2:2 L:Au:BH_4^- growth study is 2.5 nm, and the final diameter (60 s) is 3.3 nm, we would expect that concentration would decrease at least three fold during this time period (based on the initial and final volumes of the AuNPs), if the growth proceeded by coalescence. Since the AuNP concentration decreases nearly five-fold over the course of the reaction, we conclude, at this point, that AuNP growth occurs primarily by a coalescence mechanism. It should be noted however, that deposition of gold on the reactor walls was observed during the course of the analysis. ICP and UV-vis analysis were used to corroborate the concentration of AuNPs present after 60 s of residence time, and show that the amount of gold lost via adsorption to the reactor is not significant (5-10%), compared to the concentration drop observed by SAXS analysis over the course of the reaction. Therefore, the data strongly indicate that a coalescence mechanism plays a role in particle growth in this size range. SAXS analysis of concentration for the 1:5:2 L:Au:BH_4^- reaction conditions could not be completed because these data were collected during different visits to the ALS and taken on different detectors and with the X-ray source providing different intensity behaviors from trip to trip.

The dispersity (σ) of core diameter over time varies extensively over the course of the reaction (Figure 6.6), but fluctuates around an approximate value of 50% of the mean core diameter. At early times, the dispersity is large, approximately 60-70% of the mean

core diameter. Over time, the dispersity decreases, but levels off below below 50% of d_{core}. The relatively large dispersity of the core diameter over time is somewhat surprising as MEEE-AuNP samples synthesized under similar conditions typically possess relatively low dispersities, as determined by TEM (~25%, see Chapter V). It may be valuable to refine the synthetic conditions used in this experiment to minimize dispersity of the AuNP samples at different residence times, which would, in turn lead to more accurate determinations of AuNP core size at various times. The minor decrease in the overall dispersity of the particle populations observed indicates that growth is not proceeding by a ripening process, as the highest dispersities are observed at early times. This behavior of core diameter dispersity over time would be consistent with either the diffusion-limited growth model or coalescence of the AuNP nuclei to form polycrystalline AuNPs.

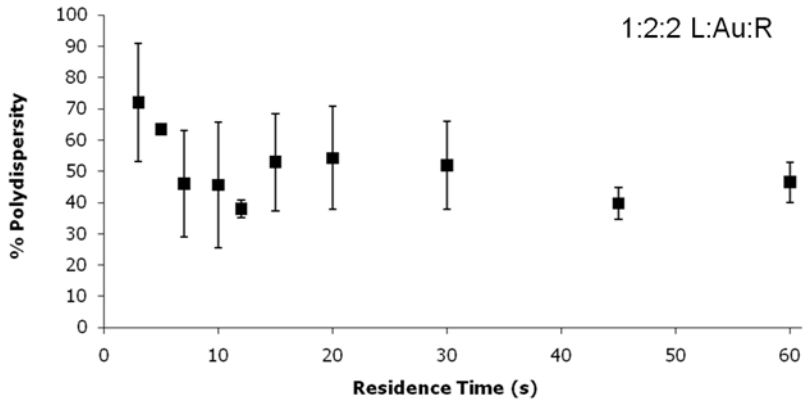

Figure 6.6: The AuNP dispersity over time under the 1:2:2 L:Au:BH_4^- reaction conditions varies, but fluctuates around a relatively constant value of approximately 50% of the mean core diameter. This data indicates that that AuNP sample dispersity does not vary in a predictable manner over the course of the entire reaction. This pattern of dispersity over time is consistent with either a diffusion-limited growth model or coalescence.

Based on the particle concentration data over time and the dispersity over time (as determined by SAXS), it is reasonable to conclude that AuNP growth likely proceeds at least partially by a coalescence mechanism, under the reaction conditions observed. Recent *in situ* observations of AuNP growth have indicated that the mechanism of AuNP growth may be size-dependent, with the coalescence of particles favored at certain sizes, and growth by monomer diffusion favored in other size regimes. Therefore, determining the concentration versus time behavior for AuNP growth under the 1:5:2 reaction conditions would be valuable to see if growth by coalescence is indicated in this size regime as well.

Conclusions

In this study, we have demonstrated how a simple capillary flow reactor can be used to permit quantitative real-time monitoring of AuNP growth during synthesis, and how this can be exploited for the kinetic analysis of AuNP growth. We utilized this reactor to perform the first real-time quantitative kinetic analysis of the growth of thiolate-protected AuNPs, and compared the growth rates under different reaction conditions. We have shown that the growth rate of the AuNPs depends on the concentration of gold precursor used in the synthetic reaction. We have also shown that the borohydride-mediated growth of AuNPs in this synthesis proceeds, at least in part, by a coalescence growth mechanism. The capillary flow reactor platform described here can

potentially serve as a general platform for the kinetic analysis of different nanoparticle synthetic systems with minimal modifications.

Notes:

α- The term nucleation has specific connotations with respect to the LaMer model of nanoparticle growth. However, when the term "nucleation" is used in this chapter, it is used simply to mean the formation of a gold nanoparticle that is large enough to be detected by SAXS analysis. We have shown that 11-atom gold clusters (0.8 nm diameter) can successfully be identified using our existing setup. As we cannot observe the earliest growth times (< 2s) using the capillary flow reactor, we cannot yet speculate on the very early processes of NP formation and growth.

β-Because of the nature of the CCD detectors employed in the SAXS analysis, every photon registered by the detector does not necessarily reflect all the scattering events occurring in solution. Instead, the relative number of scatterers in solution at a given reaction time is generally determined from the intensity measurement at q=0. Therefore, SAXS data is usually used to determine relative concentration.

CHAPTER VII

CONCLUDING SUMMARY

This dissertation describes the development of a synthetic strategy for thiol-protected gold nanoparticles that uses alkyl thiosulfates (Bunte salts) as ligand precursors to access a wide range of AuNP sizes. Beginning with the initial demonstration of the Bunte salt ligand precursors' synthetic utility, we expanded this study to an investigation of the chemistry of Bunte salt-thiolate conversion at gold nanoparticle surfaces. We demonstrated that this conversion proceeds through a weakly-passivated intermediate gold nanoparticle species, which permits further growth of the initial nanoparticle, allowing synthetic access to larger AuNPs than are available in direct synthesis methods using thiols. We then described how the initial synthesis could be adapted for use in two flow reactors, including both microfluidic devices and capillary flow reactors. The adaptation of the synthesis for use in flow reactors opens up opportunities for the high-throughput synthesis of functionalized AuNPs while allowing for real-time monitoring of particle properties *in situ*. In addition, the use of the capillary flow reactor provided an opportunity to monitor AuNP growth kinetics in real time, leading to further insights into the formation of AuNPs *via* this synthetic method.

In Chapter II, we describe the development of a direct synthesis for thiol-protected AuNPs using Bunte salts as ligand precursors. The use of Bunte salts permits the synthesis of AuNPs with core diameters between 20.0 and 1.5 nm in diameter. The range of AuNP sizes that can be synthesized by this method is much greater than the size of AuNPs available in the direct synthesis of AuNPs using thiols as ligands (0.8-4.0 nm). Characterization of the surface chemistry of these AuNPs indicates that the AuNPs produced by this synthesis are protected by thiolate ligands, indicating successful conversion of the ligand precursor to the ligand during synthesis.

In Chapter III, we explored the effect of the synthetic conditions on the ligand shell composition (Bunte salt versus thiolate) of AuNPs produced in this synthesis. We found that the ligand shell composition was strongly influenced by the sodium borohydride:gold ratio used in the synthesis for AuNPs with core diameters greater than 4.0 nm. In this size regime, the formation of thiolate-protected AuNPs proceeds through an intermediate AuNP species that is protected by adsorbed Bunte salts. This intermediate species can be isolated from the reaction mixture under appropriate conditions. In contrast, for small AuNPs (core diameters less than 4.0 nm), this intermediate species could not be isolated. In these cases, thiolate-protected gold nanoparticles form rapidly, regardless of the reaction conditions. The difference in reactivity between the two AuNP sizes may be related to differences in surface charge and structure, as AuNPs with core diameters < 4.0 nm have been shown to be effective catalysts in a number of chemical reactions. The data presented in this chapter also explicitly demonstrate that during the synthesis described in Chapter II, the Bunte salt

ligand precursor is converted to the corresponding thiolate after adsorption to the AuNP surface, not in solution.

In Chapter IV, the AuNP synthesis described in Chapter II is adapted for use in a simple microfluidic device containing a UV-vis absorbance spectroscopy-equipped flow cell for the monitoring of AuNP properties. The synthesis of AuNPs in a flow environment provides opportunities to more closely control nanoparticle properties, while providing a potential approach for the high-throughput synthesis of functionalized nanoparticles with *in situ* monitoring for quality control purposes. The synthesis of AuNPs in flow reactors represents an important new strategy in the development of functionalized nanoparticle production. In this chapter, we demonstrate, for the first time, the synthesis of thiolate-protected AuNPs in a microfluidic device with size control provided by various reaction parameters. The incorporation of UV-vis analysis into the reactor platform provides effective real time qualitative monitoring of AuNP size. Unfortunately, the device proved highly susceptible to fouling due to uncontrolled AuNP aggregation within the reactor channels, which is a common problem in the synthesis of metal nanoparticles in microfluidic devices. Because of the fouling problems encountered in this reactor system, and the limited characterization data provided by the UV-vis observation cell, the use of a different flow reactor platform with replaceable components was explored.

Chapter V describes the adaptation of the Bunte salt AuNP synthesis for use in a capillary flow reactor equipped with an observation cell that permits the determination of AuNP sizes at different reaction times by simultaneous SAXS and UV-vis absorbance

spectroscopy analysis. The capillary flow reactor described in this chapter is primarily composed of disposable, commercially available components, mitigating the effect of reactor fouling over time. The capillary flow reactor provides a versatile synthetic platform that permits high-throughput synthesis of thiol-protected AuNPs with real-time quantitative monitoring of nanoparticle size. This reactor setup was also shown to permit higher throughput synthesis of thiol-stabilized gold nanoparticles than can be achieved in batch (~0.9 mg/min versus 0.3 mg/min). This capillary flow reactor provides an appealing platform for the rapid optimization of nanoparticle synthetic techniques, and the ability to monitor nanoparticle size quantitatively at various reaction times provides a potential opportunity use this reactor setup to investigate AuNP core growth in real time.

We exploited the capillary flow reactor to monitor AuNP growth kinetics in Chapter VI. We investigated the growth rate of AuNPs under different reaction conditions using the synthesis developed in Chapter II. We found that the growth rate of gold nanoparticles in this synthetic method depended on the concentration of gold used in the synthesis, and that the growth of the gold nanoparticles proceeds in part by a coalescence mechanism.

APPENDIX A

SUPPORTING INFORMATION FOR CHAPTER II

Bunte Salt Ligand Precursor Synthetic Details and Purification

Bunte salt ligand precursors were prepared by the method of Murray et al. Briefly, 2.0 grams of an appropriate functionalized organo halide were combined with 0.8 molar equivalents of sodium thiosulfate in 150 mL of deionized water and heated at reflux for four hours. Purification methods varied depending on the target ligand precursor as described below. The final ligand precursors are given in Fig. A.1.

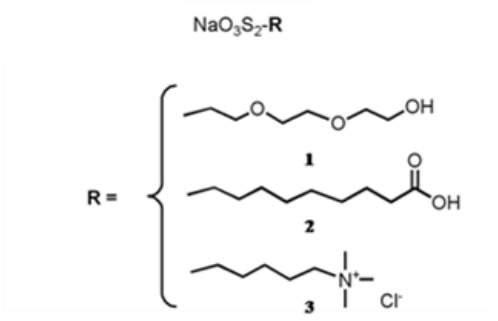

Figure A.1: The Bunte salt ligand precursors used in this study. They are named and abbreviated analogously to the corresponding thiols- mercaptoethoxyethoxy ethanol (MEEE BS, **1**), mercaptononanoic acid (MNA BS, **2**), and mercaptopentyl(trimethyl ammonium chloride) (MPTMA BS, **3**).

Purification of the Bunte Salt of MEEE BS (1). Water was removed from the cooled reaction mixture by rotary evaporation. The resulting oil was dried overnight *in vacuo*. The crude product (oily white semi-solid) was purified by dissolving it in ethanol and removing the sodium chloride side product by filtration. Rotoevaporation of the ethanol yields the product as a colorless, viscous oil with a very faint sulfurous odor. ^{1}H-NMR (300 MHz, D_2O): δ 3.25 (t, 2H), 3.50 (m, 2H), 3.55 (m, 6H) 3.75 (t, 2H)

Purification of the Bunte Salt of MNA BS (2). Water was removed from the cooled reaction mixture by rotary evaporation. The resulting solid was dried overnight *in vacuo*. The resulting white solid was purified by dissolving it in ethanol and removing the sodium bromide by gravity filtration. Ethanol was removed from the filtrate by rotary evaporation and drying the product *in vacuo* to yield an off-brown oily semi-solid compound. ^{1}H NMR (300 MHz, D_2O): δ 1.27 (m, 2H), 1.45 (m, 4H), 2.24 (t, 2H), 2.39 (t, 2H)

Purification of the Bunte Salt of MPTMA BS (3). Water was removed from the cooled reaction mixture by rotary evaporation and the crude product was dried *in vacuo* over night. The resulting solid was triturated with 30 mL acetone, followed by further trituration with 50 mL acetone. The remaining solid was dissolved in ethanol and stirred with 10 molar equivalents of NaCl for 30 min to promote ion exchange with the remaining bromide. The solution was then sonicated for 20 min. and the solid NaCl was removed by gravity filtration. The final product, recovered by rotary evaporation, is an oily colorless semi-solid. ^{1}H-NMR Data (300 MHz, D_2O): δ 3.33 (m, 2H), 3.12 (s, 9H), 3.15 (t, 2H), 1.85 (q, 4H), 1.50 (q, 2H)

In each case, following purification, the ligand precursors were analyzed by TGA to verify removal of the sodium halide side products. The presence of sodium halides in the sample raises the base line of the TGA data, as these solids are not volatilized below 500 °C.

Identification of a Colored Complex Formed Between the Bunte Salts and Gold(III)

All the ligand precursors (**1-3**) formed a colored complex when combined with tetrachloroaurate in aqueous solution. The color of this complex varied from brown to orange depending on the ligand precursor used. In order to determine the identity of these complexes, the complex formed between MEEE (**1**) and gold was isolated. For the (**1**)-Au complex, this solid was isolated, dried on the vacuum line and analyzed by ^{1}H-NMR and TGA. When the ^{1}H-NMR spectrum was taken of the colored complex in an acidic solution, some of the peaks associated with the ligand showed significant broadening, indicating that, in acidic solution, the ligand precursor and gold are associated, perhaps as a complex. However, this complex yields a colorless solution upon addition of sodium hydroxide, whereupon ^{1}H-NMR performed on the solution showed the presence of free ligand precursor once again. The ^{1}H-NMR data for the complex in acidic solution and basic solution are compared to the ^{1}H-NMR spectrum of the free ligand precursor in Table A.1.

TGA was also performed on the isolated solid and comparison to the ^{1}H-NMR and TGA data for the gold (I) polymer produced in the reaction between MEEE (thiol) and $HAuCl_4$ indicated that the isolated solid was *not* a gold(I) polymer of the

corresponding thiol (Figure A.2). We therefore conclude that the solid is a Bunte salt-gold complex with marginal water solubility, similar to what Murray originally postulated.[1] TGA analysis of the polymer formed in the reaction of gold(III) and the MEEE thiol indicates that this polymer is 54% gold by weight, as is expected for the Brust prep polymer [(Au-S$(CH_2)_2O(CH_2)_2O(CH_2)_2OH)_n$], (Fig. S2). In contrast, the insoluble complex is 66% gold by weight, and shows multiple, distinct transitions that are more consistent with a complex than the Au(I)-thiol polymer.

Table A.1. ^{1}H-NMR Data for the Ligand Precursor (1, MEEE) in the Presence of Au(III) in Acidic and Basic Solution Compared to the Free Ligand.

Acid	Base	Free Ligand Precursor
3.47, m	3.75, t, 2 H	3.75, t, 2 H
3.60, s	3.55, m, 8H	3.55, m, 8H
	3.50, m, 2 H	3.50, m, 2 H
	3.25 t, 2 H	3.25 t, 2 H

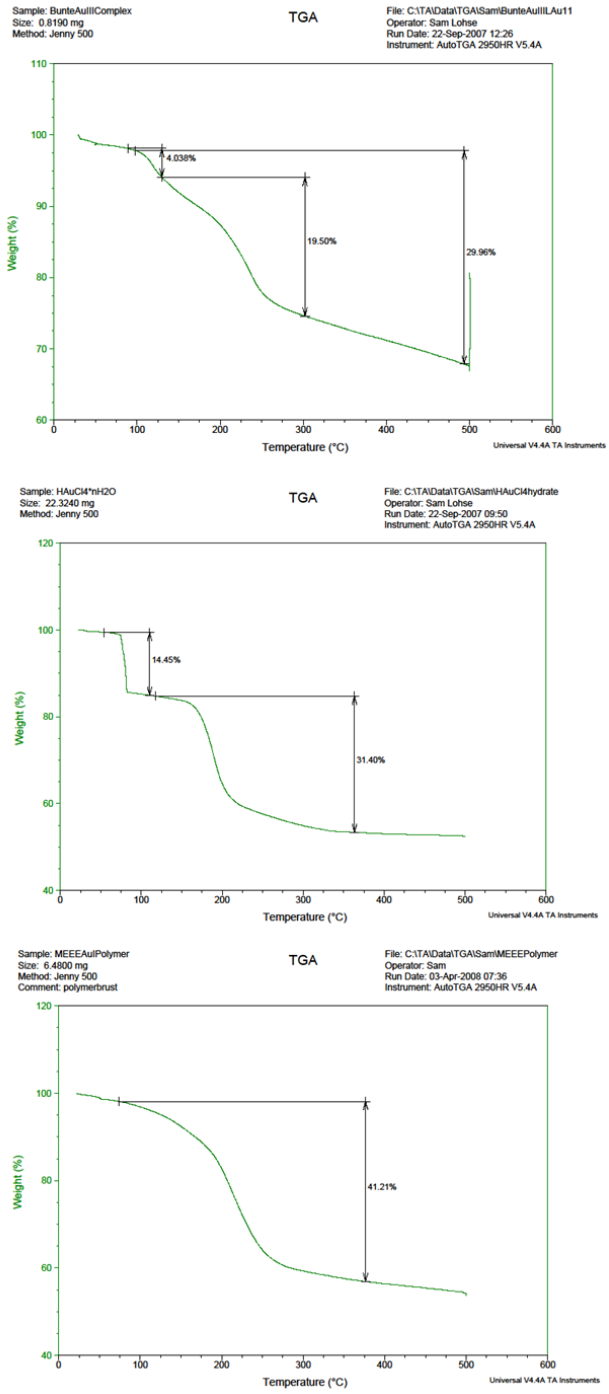

Figure A.2: TGA data (percent mass vs. temperature) for the Bunte-gold complex (top), the gold precursor $HAuCl_4 \bullet 3H_2O$ (middle), and the Au(I)-MEEE complex formed in the Brust prep (bottom). The TGA traces are dissimilar, and suggest that the Bunte salt forms a complex with tetrachloroaurate prior to nanoparticle formation.

Factorial Design of Experiments (DOE) Investigation of the Synthetic Reaction

In order to elucidate the effect of L:Au ratio, temperature and reducing agent concentration on AuNP core diameter and dispersity, we performed a design of experiments using L:Au ratio, temperature, and reducing agents equivalents as the factors, and particle core diameter and dispersity as the response variables. The design of experiments (factorial experiment design) entails testing a predetermined matrix of the terms (factors) in order to determine which factors have a significant effect on the response variables. One potential difficulty in this study is that the mean core diameter of the particle samples (as determined by TEM) is influenced by the dispersity (standard deviation) of the core diameter. So for samples where the difference in core diameter is small, the changes in core diameter may be masked by the dispersity of the sample. However, the ANOVA (Analysis of Variance) portion of the DOE is quite sensitive to detecting changes in the response variables, and therefore, we can detect changes in the mean particle diameter, so long as the product populations have normal distributions, and the differences in the standard deviation between all the samples is no more than twice the smallest standard deviation in the data set. Even though the mean diameter and dispersity are related portions of the particle size distribution, the effect of L:Au ratio, temperature, and reducing agent concentration on the diameter and dispersity have been studied for other synthetic systems.

A DOE investigation of the nanoparticle formation reaction was performed using an approach that involved producing a matrix of data points for three parameters (factors): L:Au ratio, temperature, and reductant equivalents. Each combination of these

three parameters was tested at both high and low values (two levels). Midpoint values for all the parameters were also included in the analysis. The DOE investigation was performed as two separate investigations in two areas of the L:Au ratio parameter space. In the first experiment, L:Au ratios from 0.25 to 3. In the second version, lower L:Au ratios were explored- 0.16 to 1.0. The results from both studies revealed the same trends, producing essentially identical statistical conclusions about the effects of L:Au ratio, temperature, and the molar equivalents of reducing agent employed. The principal difference was that in the second study, we found that L:Au ratio had a greater impact on dispersity than in the first study, but still no statistically significant effect. The data from these studies is given in Table A.2 and an example Main Effects Plot is gven in Figure A.3.

Table A.2. Summary of Factorial Design Experiment Raw Data

L:Au	T (° C)	Reductant Equivalents[a]	Diameter (nm)	Dispersity (± nm)[b]
3.0	0	1	2.5	1.3
3.0	0	10	1.6	0.4
3.0	60	1	2.0	0.5
3.0	60	10	2.4	0.7
1.6	24	5.5	2.5	0.9
1.0	0	1	3.3	1.1
1.0	0	10	2.9	0.8
1.0	60	1	3.8	3.1
1.0	60	10	3.1	1.1
0.6	24	5.5	3.3	1.1
0.25	0	1	2.6	1.1
0.25	0	10	3.0	1.0
0.25	60	1	30.0	9.6
0.25	60	10	3.4	1.2
0.17	0	1	5.8	4.1
0.17	0	10	4.5	1.9
0.17	60	1	5.2	4.1
0.17	60	10	10.1	2.9
0.17	60	10	3.1	1.1

[a]- Molar equivalents of sodium borohydride used with respect to gold (R:Au).

[b]- Dispersity is given as 1σ of the mean core diameter.

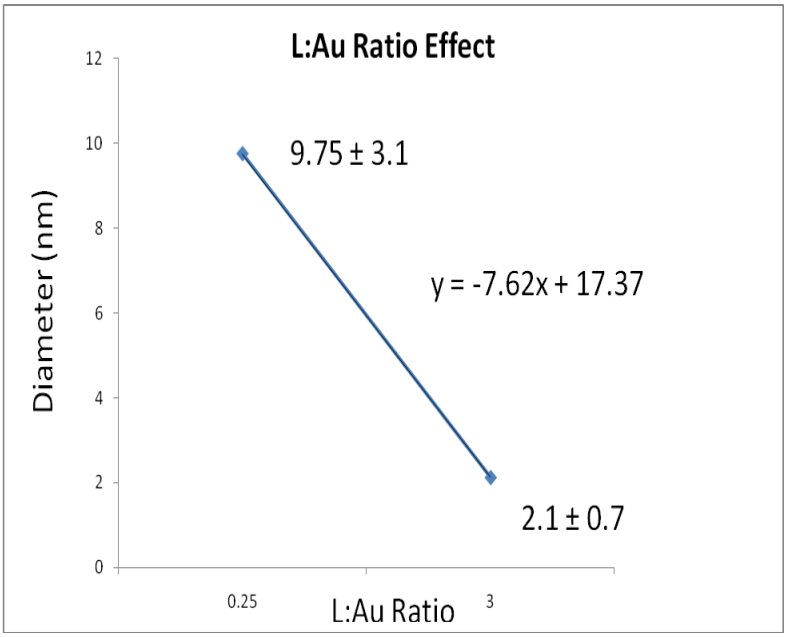

Figure A.3: Example Main Effect Plot for the effect of L:Au ratio on particle diameter. The particle size decreases as L:Au ratio increases. The average diameter and standard deviations for the high and low values for the L:Au ratio have been included.

In addition, ANOVA analysis of the raw data was used to construct Main Effect Plots. The main effects plots are created by determining the average response value at a given L:Au Ratio, and then graphing this versus the L:Au ratio. So in this case, the data point at 1:4 L:Au is an average of all the data points with L:Au = 1:4 contained in Table A.2. In this case, the mean diameter at a L:Au ratio of 1:4 is 9.75 ± 3.1 nm. This is plotted versus the L:Au ratio, and the same is done for the high L:Au ratio (3:1) 2.1 ± 0.7 nm, yielding the main effects plot given above (Figure A1.3). The slope of the line of the main effects plot is a measure of the significance of the factor.

The absolute value of the slope of the main effects plot is also known as the standardized effect. The greater the slope of the line, the greater the effect of the term. The standardized effects for each factor can be compared by constructing a Pareto chart of the effects (Figure A.4). The main effects plot and Pareto analysis are particularly effective in illustrating trends in the data that cannot be easily discerned by eye. In Table A.2, many of the core diameters seem to be roughly equivalent (particularly when the dispersities of the samples are considered), however, from the main effects plot, it is clear that there is a significant difference between the core diameters, even when the dispersity is considered. Our analysis shows that the core diameter of the particles depends on all of the parameters: L:Au ratio, temperature, and reducing agent equivalents. The dispersity in core diameter, on the other hand, is independent of the L:Au ratio used in the synthesis, but depends strongly on temperature and the number of reducing agent equivalents used with respect to gold.

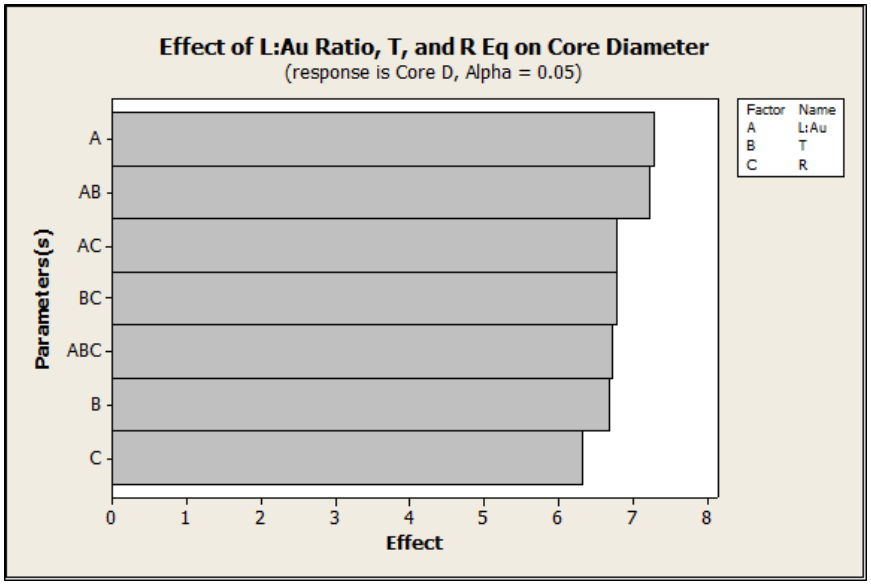

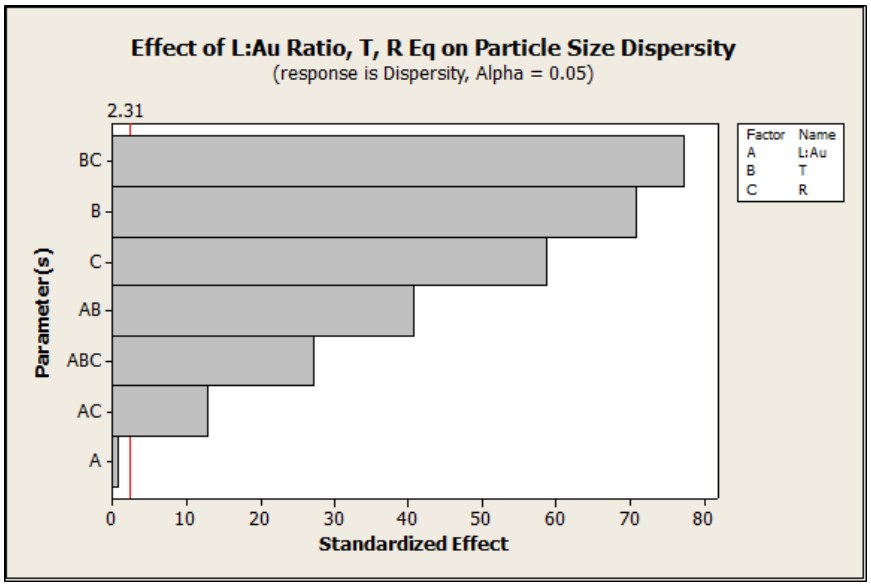

Figure A.4: Pareto Standard Effects Plots derived from the DOE data for the effect on core diameter (above) and dispersity (below). The data suggest that while the core diameter of the particles produced depends on the L:Au ratio, temperature, and the number of reducing agent equivalents used in the reaction, the dispersity is primarily dependent on temperature and reductant equivalents used.

Additional TEM Micrographs of 1,2,3-Functionalized AuNPs

Additional TEM mcirographs for AuNPs functionalized using the Bunte salt ligand precursors (1,2, and 3) are shown below (Figure A.5). Purified particle solutions were dropcast onto Ted Pella SiO/Cu Mesh TEM grids. Particle size analysis was performed using Image J Software (N > 900). Scale bars are 50 nm.

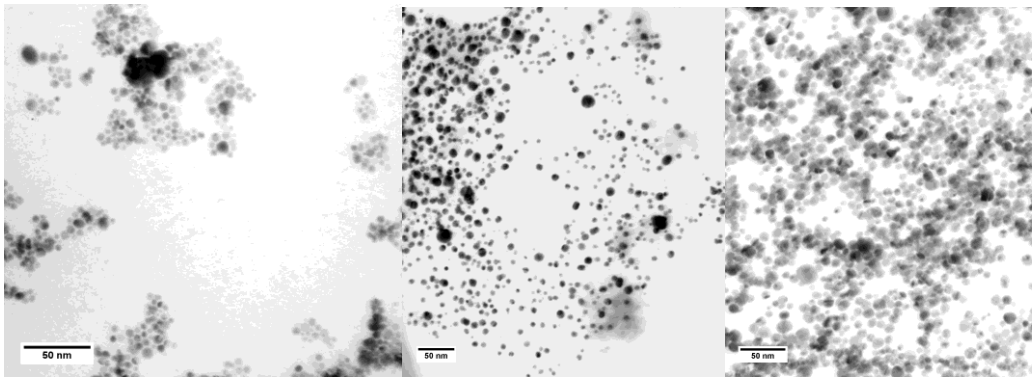

Figure A.5. Additional TEM micrographs of AuNPs functionalized with (L,**1**) MEEE, (C, **2**) MNA, and (R, **3**) MPTMA. Scale Bars are 50 nm.

XPS Analysis of Functionalized Nanoparticles

XPS analysis was performed on the functionalized nanoparticles produced using ligand precursors **1** and **2**. The spectra are shown in Fig. A.6. In the S2p region of the spectrum peaks that indicate thiolate bonds to the gold nanoparticle core were observed, as well as peaks for oxidized sulfur. This region of the spectrum is shown, for both unpurified (Fig. A.6 A and B) samples of MEEE-functionalized and MPTMA-functionalized AuNPs respectively, and purified MEEE AuNP samples (Fig. A.6C).

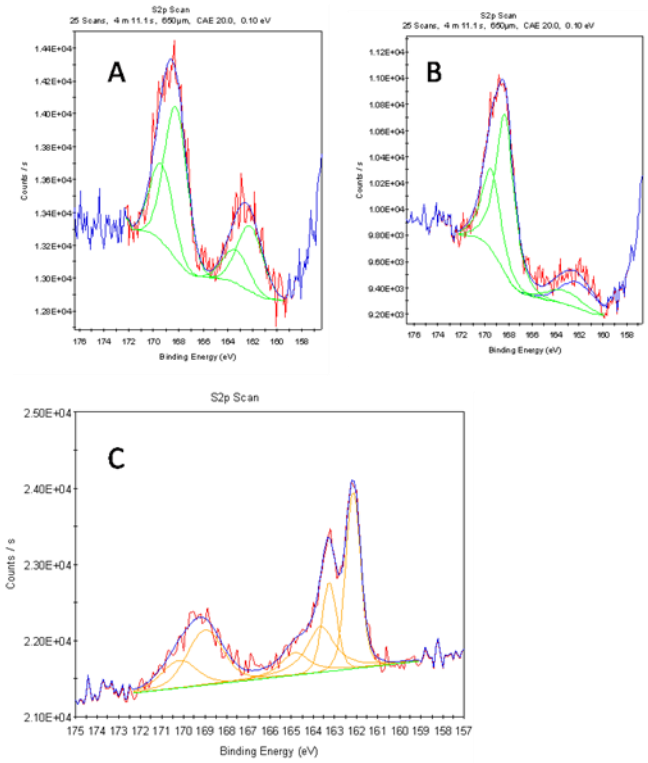

Figure A.6: XPS data for the S2p region of the spectrum.(A) XPS data for MEEE-stabilized AuNPs, and (B) for the MPTMA-functionalized particles. Both ligand precursors show thiolate and oxidized sulfur present in the monolayer, suggesting that regardless of the terminal functionality, the ligand precursor forms a thiolate bond to the gold nanoparticle core, but that the cloven sulfite group may also persist in the monolayer. The purified sample of the MEEE particles (C) shows significant removal of the oxidized sulfur, suggesting that the majority of oxidized sulfur in the ligand shell is labile. The presence of some unbound sulfur is also indicated. Binding energies were set relative to the Au 4f peak (84.0 eV).

Following purification, XPS analysis of the purified particle solution shows a decrease in the amount of the oxidized sulfur present in the particle monolayers, while the thiolate S2p peak remains, indicating that the particles are protected by a fully-formed

thiolate monolayer, and that the excess oxidized sulfur has been largely removed by purification. Even in the purified samples, however, there is evidence of multiple sulfur species- in addition to the thiolate and oxidized sulfur peaks, the thiolate peak is somewhat broadened, with a small shoulder at higher binding energy (165.0 eV). This indicates the presence of either unbound thiols, or Bunte salts that have not been converted to thiolates, but remain adsorbed to the particle surface. In their synthesis of Bunte salt-derived AuNPs, Murray's group observed only thiolate sulfur on the AuNP surface by XPS, contrary to what we have reported here. This difference likely stems from the fact that the Murray synthesis was performed in a biphasic reaction mixture and the oxidized sulfur will not associate with the particle surface once the particles have been transferred to the toluene layer. The results of our XPS study are more similar to XPS spectra taken for Bunte salt-derived monolayers on 2-D gold surfaces prepared in aqueous environments.

FTIR Analysis of Free Ligand and Functionalized AuNPs.

In order to verify the functional group content of the functionalized gold nanoparticles, the lyophilized particles were cast in a KBr pellet and then analyzed by FTIR. When casting the plate, 1.0 mg of the lyophilized of the particles were combined with 10.0 mg of oven-dried KBr. Spectra of the lyophilized particles are shown below, with comparison to the free ligand spectrum (Figure A.7). Key diagnostic peaks are highlighted with arrows in each spectrum. The O-H stretches can be seen in the MEEE and MNA samples (3400 cm^{-1}, 3150 cm^{-1}), as can the carboxylic acid and carboxylate carbonyls (1710 cm^{-1}, 1585 cm^{-1}) in the MNA AuNP sample. In the MPTMA spectrum,

only the sp^3 C-H stretching is readily apparent (2920, 2830 cm^{-1}), Nevertheless, the FTIR analysis indicates that the desired ω-functionalities are present post-synthesis.

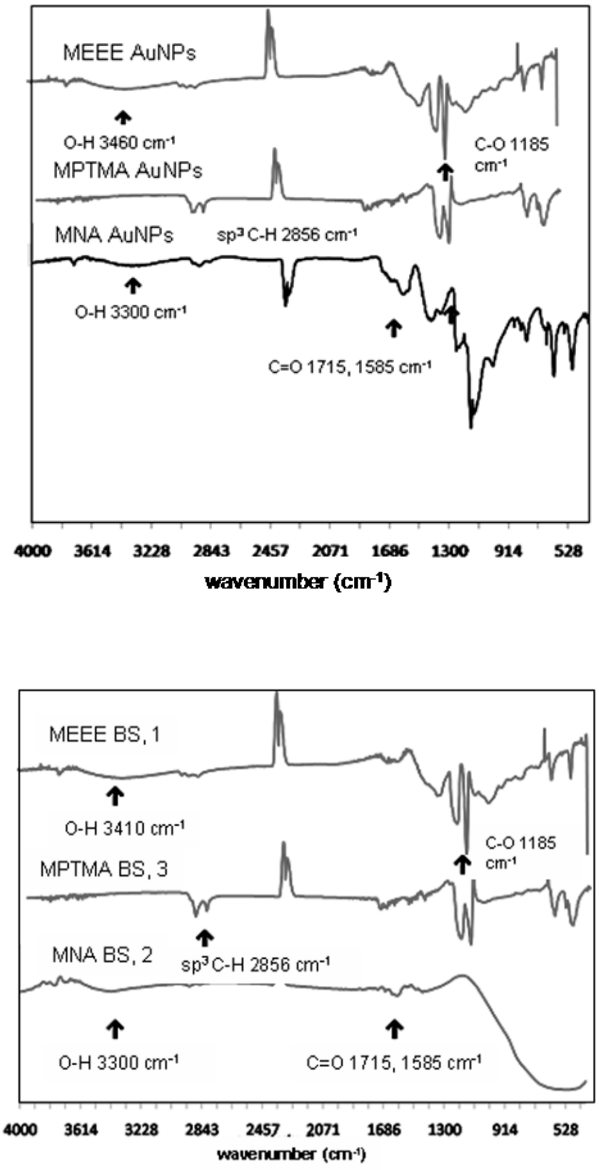

Figure A.7: FTIR Spectra of functionalized, purified AuNP samples (above) and Bunte salt ligand precursors (below). The diagnostic stretches are indicated in each spectrum.

APPENDIX B

SUPPORTING INFORMATION FOR CHAPTER III

TEM and XPS Characterization Data for 'Stable' and 'Unstable' MEEE-AuNPs

We prepared MEEE-functionalized AuNPs under reaction conditions that we had previously observed produced a mixture of 'stable' and 'unstable' MEEE AuNPs. The reaction conditions used are described in our previous work, but briefly, the MEEE AuNPs were synthesized at 1:6 MEEE BS:Au, 2.5:1 BH_4^-:Au, at 24° C. We performed the synthesis four times, and obtained two batches of AuNPs that were 'stable' and two that were 'unstable.' Representative TEM micrographs for each batch, as well as size distribution data are displayed for each batch are shown in Figure B.1. The size distribution data for each batch were as follows: Samples A and D, the stable samples, had size distributions of 6.1 ± 1.1 nm and 5.1 ± 1.6 nm, respectively. Samples B and C, the unstable AuNP solutions, had size distributions of 9.8 ± 2.1 and 6.9 ± 1.1 nm, respectively.

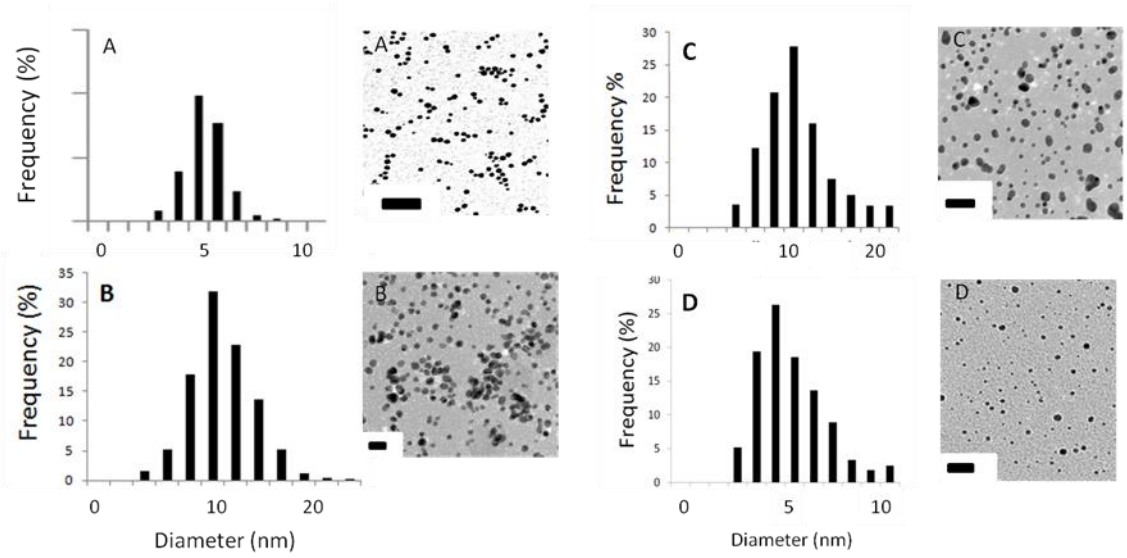

Figure B.1: Representative TEM micrographs and size distributions for two 'stable' and two 'unstable' MEEE-AuNP samples, all prepared at 1:6 L:Au, 2.5:1 BH_4^-:Au, and 24 °C. A and D represent the 'stable' particle solutions, while B and C are the 'unstable' AuNP solutions. Scale bars are 20 nm.

Samples A and B were then purified and analyzed by XPS to determine their ligand shell composition and the thiolate S:Au ratio for each sample. Each sample was analyzed in triplicate, and the representative XPS spectra are presented below (Figure B.2). Thiolate sulfur:gold ratios were determined from the areas of the Au 4f peak (84.0 eV) and the bound thiolate peak (162.5eV). In all of these spectra, three types of sulfur species are observed: bound thiolate (162.5 eV), adsorbed Bunte salts (163.5 eV and 168.9 eV), and various adsorbed oxidized sulfur species (168.7 eV).

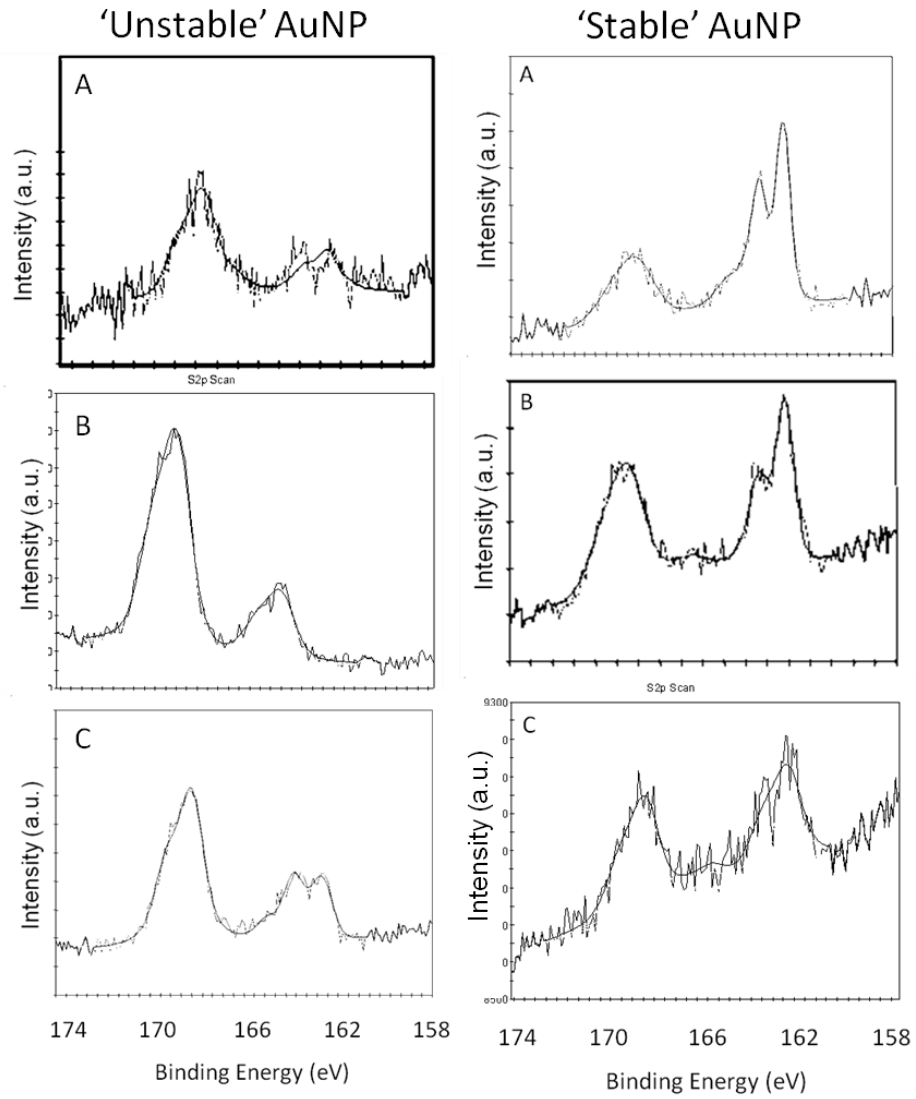

Figure B.2: Representative XPS spectra (S2p region) for the 'unstable' and 'stable' AuNP samples B and A. All spectra were referenced to the Au4f peak at 84.0 eV.

Exploration of the Effect of Reaction Conditions on MEEE-AuNP Stability

We studied the effect of a number of parameters on the formation of 'stable'/ 'unstable' MEEE AuNPs under the following reaction conditions: 1:6 L:Au, 2.5:1 BH_4^-:Au, and 25 °C. We studied the effect of reagent mixing time, reaction scale, stirring rate, reagent age, and pre-heating the reagent solutions on the stability of the AuNPs produced.

Effect of Ligand Precursor Age. Two trials to prepare MEEE-AuNPs were performed using analogous experimental procedures except for the age of the prepared MEEE Bunte salt precursor ligand solution. The first batch employed a MEEE ligand solution that had been aged for a two-month period in a scintillation vial. The second batch of AuNPs was synthesized from a freshly prepared solution of the same precursor ligand. UV-vis absorbance spectroscopy in conjunction with the metal cation addition assay (Experimental, Chapter III) were used to determine the resulting stability of each NP sample. Following synthesis and purification, both samples of MEEE AuNPs show a distinct plasmon absorption at 520 nm (Figure A2.3 A, green and purple traces). No spectral response was noted for either NP solution upon the addition of $Gd(NO_3)_3$ (Figure B.3 A, pink and blue traces), indicating that the age of the ligand solution does not play a contributing role in the stability (and hence, the extent of ligand shell formation) of MEEE functionalized AuNPs.

Effect of Reaction Vessel Size. The second control study was designed to understand the role that reaction vessel size has on the final stability of MEEE-AuNPs. Specifically, reaction vessel size was tested to determine the impact that surface vessel area and effective mixing rates play in monolayer formation. First, a series of reactions having identical synthetic conditions except for vessel size were performed. All ten reactions carried out in 20-mL scintillation vials produced AuNPs that were not stable to the addition of Gd^{3+} (Figure B.3 A, black and green traces). However, six of the ten trials performed in a 250-mL round-bottomed flask produced MEEE-AuNPs that were stable to the addition of Gd^{3+} (Figure B.3 B, blue and red traces).

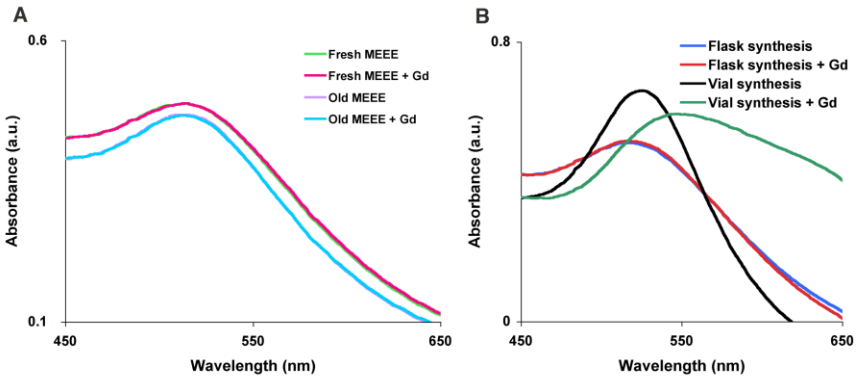

Figure B.3: UV-vis absorbance spectra for the control experiments designed to explore the impact that ligand solution age and reaction vessel size have on MEEE AuNP synthesis. The initial absorbance spectra for particles synthesized using a freshly MEEE ligand solution (A, green trace) and particles prepared from an aged MEEE solution (A, purple trace) both have a distinct absorbance at 520 nm. The absorbance remains unchanged upon the addition Gd^{3+}, indicating that the age of ligand solution does not play a significant role in the stability of the final nanoparticle product. MEEE AuNPs prepared in a 250-mL reaction flask (B, blue trace) and a 20-mL scintillation vial (B, black trace) also have a distinct absorption at 520 nm. The particles prepared in the larger flask show no response to the addition of Gd^{3+} (B, red trace), while the particles prepared in the smaller vial aggregate immediately upon the addition of Gd^{3+} (B, green trace), indicating their instability due to incomplete ligand shell formation. These results indicate that variations in reaction conditions generated from by the vessel can impact the stability of the final nanoparticle product under these conditions.

The production of both stable and unstable MEEE AuNPs from the larger reaction flask implied that surface area was not a primary contributing factor to stability. However, despite strict control over the reaction parameters including temperature, concentration, and exposure to light, and precursor mixing time, drastic differences in the integrity of the final NP product was observed between the larger flask trials and those performed in scintillation vials. This effect of scale may be related to the mixing rate

achieved in the respective reaction vessels. Vortex mixing was easily achieved in the 250 mL round-bottomed flasks, but was not achieved in the scintillation vials. In addition, two of the four RBF experiments that produced unstable MEEE-AuNPs under these reaction conditions had significant fluctuations in the stirring rate within the flask, preventing vortex mixing from continuing uninterrupted shortly after sodium borohydride addition.

The Effect of Pre-mixing MEEE BS and $HAuCl_4$ Time. Synthetic trials to produce AuNPs that involved the addition of $NaBH_4$ immediately following the addition of gold and ligand solutions consistently resulted in AuNP aggregation and precipitation. Conversely, NP trials that allowed the gold and ligand solutions to stir extensively before the addition of the reducing agent resulted in a higher proportion of stable AuNPs. This suggested that an interaction between the gold and ligand species must take place prior to the addition of the reductant in order for NP formation to occur. UV-vis spectroscopy was used to monitor a mixture of Au salt and ligand solution over time. Two distinct absorbance bands corresponding to the gold salt and precursor ligand can be seen (Figure B.4 A, red and blue traces, respectively). The UV-vis spectra shows a distinct change from the mixture of Au salt and precursor ligand to the formation of a new species at t = 6.5 minutes. By t = 9 minutes, formation of this new species is complete and no further changes are monitored.

As a final confirmation that the formation of this monomer was occurring and the heat from the UV-vis light source did not impact the changes in absorbance observed, the gold salt was heated and monitored by UV-vis. An aqueous solution of gold salt was first

heated for 40 minutes (Figure B.4 B, red trace). No change in the absorbance spectra was determined after prolonged, gentle heating. The gold salt solution was then subjected to quick, intense heating (Figure B.4 B, red trace). Once again, no changes were observed in the absorbance spectra. This study confirms that the spectral changes observed for the gold salt and precursor ligand were the result of the formation of a new species, and suggest that the ligand and gold salt should be allowed to stir for a minimum of 10 minutes prior to addition of the reducing agent in order for stable particles to successfully form.

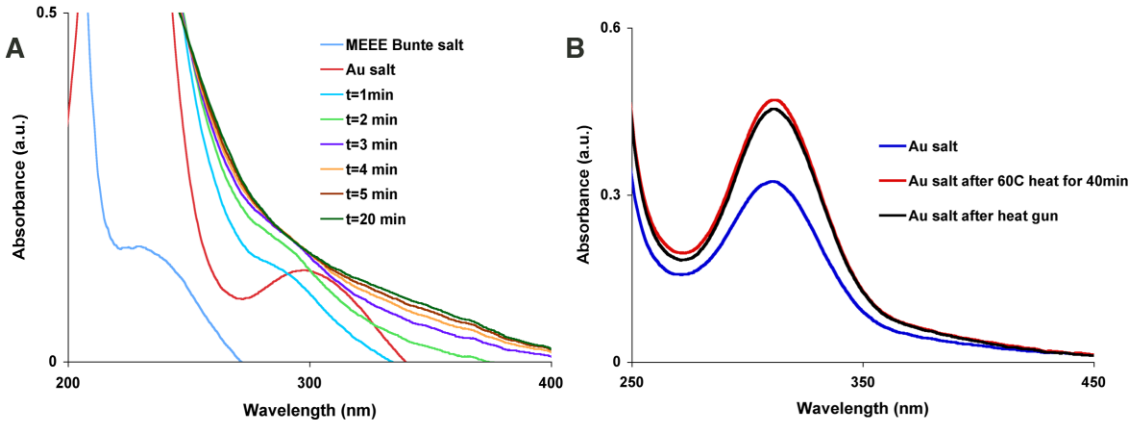

Figure B.4: UV-vis spectroscopy was used to monitor Au-ligand complex formation and the impact of heat on $HAuCl_{4\ (aq)}$. The absorbance spectra of the gold salt and ligand solution (A) were collected over a 20 min time interval to monitor the Au-ligand complex formation that occurs prior to the $NaBH_4$ addition. Initially, the gold salt shows an absorbance peak at 300 nm corresponding to the presence of Au^{3+} in solution (A, red trace). Within a minute, the formation of a new gold species begins to change the absorbance spectra. After 4 minutes the absorbance peak at 300 nm has disappeared, suggesting Au^{3+} is no longer present. In order to explore whether heat causes changes to the gold salt, UV-vis spectra were collected after sustained heating (B, red trace) and direct high temperature heating (B, black trace). No changes in the absorbance spectra were observed under either of these conditions, suggesting that the heat from the UV-vis lamp was not responsible for the changes in the absorbance spectra observed during experiment A.

TEM and XPS Characterization Data for MEEE-AuNPs Prepared at Various BH_4^-:Au Ratios

In order to determine the effect of the borohydride:gold ratio on the formation of stable, ligand-protected MEEE-AuNPs, we prepared ~7.0 nm MEEE AuNPs using the following reagent conditions: 1:20 L:Au, 24°C, and the amount of borohydride that was added was varied to achieve BH_4^-:Au molar ratios of 1.5:1, 5:1, and 10:1. The total

volume of the reaction mixture and all additions was held constant. Three samples were prepared for each reaction condition. Representative TEM data for each reaction condition (Figure B.5), and a representative XPS spectrum (S2P region, Figure B.6) is given below for every sample.

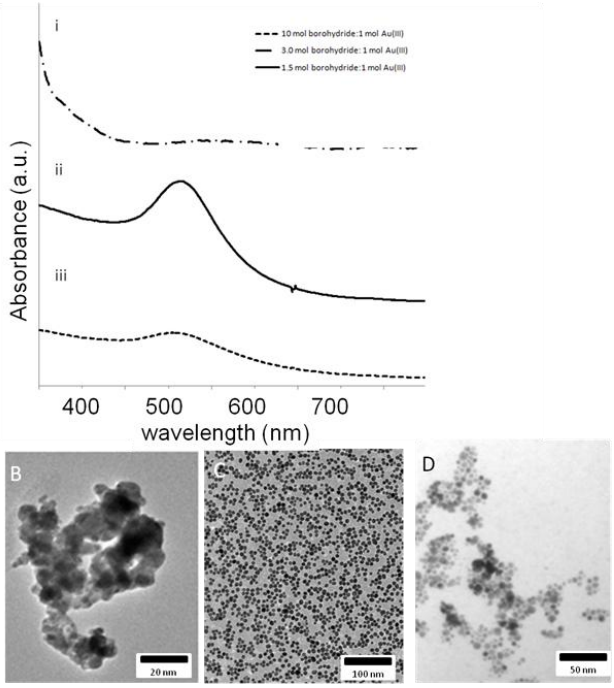

Figure B.5. Representative UV-vis absorbance data for MEEE AuNPs prepared at different borohydride:gold molar ratios. (A) Absorbance data for MEEE AuNPs prepared at (i)1.5:1, (ii) 5.0:1, and (iii) 10.0:1 mols borohydride: mol gold. Representative TEM micrographs are also given. (B) 1.5:1, (C) 5.0:1, (D) 10.0:1. Scale bars are 20 nm, 100nm, and 50 nm respectively.

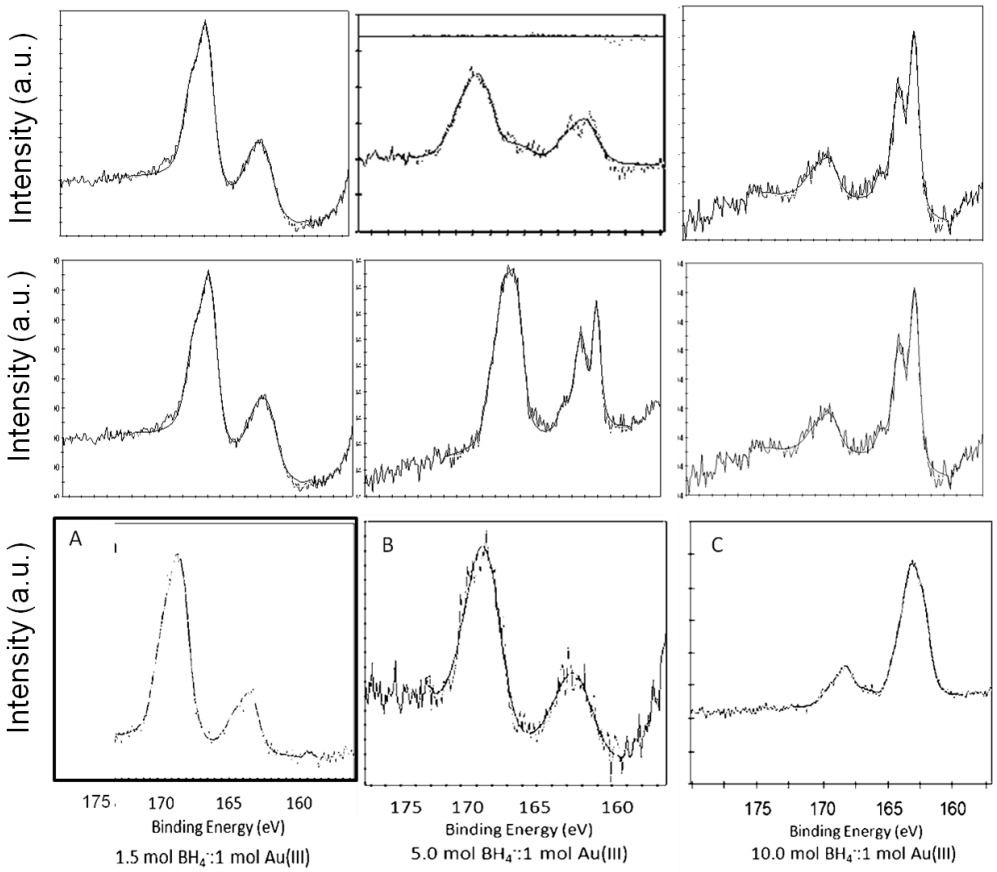

Figure B.6: Representative XPS spectra for each sample prepared in the study of the effect of the borohydride:gold ratio on the extent of ligand shell formation. (A) The S2P region of the three samples prepared at the 1.5:1 ratio. (B) The 5.0:1 ratio, and (C) The 10.0:1 ratio. The peaks of all spectra were referenced to the Au 4f peak (84.0 eV).

<u>TEM and XPS Characterization Data for the Conversion of 'Unstable' to 'Stable' MEEE-AuNPs Mediated by Borohydride.</u> Representative XPS spectra (S2p region) for purified 'unstable' MEEE-AuNPs and 'stable' MEEE-AuNPs, after the addition of further sodium borohydride are given (Figure B.7). Binding energies are referenced to Au 4f (84.0 eV).

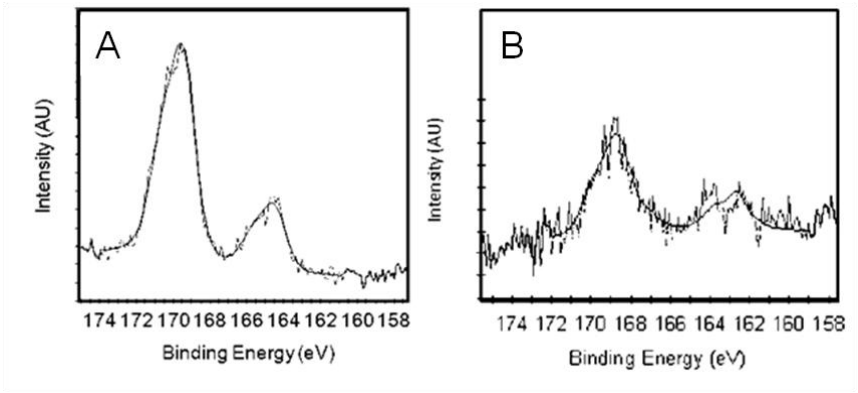

Figure B.7: Representative spectra, S2P region, for (A) 'unstable' MEEE-AuNPs that were made 'stable' (B) by the addition of further sodium borohydride. Binding energies were referenced to Au4f 84.0eV.

REFEERENCES CITED

Chapter I

1. Daniel, M. C.; Astruc, D. *Chem Rev* **2004**, 104, 293.
2. Burda, C.; Chen, X.; Narayanan, R.; El-Sayed, M.A. *Chem Rev* **2005,** *105*, 1025.
3. Dahl, J. A.; Maddux, B. L. S.; Hutchison, J. E. *Chem Rev* **2007**, *107*, 2228.
4. Murphy, C. J. *J Mater Chem* **2008**, *18*, 2173.
5. Sardar, R.; Funston, A. M.; Mulvaney, P.; Murray, R. W. *Langmuir* **2009**, *25*, 13840.
6. Goessman, H.; Feldman, C. *Angew Chem Int Ed* **2010**, *49*, 1362.
7. American Chemical Society, *Scifinder Software*, Washington D.C., **2009**.
8. Grainger, D. W.; Castner, D. G. *Adv Mater* **2008**, *20*, 867.
9. Hutchison, J. E. *ACS Nano* **2008**, *2*, 395.
10. Alikilany, A. M.; Nagaria, P. K.; Hexel, C. R.; Shaw, T. J.; Murphy, C. J.; Wyatt, M. D. *Small* **2009**, *5*, 701.
11. Richman, E. K.; Hutchison, J. E. *ACS Nano* **2009**, *3*, 244.
12. Van Der Vost, G.; Dewulf, J.; Aelterman, W.; Witte, B. D.; Langenhove, H. V. *Ind Eng Chem Res* **2009**, *48*, 5344.
13. Noyori, R. *Nat Chem* **2009**, *1*, 5.
14. Mueller, R.; Madler, L.; Pratsinis, S. E. *Chem Eng Sci* **2003**, *58*, 1969.
15. Anastas, P. T., Levy, I. J., Parent, K. E. *Green Chemistry Education: Changing the Course of Chemistry*. **2009**, *ACS Symposium Series*. 1011.
16. Groisman, Y.; Gedanken, A. *J Phys Chem C* **2008**, *112*, 8802.
17. Reuge, N.; Basca, R.; Serp, P.; Caussat, B. *J Phys Chem C* **2009**, *113*, 19845.

18. Eckelman, M. J.; Zimmerman, J. B.; Anastas, P. T. *J Ind Ecol* **2008**, *12*, 316.

19. Talapin, D. V.; Lee, J.- S.; Kovalenko, M. V.; Shevchenko, E. V. *Chem Rev* **2010**, *110*, 389.

20. Eustis, S.; El-Sayed, M. *Chem Soc Rev* **2006**, *35*, 209.

21. Jana, N. R.; Chem, Y.; Peng, X. *Chem Mater* **2004**, *16*, 3931.

22. Grzelczack, M.; Perez-Juste, J.; Mulvaney, P.; Liz-Marzan, L. M. *Chem Soc Rev* **2008**, *37*, 1783.

23. Mao, Y.; Park, T.- J.; Zhang, F.; Zhou, H.; Wong, S. S. *Small* **2007**, *3*, 1122.

24. Murphy, C. J.; Thompson, L. B.; Alkilany, A.; Sisco, P. N.; Boulos, S. P.; Sivapalan, S. T.; Yang, J. A.; Chernak, D. J.; Huang, J. J *Phys Chem Lett* **2010**, *1*, 2867.

25. Turkevich, J. *Gold Bull* **1985**, *18*, 86.

26. Brust, M.; Walker, M.; Bethell, D.; Schiffrin, D. J.; and Whyman, R. J. *Chem Soc Chem Commun* **1994**, 801.

27. Murray, C. B.; Norris, D. J.; Bawendi, M. G. *J Am Chem Soc* **1993**, *115*, 8706.

28. Sau, T. K.; Murphy, C. J. *J Am Chem Soc* **2004,** *126*, 8646.

29. Jana, N. R. *Small* **2005**, *1*, 875.

30. Nikoobakht, B.; El-Sayed, M. A. *Chem Mater* **2003**, *15*, 1957.

31. Huber, D. L. *Small* **2005**, *5*, 482.

32. Mayoral, A.; Vazquez-Duran, A.; Barron, H.; Jose-Yacaman, M. *App Phys A* **2009**, *97*, 11.

33. Cui, F.- H.; Vashist, S. K.; Al-Rubeann, K.; Luong, J. H. T.; Sheu, F.- W. *Chem Res Tox* **2010**, *ASAP*.

34. Sweeney, S. F.; Woerhle, G. H.; Hutchison, J. E. *J Am Chem Soc* **2006**, *128*, 3190.

35. Peng, Z.; Peng, X. *J Am Chem Soc* **2001**, *123*, 183.

36. Qu, L.; Peng, Z.; Peng, X. *Nano Lett* **2001**, *1*, 333.

37. Song, Y.; Hormes, J.; Kumar, C.S.S.R. *Small* **2008**, *4*, 698.

38. Pradhan, N.; Battaglia, D.M.; Liu, Y.; Peng, X. *Nano Lett* **2007**, *7*, 312.

39. Pradhan, N.; Peng, X. *J Am Chem Soc* **2007**, *129*, 3339.

40. Xie, R.; Peng, X. *J Am Chem Soc* **2009,** *131*, 10645.

41. Engelbrekt, C.; Sorensen, K. H.; Zhang, J.; Welinder, J.; Jensen, P. S.; Ulstrup, J. *J Mater Chem* **2009**, *19*, 7839.

42. He, F.; Lin, J.; Roburst, C. B.; Zhao, D. *Ind Eng Chem Res* **2009**, *48*, 6550.

43. Weare, W. W.; Reed, S. M.; Warner, M. G.; Hutchison, J. E. *J Am Chem Soc* **2000**, *122*, 12890.

44. Auffan, M.; Rose, J.; Bottero, J.- Y.; Lowry, G. V.; Jolivet, J.- P.; Wiesner, M. R. *Nat Nanotech* **2009**, *4*, 634.

45. Garg, N.; Scholl, C.; Mohanty, A.; Jin, R. *Langmuir* **2010**, *26*, 10271.

46. Shon, Y. -S.; Murray, Wuelfing, P. W.; R. W. *Langmuir* **2001**, *17*, 1255.

47. Zhang, S.; Leem, G.; Randall Lee, T. *Langmuir* **2009**, *25*, 13855.

48. Lohse, S. E.; Dahl, J. A.; Hutchison, J. E. *Langmuir*, **2010**, *26*, 7504.

49. Shon, Y.- S.; Cutler, E. *Langmuir* **2004**, *20*, 6626.

50. Lisowski, C. E.; Hutchison, J. E. *Anal Chem* **2010**, *81*, 10246.

51. Caragheorgheopol, A.; Chechik, V. *Phys Chem Chem Phys* **2008**, *10*, 5029.

52. Polte, J. *J Phys Conference Series* **2010**, *247*, 1.

53. Murray, C. B. *Science* **2009**, *324*, 1276.

54. Zheng, H. M.; Smith, R. K.; Jun, Y. W.; Kisolowski, C.; Dhamen, U.; Alivasatos, A.P. *Science* **2009**, *324*, 1309.

55. Niidome, Y.; Nakamura, Y.; Honda, K.; Akiyama, Y.; Nishioka, K.; Kawasaki, H.; Nakashima, N. *Chem Commun* **2009**, 1754.

56. Moussa, N.; Ringnalda, J. F.; Agarwal, M. A.; Nestor, N. K.; Zaluzec, J.; Norris, T. B. *Nano Lett* **2008**, *8*, 3200.

57. Kumar, S.; Gandhi, K. S.; Kumar, R. *Ind Eng Chem Res* **2007**, *46*, 3128.

58. Ji, X.; Song, X.; Li, J.; Bai, Y.; Yang, W.; Peng, X. *J Am Chem Soc* **2007**, *129*, 13939.

59. Orrendorf, C. J.; Murphy, C. J. *J Phys Chem B* **2006**, *110*, 3990.

60. Gou, L.; Murphy, C. J. *Chem Mater* **2005**, *17*, 3668.

61. Rayavarapu, R. G.; Ungureanu, C.; Krystek, P.; van Leeuwen, T. G.; Manohar, S. *Langmuir* **2010**, *26*, 5050.

62. Henkel, A.; Schubert, O.; Plech, A.; Sonnischen, C. *J Phys Chem C* **2009**, *113*, 10390.

63. Shields, S. P.; Richards, V. N.; Buhro, W. E. *Chem Mater* **2010**, *22*, 3212.

64. Polte, J.; Ahner, T. T.; Delissen, F.; Sokolov, S.; Emmerling, F.; Thunemann, A. F.; Kraehnert, R. *J Am Chem Soc* **2010**, *132*, 1296.

65. Saunders, A. E.; Sigman, M. B.; Korgel, B. A. *J Phys Chem B* **2004**, *108*, 193.

66. Jana, N. R.; Peng, X. *J Am Chem Soc* **2003**, *125*, 14280.

67. Wang, F.; Tang, R.; Kao, J. L. F.; Digmon, S. D.; Buhro, W. E. *J Am Chem Soc* **2009**, *131*, 4983.

68. Kloper, V.; Osovsky, R.; Kolny-Olesnik, J.; Sashchink, A.; Lifshitz, G. *J Phys Chem C* **2007**, *111*, 10336.

69. Wang, F.; Tang, R.; Buhro, W. E. *Nano Lett* **2008,** *8*, 3521.

70. Xie, R.; Rutherford, M.; Peng, X. *J Am Chem Soc* **2009**, *131*, 5691.

71. Goubet, N.; Ding, Y.; Brust, M.; Wang, Z. L.; Pileni, M. P. *ACS Nano* **2009**, *3*, 3627.

72. Li, Y.; Zalazhan, O.; Xu, B.; Gao, Y.; Modest, J. M.; Tang, Y. Y. J.; *J Am Chem Soc* **2011**, *139*, 2092.

73. Haiss, W.; Thanh, N. T. K.; Aveyard, J.; Fernig, D. G. *Anal Chem* **2007**, *79*, 4215.

74. Khlebtsov, N. G. *Anal Chem* **2008**, *80*, 6620.

75. Qu, L.; Yu, W. W.; Peng, X. *Nano Lett* **2004**, *4*, 465.

76. McKenzie, L. C.; Haben, P. M.; Kevan, S. D.; Hutchison, J. E. *J Phys Chem C* **2010**, *114*, 22055.

77. Whitesides, G. M. *Nature* **2006**, *442*, 368.

78. Chan, E. M.; Xu, C.; Mao, A. M.; Han, G.; Owen, J. S.; Cohen, B. E.; Milliron, D.J. *Nano Lett* **2010**, *10*, 1874.

79. Srivastava, B. B.; Jana, S.; Karan, N. S.; Paria, S.; Jana, N. R.; Sarma, D. D.; Pradhan, N. *Phys Chem Lett* **2010**, *ASAP*.

80. Wagner, J.; Tshikudo, T. R.; Kohler, J. M. *Chem Eng J* **2008**, *135*, 104.

81. Chan, E. M.; Alivasatos, P. A.; Mathies, R. A. *J Am Chem Soc* **2005**, *127*, 13854.

82. Chan, E. M.; Alivasatos, P. A.; Mathies, R. A. *Nano Lett* **2003**, *3*, 199.

83. Voth, G. A.; Saint, T. C.; Dobler, G.; Gollub, J. P. *Phys Fluids* **2003**, *15*, 2560.

84. Wei, G. -T.; Liu, F. -K.; Wang, C. R. C. *Anal Chem* **1999**, *71*, 2085.

85. Waters, C. A.; Mills, A. J.; Johnson, K. A.; Schiffrin, D.J. *Chem Commun* **2003**, 540.

86. Verweij, H.; Shi, J. *Langmuir* **2005**, *21*, 5570.

87. Bai, L.; Ma, X.; Liu, J.; Sun, X.; Zhao, D.; Evans, D. G. *J Am Chem Soc* **2010**, *132*, 2333.

88. Hanauer, M.; Pierrat, S.; Zins, I.; Lotz, A.; Sonnischen, C. *Nano Lett* **2007**, *7*, 2881.

89. Stavis, S. M.; Giest, J.; Gaitan, M. *Lab Chip* **2010**, *10* , 2618.

90. Templeton, A. C.; Wuelfing, W. P.; Murray, R. W. *Acc Chem Res* **2000**, *33*, 27.

91. Skoog, A. S.; Holler, F. J.; Nieman, T. A. *Principles of Instrumental Analysis*, *5th ed*., Saunders Publishing, USA, **1998**.

92. Haiss, W.; Thanh, N. T. K.; Aveyard, J.; Fernig, D. G. *Anal Chem* **2007**, *79*, 4215.

93. Templeton, A. C.; Wuelfing, W. P.; Murray, R. W. *Acc Chem Res* **2000**, *33*, 27.

Chapter II

1. Cushing, B. L.; Kolesnichenko, V. L.; O' Connor, C. *J. Chem. Rev.* **2004**, *104*, 3893.

2. Daniel, M. C.; Astruc, D. *Chem. Rev.* **2004**, *104*, 293.

3. Murray, C. B.; Kagan, C. R.; Bawendi, M. G. *Science* **1995**, *270*, 1335.

4. Dahl, J. A.; Maddux, B.; Hutchison, J. E. *Chem. Rev.* **2007**, *107*, 2228.

5. Huff, T. B.; Hansen, M. N.; Zhao, Y.; Cheng, X. J.; Wei, A. *Langmuir* **2007**, *23*, 1596.

6. Grainger, D. W.; Castner, D. G. *Adv. Mater.* **2008**, *20*, 867.

7. (a) Hostetler, M. J.; Wingate, J. E.; Zhong, C. J.; Harris, J. E.; Vachet, R.W.; Clark, M. R.; Londono, J. D.; Green, S. J.; Stokes, J. J.; Wignall, G. D.; Glish, G. L.; Porter, M. D.; Evans, N. D.; Murray, R. W. *Langmuir* **1998**, *14*, 17. (b) Hostetler, M. J.; Wingate, J. E.; Zhong, C.- J.; Harris, J. E.; Vachet, R. W.; Clark, M. R.; Londono, J. D.; Green, S. J.; Stokes, J. J.; Wignall, G. D.; Glish, G. L.; Porter, M. D.; Evans, N. D.; Murray, R. W. *Langmuir* **1998**, *14*, 17.

8. Woehrle, G. H.; Hutchison, J. E. *Inorg. Chem.* **2005**, *44*, 6149. (b) Warner, M. G.; Hutchison, J. E. *Synthesis, Functionalization, and Surface Treatment of Nanoparticles*, American Scientific, NY, **2003**.

9. (a) Eustis, S.; El-Sayed, M. A. *Chem. Soc. Rev.* **2006**, *35*, 209. (b) El-Sayed, M. A. *Acc Chem Res* **2001**, *34*, 257.

10. Brust, M.; Walker, M.; Bethell, D. Schiffrin, D. J.; Whyman, R. *Chem. Comm.* **1994**, 801.

11. Turkevich, J. *Gold Bull* **1985**, *18*, 86.

12. Templeton, A. C.; Wuelfing, M. P.; Murray, R. W. *Acc. Chem. Res.* **2000**, *33*, 27.

13. Caragheorgheopol, A.; Chechik, V. *Phys. Chem. Chem. Phys*. **2008**, *10*, 5029.

14. Stoeva, S.; Klabunde, K. J.; Sorensen, C. M.; Dragieva, I. *J. Am. Chem. Soc.* **2002**, *124*, 2305.

15. Prasad, B. L. V.; Stoeva, S. I.; Sorensen, C.M.; Klabunde, K. *J. Chem. Mater.* **2003**, *15*, 935.

16. (a) Ivanov, M. R.; Bednar, H. R.; Haes, A. J. *ACS. Nano.* **2009**, ASAP (b) Hill, H. D.; Millstone, J. E.; Banholzer, M. J.; Mirkin, C. A. *ACS Nano*, **2009**, ASAP

17. (a) Brewer, S. H.; Glomm, W. R.; Johnson, M. C.; Knag, M. K.; Franzen, S. *Langmuir* **2005**, *21*, 9303. (b) Ojea-Jimenez, I.; Puntes, V. *J. Am. Chem. Soc.* **2009**, *131*, 13320.(c) Zhu, T.; Vasilev, K.; Kreiter, M.; Mittler, S.; Knoll, W. *Langmuir* **2003**, *19*, 9518. (d) Newman, J. D. S.; Mac Crehan, W. A. *Langmuir* **2009**, *25*, 8993.

18. Shon, Y. -S.; Gross, S. M.; Dawson, B.; Porter, M.; Murray, R. W. *Langmuir* **2000**, *16*, 6555.

19. Shon, Y. S.; Gross, S. M.; Dawson, B.; Porter, M.; Murray, R. W. *Langmuir* **2001**, *17*, 1255.

20. Shon, Y. -S.; Cutler, E. *Langmuir* **2004**, *20*, 6626.

21. Ju-Nam, Y.; Bricklebank, N.; Allen, D. W.; Gardiner, P. H. E.; Light, M. E.; Hursthouse, M. B. *Org. Biomol. Chem.* **2006**, *4*, 4345.

22. (a) Lukkari, J.; Meretoja, M.; Karito, I.; Laajalehto, K.; Rajamaki, M.; Lindstrom, M.; Kankare, J. *Langmuir* **1999**, *15*, 3529. (b) Lusk, A. T.; Jennings, G. K. *Langmuir* **2001**, *17*, 1255, (c) Lee, M. -T.; Hseuh, C. -C.; Freund, M. S.; Ferguson, G. S. *Langmuir* **2003**, *19*, 5246.

23. Shelley, E. J.; Ryan, D.; Johnson, S. R.; Couillard, M.; Fitzmaurice, D.; Nellist, P. D.; Chen, Y.; Palmer, R. E.; Preece, J.A. *Langmuir* **2002**, *18*, 1791.

24. Sweeney, S. F.; Woehrle, G. H.; Hutchison, J. E. *J. Am. Chem. Soc.* **2006**, *128*, 3190-3197.

25. Kearns, G. J.; Foster, E. W.; Hutchison, J. E. *Anal. Chem.* **2007**, *79*, 9091.

26. Woehrle, G. M.; Hutchison, J. E.; Ozkar, S.; Finke, R. G. *Turk. J. Chem.* **2006**, *30*, 1.

27. Jorgensen, J. M.; Erlacher, K.; Pedersen, J. S.; Gothelf, K. V. *Langmuir* **2005**, *21*, 10320.

28. Ji, X.; Song, X.; Li, J.; Bai, Y.; Yang, W.; Peng, X. *J. Am. Chem. Soc.* **2007**, *129*, 13939.

29. (a) Kim, J.- H.; Chung, H. W.; Lee, T. R. *Chem Mater* **2006**, *18*, 4115-4120. (b) Hayat, M. A. *Colloidal gold: principles, methods, and applications*; Academic Press: San Diego, **1989.**

30. (a) Box, G. E. P.; Hunter, W. G.; Hunter, J. S. *Statistics for Experiments: An Introduction to design, data analysis, and model building*, Wiley, NY, **1978**. (b) Fernandez, J.; Kiwi, J.; Lizama, C.; Freer, J.; Baeza, J.; Masilla, H. D. *J. Photochem. Photobio. A* **2002**, *151*, 213. (c) Ruiz, V. S. C.; Dias, S. L. P.; Gushikea, Y.; Burns, R. E.; AIroldi, C. *J Solid State Chem* **2004**, *177*, 675.

31. Hiramatsu, H.; Osterloh, F. E. *Chem. Mater.* **2004**, *16*, 2509.

Chapter III

1. Daniel, M. C.; Astruc, D. *Chem Rev* **2004**, *104*, 293.

2. Dahl, J. A.; Maddux, B. L. S.; Hutchison, J. E. *Chem Rev* **2007**, *107*, 2228.

3. Caragheorgheopol, A.; Chechik, V. *Phys Chem Chem Phys* **2008**, *10*, 5029.

4. Shon, Y. S.; Gross, S. M.; Dawson, B.; Porter, M.; Murray, R. W. *Langmuir* **2000**, *16*, 6555.

5. Lohse, S. E.; Dahl, J. A.; Hutchison, J. E. *Langmuir* **2010**, *26*, 7504.

6. Shon, Y.- S.; Wuelfing, W. P.; Murray, R. W. *Langmuir* **2001**, *17*, 1255.

7. Shon, Y.- S.; Cutler, E. *Langmuir* **2004**, *20*, 6626.

8. Ju-Nam, Y.; Bricklebank, N.; Allen, D. W.; Gardiner, P. H. E.; Light, M. E.; Hursthouse, M. B. *Org Biomol Chem* **2006**, 4, 4345.

9. Zhang, S.; Leem, G.; Randall Lee, T. *Langmuir* **2009**, *25*, 13855.

10. Ionita, P.; Caragheorgheopol, A.; Gilbert, B. C.; Checik, V. *J Am Chem Soc* **2002**, *124*, 9048.

11. Ionita, P.; Caragheorgheopol, A.; Gilbert, B. C.; Checik, V. *Langmuir* **2004**, *20*, 11536.

12. Lisowski, C. E.; Hutchison, J. E. *Anal Chem* **2009**, *81*, 10246.

13. Choi, Y.; Ho, N. H.; Tung, C. H. *Angew Chem Int Ed* **2007**, *46*, 707.

14. Slocik, J. M.; Zabinski, J. S.; Phillips, D. M.; Naik, R. R. *Small* **2008**, *4*, 548.

15. Sun, L.; Liu, D.; Wang, Z. *Langmuir* **2008**, *24*, 10293.

16. Lee, J. S.; Han, M. S.; Mirkin, C. A. *Angew Chem Int Ed* **2007**, *46*, 4093.

17. Cha, J. N.; Bartl, M. H.; Wong, M. S.; Popitsch, A.; Deming, T. J.; Stucky, G. D. *Nano Lett* **2003**, *3*, 907.

18. Jeong, S.; Achermann, M.; Nanda, J.; Ivanov, S.; Klimov, V. I.; Hollingsworth, J. A. *J Am Chem Soc* **2005**, *127*, 10126.

19. Kim, T.; Noh, M.; Lee, H.; Joo, S.-W.; Lee, S. Y.; Lee, K. *J Phys Chem B* **2009**, *113*, 14487.

20. Niikura, K.; Nagakawa, K.; Ohtake, N.; Suzuki, T.; Matsuo, Y.; Sawa, H.; Ijiro, K. *Bioconj Chem* **2009**, *20*, 1848.

21. Paul, S.; Pearson, C.; Molloy, A.; Cousins, M. A.; Green, M.; Kolliopoulou, S.; Dimitrakis, P.; Normand, P.; Tsoukalas, D.; Petty, M. C. *Nano Lett* **2003**, *3*, 533.

22. Zheng, J.; Constantinou, P. E.; Micheel, C.; Alivisatos, A. P.; Kiehl, R. A.; Seeman, N. C. *Nano Lett* **2006**, *6*, 1502.

23. Yonezawa, T.; Yasui, K.; Kimizuka, N. *Langmuir* **2001**, *17*, 271.

24. Chen, C.-F.; Tzeng, S.-D.; Chen, H.-Y.; Lin, K.-J.; Gwo, S. *J Am Chem Soc* **2007**, *130*, 824.

25. Ishifuji, M.; Mitsuishi, M.; Miyashita, T. *J Am Chem Soc* **2009**, *131*, 4418.

26. Kang, Y.; Erickson, K. J.; Taton, T. A. *J Am Chem Soc* **2005**, *127*, 13800.

27. Hayat, M. A. *Colloidal Gold: Principles, Methods, and Applications*; Academic Press: San Diego, **1989**.

28. Rotello, V. M. *Nanoparticles: Building Blocks for Nanotechnology*; Kluwer Academic/Plenum Publishers: New York, **2004**.

29. Lukkari, J.; Meretoja, M.; Kartio, I.; Laajalehto, K.; Rajamaki, M.; Lindstrom, M.; Kankare, J. *Langmuir* **1999**, *15*, 3529.

30. Lusk, A. T.; Jennings, G. K. *Langmuir* **2001**, *17*, 7830.

31. Lee, M.-T.; Hseuh, C.-C.; Freund, M.S.; Ferguson, G.S. *Langmuir* **2003**, *19*, 5246.

32. Ciszek, J. W.; Stewart, M. P.; Tour, J. M. *J Am Chem Soc* **2004**, *126*, 13172.

33. Hostetler, M. J.; Wingate, J. E.; Zhong, C. J.; Harris, J. E.; Vachet, R. W.; Clark, M. R.; Londono, J. D.; Green, S. J.; Stokes, J. J.; Wignall, G. D.; Glish, G. L.; Porter, M. D.; Evans, N. D.; Murray, R. W. *Langmuir* **1998**, *14*, 17.

34. Templeton, A. C.; Wuelfing, W. P.; Murray, R. W. *Acc Chem Res* **2000**, *33*, 27.

35. Brewer, S.H.; Glomm, W.R.; Johnson, M.C.; Kang, M.K.; Franzen, S. *Langmuir* **2005**, *21*, 9303.

36. Rouhana, L. L.; Jaber, J. A.; Schlenoff, J. B. *Langmuir* **2007**, *23*, 12799.

37. Lin, S.- Y.; Tsai, Y.- T.; Chen, C.- C.; Lin, C.- M.; Chen, C.- H. *J Phys Chem B* **2004**, *108*, 2134.

38. Xie, H.; Tkachenko, A. G.; Glomm, W. R.; Ryan, J. A.; Brennaman, M. K.; Papankolni, J. M.; Franzen, S.; Feldheim, D. L. *Anal Chem* **2003**, *75*, 5797.

39. Isaacs, S. R.; Cutler, E. C.; Park, J.- S., Lee, T.; Shon, Y.- S. *Langmuir* **2005**, *21*, 5689.

40. Kearns, G.; Hutchison, J. E. *Anal Chem* **2006,** *78*, 298.

41. Woehrle, G. H.; Hutchison, J. E.; Ozkar, S.; Finke, R. G. *Turk J Chem* **2006**, *30*, 1.

42. Sweeney, S. F.; Woehrle, G. H.; Hutchison, J. E. *J Am Chem Soc* **2006**, *128*, 3190.

43. Eustis, S.; El-Sayed, M. A. *Chem Soc Rev* **2006**, *35*, 209.

44. Turner, M.; Golovko, V. B.; Vaughan, O. P. H.; Abdulkin, P.; Berenguer-Murcia, A.; Tikhov, M. S.; Johnson, B. F. G.; Lambert, R. M. *Nature* **2008**, *454*, 981.

45. Sanchez, A.; Abbet, S.: Hiez, U.; Schneider, W.- D.; Hakkineen, H.; Barnett, R. N.; Landman, V. *J Phys Chem A* **1999**, *103*, 9573.

46. Song, Y.; Challa, J. H.; Kumar, C. S. S. R. *Small* **2008**, *4*, 698.

Chapter IV

1. Jana, N.R.; Peng, X. *J Am Chem Soc* **2003**, *125*, 14280.

2. Dahl, J.A.; Maddux, B.L.S.; Hutchison, J.E. *Chem Rev* **2007**, *107*, 2228.

3. Jana, N. R. *Small* **2005**, *1*, 875.

4. Wang, Z.; Lu, M.; Wang, X.; Yin, R.; Song, Y.; Le, X.C.; Wang, H. *Anal Chem* **2009**, *81*, 10285.

5. Song, Y.; Challa, J.H.; Kumar, S.S.R. *Small* **2008**, *4*, 698.

6. Chen, Y.-Y.; Chang, H.-T.; Shiang, Y.-C.; Hung, Y.-L.; Chiang, C.-K.; Huang, C.-C. *Anal Chem* **2009**, *81*, 9433.

7. Sardar, R.; Funston, A.M.; Mulvaney, P.; Murray, R.W. *Langmuir* **2009**, *25*, 13840.

8. Lisowski, C.E.; Hutchison, J.E. *Anal Chem* **2009**, *81*, 10246.

9. Song, Y.; Doomes, E.E.; Prindle, J.; Tittsworth, R.; Hormes, J. *J Phys Chem B* **2005**, *109*, 9330.

10. Yang, S.-Y.; Chang, F.-Y.; Yeh, C.-S.; Lee, G.-B. *Microfluidics and Nanofluidics* **2010**, *8*, 303.

11. Duraiswamy, S.; Khan, S.A. *Small* **2009**, *5*, 2828.

12. Jackman, R.J.; Ghodssi, F.R.; Schmidt, M.A.; Jensen, K.F. *J Micromech Microengineering* **2001**, *11*, 263.

13. Valencia, P.M.; Basto, P.M.; Zhang, L.; Rhee, M.; Langer, R.; Farokhzad, O.C.; Karnik, R. *ACS Nano* **2010**, *4*, 1671.

14. Koesdjojo, M.T.; Koch, C.R.; Remcho, V.T. *Anal Chem* **2009**, *81*, 1652.

15. Hung, L.H.; Choi, K.M.; Tseng, W.Y.; Tan, Y.C.; Shea, J.; Lee, A.P. *Lab Chip* **2006**, *6*, 174.

16. Edel, J.B.; Fort, R.; De Mello, J.C. *Chem Commun* **2002,** *10***,** 1136.

17. Wagner, J.; Tshikudo, T.R.; Kohler, J.M. *Chem Eng J* **2008**, *135*, S104-S109.

18. Wagner, J.; Kirner, T.; Mayer, G.; Albert, J.; Kohler, J.M. *Chem Eng J* **2004**, *101*, 251.

19. Wagner, J.; Kohler, J.M. *Nano Lett* **2005**, 5, *685*.

20. Chan, E.M.; Mao, A.W.; Han, G.; Owen, J.S.; Cohen, B.E.; Milliron, B.J. *Nano Lett* **2010**, *10*, 1874.

21. Chan, E.M.; Mathies, R.A.; Alivasatos, A.P. *Nano Lett* **2003**, 3, 199.

22. Weng, C.H.; Huang, C.-C.; Yeh, C.-S.; Lei, H.Y.; Lee, G.-B. *J Micromech Microengineering* **2008**, *18*, 35019.

23. Koch, C.R.; Ingle, J.D.; Remcho, V.T. In *Proceedings of the Twelfth International Conference on Miniaturized Systems for Chemistry and Life Sciences* San Diego, CA, USA; **2008**,1900.

24. Pregibon, D. C. *Science* **2007**, *315*, 1393.

25. Doerr, A. *Nature Methods* **2007**, *4*, 381.

26. Lohse, S.E.; Dahl, J.A.; Hutchison, J.E. *Langmuir* **2010**, *26*, 126.

27. Kearns, G.J.; Foster, E.W.; Hutchison, J.E. *Anal Chem* **2006**, *78*, 298.

28. Woehrle, G.H.; Hutchison, J.E.; Ozkar, S.; Finke, R.G. *Turk J Chem* **2006**, 1.

29. Haiss, W.; Thanh, N.T.K.; Aveyard, J.; Fernig, D.E. *Anal Chem* **2007**, *79*, 4215.

30. Hostetler, M.J.; Wingate, J.E.; Zhong, C.J.; Harris, J.E.; Vachet, R.W.; Clark, M.R.; Londono, J.D.; Green, S.J.; Stokes, J.J.; Wignall, G.D. Glish, G.L.; Proter, M.D.; Evans, N.D.; Murray, R.W. *Langmuir* **1998**, *14*, 17.

31. Link, S.; El-Sayed, M.A. *J Phys Chem B* **1999**, *103*, 4212.

32. Templeton, A.C.; Weulfing, W.P.; Murray, R.W. *Acc Chem Res* **2000**, *33*, 27.

Chapter V

1. Song, Y.; Hormes, J.; Kumaar, C.S.S.R. *Small* **2008**, *4*, 698.

2. Whitesides, G.M. *Nature* **2006**, *442*, 368.

3. DeMello, A.J. *Nature* **2006**, *442*, 394.

4. Wagner, J.; Kirner, T.; Mayer, G.; Albert, G.; Kohler, G.M. *Chem Eng J* **2004**, *101*, 251.

5. Song, Y.; Doomes, E.E.; Prindle, J.; Tittsworth, R.; Hormes, J.; Kumar, C.S.S.R. *J Phys Chem B* **2005**, *109*, 9330.

6. Wagner, J.; Kirner, T.; Mayer, G.; Albert, J.; Kohler, J.M. *Chem Eng J* **2004**, *101*, 251.

7. Wagner, J.; Kohler, J.M. *Nano Lett* **2005**, *5*, 685.

8. Kohler, J.M.; Wagner, J.; Albert, J. *J Mater Chem* **2005**, *15*, 1924.

9. Yeng, S.Y.; Cheng, F.Y.; Chen, S.Y.; Lee, G.B. *Microfluidics and Nanofluidics* **2008,** *8*, 303.

10. Weng, C.H.; Huang, C.C.; Leh, H.Y.; Lee, G.B. *J Micromechanics and Microengineering* **2008**, *18*, 30519.

11. Chang, C.H.; Paul, B.K.; Remcho, V.T.; Atre, S.; Hutchsion, J.E. *J Nanoparticle Research* **2008**, *10*, 956.

12. Polte, J. *J Phys Conference Series* **2010**, *247*, 1.

13. Polte, J.; Ahner, T.T.; Delissen, F.; Sokolov, S.; Emmerling, F.; Thumnemann, A.F.; Kraehnert, R. *J Am Chem Soc* **2010**, *132*, 1296.

14. Njoki, P.N.; Luo, J.; Kamundi, M.M.; Lim, S.; Zhong, C.-J. *Langmuir* **2010** *26*, 13622.

15. Shields, S.P.; Richards, V.N.; Buhro, W.E. *Chem Mater* **2010**, *22*, 3212.

16. Kumar, S.; Gandhi, K.S.; Kumar, R. *Ind Eng Chem Res* **2007**, *46*, 3128.

17. Toyota, A.; Nakamura, H.; Ozono, H.; Yamashita, K.; Uehara, M.; Maeda, H. *J Phys Chem C* **2010**, *114*, 7527.

18. Liu, X.; Dai, Q.; Austin, L.; Coults, J.; Knowles, G.; Zou, J.; Chen, H.; Huo, Q. *J Am Chem Soc* **2008**, *130*, 2780.

19. Jans, H.; Liu, X.; Austin, L.; Maes, G.; Huo, Q. *Anal Chem* **2009**, *81*, 9425.

20. Kalluri, J.R.; Chandra, P. *Angew Chem Int* **2009**, *121*, 9848.

21. Wiles, C.; Watts, P. *Eur J Org Chem* **2008**, *10*, 1655.

22. Edel, J.B.; Fortt, R.; deMello, J.C.; deMello, A.J. *Chem. Commun.* **2002**, 1136.

23. K. D. Wise, *Proc. IEEE* **1998**, *86*, 1531.

24. Chan, E.M.; Mathies, R.A.; Alivisatos, A.P. *Nano Lett.* **2003**, *3*, 199.

25. Shestopalov, I.; Tice, J.D.; Ismagilov, R.F. *Lab Chip* **2004**, *4*, 316.

26. Daniel, M.; Astruc, D. *Chem Rev* **2004**, *104*, 293.

27. Templeton, A. C.; Wuelfing, W. P.; Murray, R. W. *Acc Chem Res* **2000**, *33*, 27.

28. Lohse, S.E.; Lisowski, C.E.; Hutchison, J.E. *Inorg Chem* **2011** Submitted.

29. Dahl, J.A.; Maddux, B.L.S.; Hutchison, J.E. *Chem Rev* **2007**, *107*, 2228.

30. Lohse, S.E.; Dahl, J.A.; Hutchison, J.E. *Langmuir* **2010**, *28*, 126.

31. Sweeney, S. F.; Woehrle, G. H.; Hutchison, J. E. *J Am Chem Soc* **2006**, *128*, 3190.

32. McKenzie, L.C.; Haben, P.M.; Kevan, S.D.; Hutchison, J.E. *J Phys Chem C* **2010**, *114*, 22055.

33. Haiss, W.; Thanh, N.T.K.; Aveyard, J.; Fernig, D.G. *Anal Chem* **2007**, *79*, 4215.

34. Khlebtsov, N.G. *Anal Chem* **2008**, *80*, 6620.

35. Shull, C.G.; Roess, L.C. *J App Phys* **1947**, *18*, 295.

36. Roess, L.C.; Shull, C.G. *J App Phys* **1947**, *18*, 308.

37. Kotlarckyk, M.; Stephens, R.B.; Huang, J.S. *J Phys Chem* **1988**, *92*, 1533.

38. Kotlarchyk, M.; Chen, S.-H. *J Chem Phys* **1983**, *79*, 2461.

39. Shi, X.; Luo, J.; Njoki, P.N. *Ind Eng Chem Res* **2008**, *4*, 4675.

40. Souza, G.R.; Stanquicini, F.I.; Arap, W. *Biomedical Microdevices* **2010**, *12*, 597.

41. Wang, G.; Park, H.Y.; Lipert, R.J.; Parker, M.D. *Anal Chem* **2009**, *81*, 9643.

Chapter VI

1. Polte, J.; Ahner, T.T.; Delissen, F.; Sokolov, S.; Emmerling, F.; Thumnemann, A.F.; Kraehnert, R. *J Am Chem Soc* **2010**, *132*, 1296.

2. Jana, N.R. *Small* **2005**, *1*, 875.

3. Millstone, J.E.; Wei, W.; Jones, M.R.; Yoo, H.; Mirkin, C.A. *Nano Lett* **2008**, *8*, 2526.

4. Njoki, P.N.; Luo, J.; Kamundi, M.M.; Lim, S.; Zhong, C.-J. *Langmuir* **2010**, *26*, 13622.

5. Shields, S.P.; Richards, V.N.; Buhro, W.E. *Chem Mater* **2010**, *22*, 3212.

6. Kumar, S.; Gandhi, K.S.; Kumar, R. *Ind Eng Chem Res* **2007**, *46*, 3128.

7. Gulati, A.; Liao, H.; Hafner, J.H. *J Phys Chem B* **2006** *110*, 22323.

8. Henkel, A.; Schubert, O.; Plech, A.; Sonnischen, C. *J Phys Chem C* **2009**, *113*, 10390.

9. Kimling, J.; Maier, M.; Okenve, B.; Kotaidis, V.; Ballot, H.; Plech, A. *J Phys Chem B* **2006**, *110*, 15700.

10. Qu, L.; Yu, W.W.; Peng, X. *Nano Lett* **2004**, *4*, 465.

11. Murphy, C.J. *J Mater Chem* **2008**, *18*, 2173.

12. Smith, D.K.; Korgel, B.A. *Langmuir* **2008**, *24*, 644.

13. Smith, D.K.; Miller, N.R.; Korgel, B.A. *Langmuir* **2009**, *25*, 9518.

14. Dahl, J. A.; Maddux, B. L. S.; Hutchison, J. E. *Chem Rev* **2007**, *107*, 2228.

15. LaMer, V. K.; Dinegar, R. H. *J Am Chem Soc* **1950**, *72*, 4847.

16. Levit, A. B.; Rowell, R. L. *J Colloid Interface Sci*. **1975**, 50, 162.

17. Frens, G. *Nat Phys-Sci* **1973**, *241*, 20.

18. Sugimoto, T. *Adv Colloid Interface Sci* **1988**, 2865.

19. Talapin, D.V.; Rogach, J.L.; Hasse, M.; Welles, H. *J Phys Chem B* **2001**, *105*, 12278.

20. Ji, X.; Song, X.; Li, J.; Bai, Y.; Yang, W.; Peng, X. *J Am Chem Soc* **2007**, *129*, 13939.

21. Daniel, M.; Astruc, D. *Chem Rev* **2004**, *104*, 293.

22. Joyce, P.B.; Krzyzewski, T.J.; Bell, G.R.; Jones, T.S.; Malik, S.; Childs, D.; Murray, R.W. *Phys Rev B* **2000**, *62*, 10891.

23. Murray, C.B. *Science* **2009**, *324*, 1276.

24. Zheng, H.M.; Smith, R.K.; Jun, Y.W.; Kisolowski, C.; Dhamen, U.; Alivasatos, A.P. *Science* **2009**, *324*, 1309.

25. Polte, J. *J Phys Conference Series* **2010**, *247*, 1.

26. McKenzie, L. C.; Haben, P. M.; Kevan, S. D.; Hutchison, J. E. *J Phys Chem C* **2010**, ASAP.

27. Pong, B.-K.; Elim, H.I.; Chong, J.-X.; Ji, W.; Trout, B.L.; Lee, J.-Y. *J Phys Chem C* **2007**, *111*, 6281.

28. Pan, D.; Ji, X.; An, L.; Lu, Y. *Chem Mater* **2008**, *20*, 3560.

29. Richman, E.K.; Hutchison, J.E. *ACS Nano*, **2009**, *3*, 2441.

30. Grainger, D.W.; Castner, D.G. *Adv Mater* **2008**, *20*, 867.

31. Hutchison, J.E. *ACS Nano* **2008**, *2*, 395.

32. Baer, D.R.; Gaspar, D.J.; Nachimuthu, P.; Techane, S.D.; Castner, D.G. *Anal Bioanal Chem* **2010**, *396*, 983.

33. Abécassis, B.; Testard, F.; Spalla, O.; Barboux, P. *Nano Lett* **2007**, *7*, 1723.

34. Becker, J.; Schubert, O.; Sonnichsen, C. *Nano Lett* **2007**, *7*, 1664.

35. Saunders, A.E.; Sigman, M.B.; Korgel, B.A. *J Phys Chem B* **2004**, *108*, 193.

36. Song, Y.; Hormes, J.; Kumaar, C.S.S.R. *Small* **2008**, *4*, 698.

37. Wagner, J.; Kirner, T.; Mayer, G.; Albert, G.; Kohler, G.M. *Chem Eng J* **2004**, *101*, 251.

38. Lohse, S.E.; Dahl, J.A.; Hutchison, J.E. *Langmuir* **2010**, *26*, 7504.

39. Haiss, W.; Thanh, N.T.K.; Aveyard, J.; Fernig, D.G. *Anal Chem* **2007**, *79*, 4215.

40. Khlebtsov, N.G. *Anal Chem* **2008**, *80*, 6620.

41. Shull, C.G.; Roess, L.C. *J App Phys* **1947**, *18*, 295.

42. Roess, L.C.; Shull, C.G. *J App Phys* **1947**, *18*, 308.

43. Kotlarckyk, M.; Stephens, R.B.; Huang, J.S. *J Phys Chem* **1988**, *92*, 1533.

44. Kotlarchyk, M.; Chen, S.-H. *J Chem Phys* **1983**, *79*, 2461.